AD-753 529

FRACTURE AND COMMINUTION OF ROCK

John E. Reaugh, et al

Physics International Company

Prepared for:

Advanced Research Projects Agency
Bureau of Mines

November 1972

Contractor: Physics International Company
Effective Date of Contract: 15 January 1971
Contract Expiration Date: 15 February 1972
Amount of Contract: $97,825
Contract Number: H0210014
Principal Investigator: J. Reaugh (415-357-4610)
Project Scientist: D. Maxwell (415-357-4610)

FRACTURE AND COMMINUTION OF ROCK

PIFR-310

November 1972

J. E. Reaugh, I. O. Huebsch, and R. P. Swift

Sponsored by

Advanced Research Projects Agency
ARPA Order No. 1579, Amend. 2
Program Code 1F10

PHYSICS INTERNATIONAL COMPANY
2700 MERCED STREET • SAN LEANDRO, CALIFORNIA 94577 • PHONE 357-4610 (415) • TWX 891-9689 (415)

Security Classification

DOCUMENT CONTROL DATA - R&D

(Security classification of title, body of abstract and indexing annotation must be entered when the overall report is classified)

1 ORIGINATING ACTIVITY (Corporate author) Physics International Company 2700 Merced Street San Leandro, California 94577	2a. REPORT SECURITY CLASSIFICATION Unclassified 2b GROUP

3. REPORT TITLE

Fracture and Comminution of Rock

4. DESCRIPTIVE NOTES (Type of report and inclusive dates)

Final Report, 15 January 1971 through 15 February 1972

5 AUTHOR(S) (Last name, first name, initial)

Reaugh, John E.; Huebsch, Ian O.; Swift, Robert P.

6. REPORT DATE	7a. TOTAL NO. OF PAGES	7b. NO. OF REFS
November 1972	123	29

8a. CONTRACT OR GRANT NO. HO210014 b. PROJECT NO. ARPA Order No. 1579, Amend. 2 c. Program Code 1F10 d.	9a. ORIGINATOR'S REPORT NUMBER(S) PIFR-310 9b. OTHER REPORT NO(S) (Any other numbers that may be assigned this report)

10 AVAILABILITY/LIMITATION NOTICES

11 SUPPLEMENTARY NOTES Details of illustrations in this document may be better studied on microfiche	12. SPONSORING MILITARY ACTIVITY Advanced Research Projects Agency

13. ABSTRACT

Existing theories of fracture and comminution of rock were examined and applied to an idealized blasting configuration to obtain the resulting particle size distribution. The results were reasonable, but more development is required for practical applications. An exploding wire apparatus was developed to generate tensile fracture data in thick-walled cylinders of Westerly granite. The experimental results were interpreted with the aid of a finite-difference continuum mechanics computer program. It is indicated that fracture initiation in Westerly granite requires more than 600 bar hoop tension, but that crack propagation is possible with less.

DD FORM 1 JAN 64 1473

Security Classification

14. KEY WORDS	LINK A		LINK B		LINK C	
	ROLE	WT	ROLE	WT	ROLE	WT
Comminucion theory						
Dynamic tensile strength						
Exploding wires						
Westerly granite						
Rock fracture						

INSTRUCTIONS

1. ORIGINATING ACTIVITY: Enter the name and address of the contractor, subcontractor, grantee, Department of Defense activity or other organization *(corporate author)* issuing the report.

2*a*. REPORT SECURITY CLASSIFICATION: Enter the overall security classification of the report. Indicate whether "Restricted Data" is included. Marking is to be in accordance with appropriate security regulations.

2*b*. GROUP: Automatic downgrading is specified in DoD Directive 5200.10 and Armed Forces Industrial Manual. Enter the group number. Also, when applicable, show that optional markings have been used for Group 3 and Group 4 as authorized.

3. REPORT TITLE: Enter the complete report title in all capital letters. Titles in all cases should be unclassified. If a meaningful title cannot be selected without classification, show title classification in all capitals in parenthesis immediately following the title.

4. DESCRIPTIVE NOTES: If appropriate, enter the type of report, e.g., interim, progress, summary, annual, or final. Give the inclusive dates when a specific reporting period is covered.

5. AUTHOR(S): Enter the name(s) of author(s) as shown on or in the report. Enter last name, first name, middle initial. If military, show rank and branch of service. The name of the principal author is an absolute minimum requirement.

6. REPORT DATE: Enter the date of the report as day, month, year, or month, year. If more than one date appears on the report, use date of publication.

7*a*. TOTAL NUMBER OF PAGES: The total page count should follow normal pagination procedures, i.e., enter the number of pages containing information.

7*b*. NUMBER OF REFERENCES: Enter the total number of references cited in the report.

8*a* CONTRACT OR GRANT NUMBER: If appropriate, enter the applicable number of the contract or grant under which the report was written.

8*b*, &*c*, & 8*d*. PROJECT NUMBER: Enter the appropriate military department identification, such as project number, subproject number, system numbers, task number, etc.

9*a*. ORIGINATOR'S REPORT NUMBER(S): Enter the official report number by which the document will be identified and controlled by the originating activity. This number must be unique to this report.

9*b* OTHER REPORT NUMBER(S): If the report has been assigned any other report numbers *(either by the originator or by the sponsor)*, also enter this number(s).

10. AVAILABILITY/LIMITATION NOTICES: Enter any limitations on further dissemination of the report, other than those imposed by security classification, using standard statements such as:

(1) "Qualified requesters may obtain copies of this report from DDC."

(2) "Foreign announcement and dissemination of this report by DDC is not authorized."

(3) "U. S. Government agencies may obtain copies of this report directly from DDC. Other qualified DDC users shall request through _____."

(4) "U. S. military agencies may obtain copies of this report directly from DDC. Other qualified users shall request through _____."

(5) "All distribution of this report is controlled. Qualified DDC users shall request through _____."

If the report has been furnished to the Office of Technical Services, Department of Commerce, for sale to the public, indicate this fact and enter the price, if known.

11. SUPPLEMENTARY NOTES: Use for additional explanatory notes.

12. SPONSORING MILITARY ACTIVITY: Enter the name of the departmental project office or laboratory sponsoring *(paying for)* the research and development. Include address.

13. ABSTRACT: Enter an abstract giving a brief and factual summary of the document indicative of the report, even though it may also appear elsewhere in the body of the technical report. If additional space is required, a continuation sheet shall be attached.

It is highly desirable that the abstract of classified reports be unclassified. Each paragraph of the abstract shall end with an indication of the military security classification of the information in the paragraph, represented as *(TS)*, *(S)*, *(C)* or *(U)*.

There is no limitation on the length of the abstract. However, the suggested length is from 150 to 225 words.

14 KEY WORDS: Key words are technically meaningful terms or short phrases that characterize a report and may be used as index entries for cataloging the report. Key words must be selected so that no security classification is required. Identifiers, such as equipment model designation, trade name, military project code name, geographic location, may be used as key words but will be followed by an indication of technical context. The assignment of links, roles, and weights is optional.

Contractor: Physics International Company
Effective Date of Contract: 15 January 1971
Contract Expiration Date: 15 February 1972
Amount of Contract: $97,825
Contract Number: H0210014
Principal Investigator: J. Reaugh (415-357-4610)
Project Scientist: D. Maxwell (415-357-4610)

FRACTURE AND COMMINUTION OF ROCK

PIFR-310

November 1972

J. E. Reaugh, I. O. Huebsch, and R. P. Swift

Sponsored by

Advanced Research Projects Agency
ARPA Order No. 1579, Amend. 2
Program Code 1F10

Preparing Agency

Physics International Company
2700 Merced Street
San Leandro, California 94577

IC

ABSTRACT

Existing theories of fracture and comminution of rock were examined and applied to an idealized blasting configuration to obtain the resulting particle size distribution. The results were reasonable, but more development is required for practical applications. An exploding wire apparatus was developed to generate tensile fracture data in thick-walled cylinders of Westerly granite. The experimental results were interpreted with the aid of a finite-difference continuum mechanics computer program. It is indicated that fracture initiation in Westerly granite requires more than 600 bar hoop tension, but that crack propagation is possible with less.

CONTENTS

CONTENTS (cont.)

ILLUSTRATIONS

ILLUSTRATIONS (cont.)

ILLUSTRATIONS (cont.)

SECTION 1
BACKGROUND AND INTRODUCTION

A recent study by a committee of the National Academy of Sciences points out the need for advances in the technology of underground excavation (Reference 1). The need is most acute for hard rock tunneling and mining which are now done almost exclusively by drill-and-blast methods. Although these methods have improved steadily for many years, their inherently cyclic nature imposes fundamental limitations on the excavation rates attainable and on the means of reducing costs. To increase speed and reduce costs significantly, it will be necessary to develop equipment that operates continuously.

Both established and advanced excavation techniques consist of breaking rock and moving the pieces. Ideally, the system for rock breakage at the face should have minimal energy requirements. Effective muck handling systems, however, require that the size of the broken rock be controlled. Optimization of these two elements requires improved capabilities for predicting rock fracture. For example, two promising systems for muck handling--slurry pumping and pneumatic transport--require that the maximum fragment size be controlled. Even for more conventional methods of muck removal, the production of relatively small fragments in the primary rock breaking process may be attractive since, although more expensive, it may allow continuous removal by conveyor rather than by batch, loader, and truck methods. For

mining operations, a smaller fragment size may reduce the number of crushing stages required in the mineral concentration and refining processes. All of these examples indicate the desirability of small fragment sizes. However, excessive production of fines (the dust produced in the fragmentation process) can be detrimental to health and safety. This dust, even if only constituting a small mass fraction of the total debris formed, can create an explosion hazard, and its inhalation is potentially injurious to health. Thus, finding ways to increase the overall efficiency of rock fracture and comminution requires ways to predict not only the average particle size but also the size distribution.

The data base associated with the problem of rock fracture and comminution largely derives from three sources: practical field experience in excavation, impact and single-explosive-charge cratering experience, and steady-state crushing and grinding operations. Through practical field experience, specific recommendations for blast-hole drilling patterns, charge loads, and firing sequences for particular geologies have emerged. Correlations of crater size with explosive (or kinetic) energy have been made over many decades of yield, ranging from smaller than gram-sized charges in laboratory tests to impact craters caused by meteors which had kinetic energies equivalent to many megatons of TNT (Reference 2). Additional correlations from cratering events have been made which relate the size of the largest fragment produced to the source energy. Data from grinding and crushing operations have been used in correlations which relate output particle size distributions to the work done on the input size distribution.

To distill and understand this large body of seemingly unrelated data requires a theory of the processes involved in rock fracture and comminution. There exist computer codes (References 3 and 4) which can, in principle, calculate physical processes active in all three sources of fracture and comminution data. Such computer codes, developed primarily for the study of weapons effects, are capable of computing the response of materials to explosive detonations, projectile impact, and even static stress fields for a wide variety of geometries and material properties. These calculations are exact within the limitations of the numerical approximations of finite zone sizes and within uncertainties in the description of material behavior. To apply these calculations to a field experiment, using them to predict the production of small fragments directly, would require fine zoning, in fact zones smaller in size than the smallest expected fragment. Such direct computation of all particle sizes is not feasible in any currently conceived computer system. Moreover, such a deterministic method is unrealistic in light of the inherent variability of rock, the statistical distribution of particle sizes produced at any location, and the variation in stress histories produced in engineering operations under actual field conditions as opposed to laboratory conditions. On the other hand, many existing theories of comminution have been used to correlate data, but at times the simplifications that make them useful results in their providing little insight into the physical processes that occur.

A blend of these two approaches--calculating in detail simplified loading conditions and materials in an effort to understand these processes and testing the utility of simplified theories in more complex situations--was the approach used in the program reported here. As originally conceived, the program was

to have extended three years. This report covers only the first year's work. As a consequence, although specific information and results have been obtained, a coherent body of information is still lacking. The following summary section will place the specific results obtained in this study into perspective. This summary is followed by three sections presenting the specific results and a final section of conclusions and recommendations.

SECTION 2
PROGRAM SUMMARY AND RESULTS

The program consisted principally of two related activities: the examination of existing theories of fracture and comminution and the experimental and computational study of tensile fracture of Westerly granite. These activities are summarized below.

Existing theories of fracture and comminution range in their designed application from frictional wear to rock bursts. It would be very desirable for such existing theories, which typically correlate the data for which they were designed, to be also applicable to blasting. These theories generally require only a few material descriptive parameters, and, as a consequence, would adapt to the variability of properties present in any practical application. A computer program was devised and written to test promising theories with realistic blasting stress histories without having to make detailed calculations. In particular, the computer program was designed to be used in an iterative way so that various theories and experimental data could be checked. The preliminary results obtained seem to indicate that, under dynamic loading, reasonable particle size distributions can be predicted by considering the conversion of stored energy to surface energy. The model does, however, require further development before practical application is possible.

The second activity addressed the process of the tensile fracture of Westerly granite. Large amounts of data exist for Westerly granite, and detailed models of its nonlinear behavior under compressive loads have been formulated and are described here. The fracture and comminution computer program, other calculations, and blasting and cratering experiments, however, indicate that the largest mass of rock is broken in tension. In field blasting the effect of nearby surfaces is quite pronounced. The use of line drilling and pre-shearing techniques (Reference 5) to obtain smooth excavation lines are two clear examples. The reflection of compressive waves from these surfaces results in fracture in tensile stress. However, laboratory data on the dynamic tensile fracture of rock are very limited. In this study experimental techniques using an exploding wire to generate a low radial compressive stress and large hoop tension in granite blocks were established, and fracture data were obtained. A model of hoop tension failure was developed that accounts for the effect of cracks opening in the radial direction. When this model was applied to the experiments and the calculations using this model were analyzed, the following results were indicated: to initiate a fracture in Westerly granite requires more than 0.6-kbar hoop tension, but to propagate the fracture requires a tensile stress field of only about 0.3 kbar.

The fracture and comminution models and the computer program are discussed in the next section. In Section 4 details of an existing compressive failure model and a tensile failure model for Westerly granite are discussed. Section 5 reports the experimental method and results of dynamic tensile fracture of Westerly granite, and their interpretation. The final section summarizes the program and presents recommendations for further study.

SECTION 3
COMMINUTION MODEL DEVELOPMENT

3.1 TECHNICAL APPROACH

Effort on model development has included examination of different comminution theories and algorithms and selection of the most promising ones for intensive analysis. In modeling the time-dependent, sequential development of fracture and comminution, the excavation geometry and the interaction of compressive, shear, and tensile stresses all play a part. In examining idealized comminution models, simplified stress configurations and geometries were deliberately selected as an initial approach to a complex problem.

Simplified versions of certain of the algorithms were programmed and one-dimensional computations were performed. Relevant material properties were determined and numerical values selected for test computations. An analytical form of stress profile was used to represent the incident shock. The coefficients in this profile were varied in successive computations as part of the parametric study. Results of the initial computations were used to guide revision of the model. Figure 1 is a schematic flow diagram of the development procedure that was followed. The bottom line of the flow diagram shows a procedure recommended for future, continued development of the model.

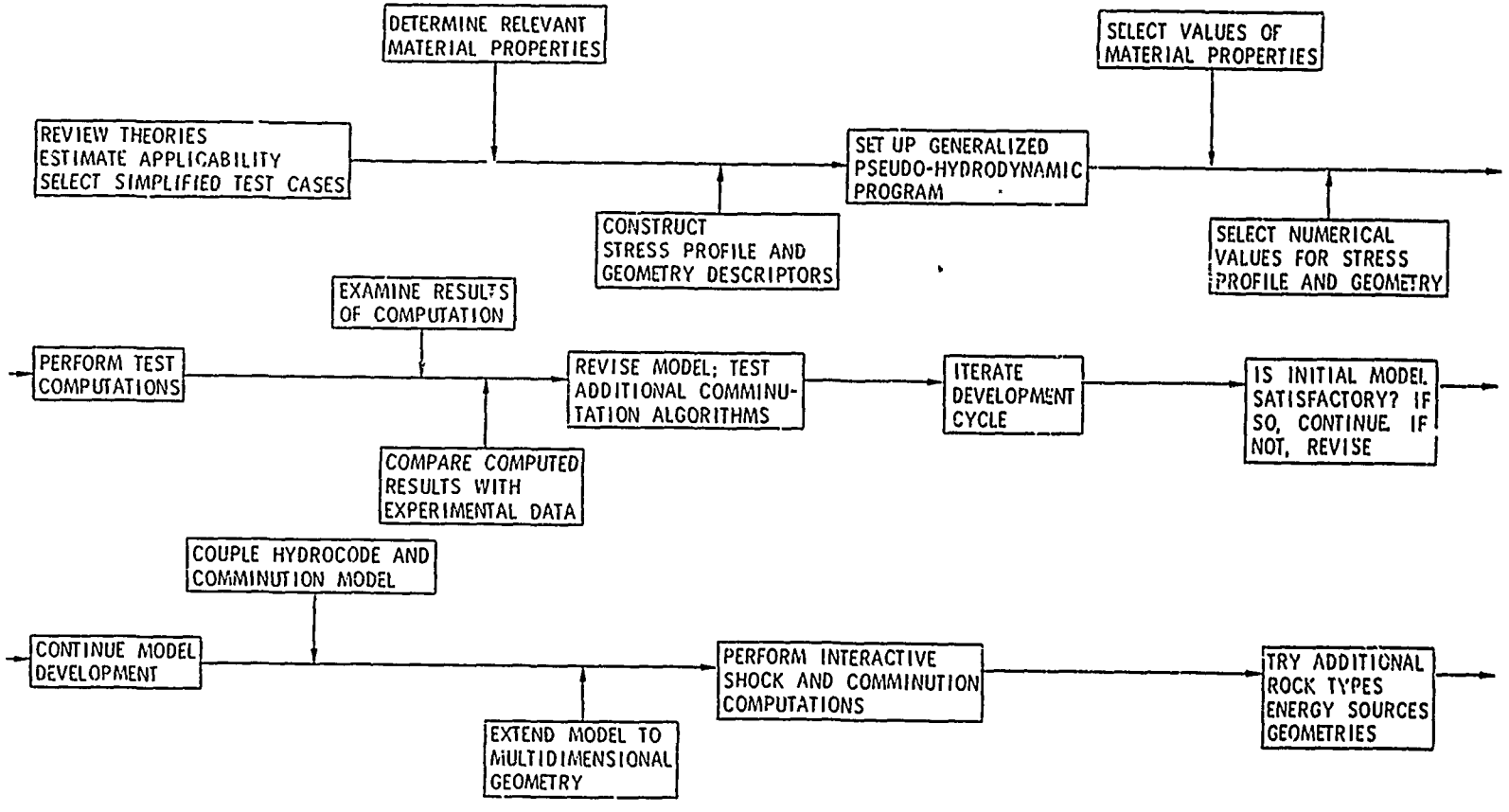

Figure 1 Fracture and comminution of rock: general procedure for development of analytical model.

In the remainder of this section the literature on comminution laws is reviewed and the computer program used to examine the various laws in idealized but dynamic conditions and geometries is discussed.

3.2 REVIEW OF COMMINUTION LAWS

Various models of fracture and comminution have been proposed. Comminution in steady-state grinding has been considered a chemical reaction whereby various kinds of atomic and molecular bonds are broken and reformed (Reference 6). The shock may be pictured as a grinding mill with the feed consisting of the undisturbed rock. The grinding process, then, consists of an energy-input, compression stage, followed by an energy-transformation, stress-relief and fragmentation stage. In this second stage, in certain geometries, a tensile wave arrives from a free surface and spallation occurs. The energy released and transformed may include not only the input energy, but, for deep excavation, stored strain energy due to the overburden (rock bursts are an example of release of such energy). Several of the comminution models considered apply to spallation; these include the wave theory of Hino (Reference 7), and the destruction-wave model of Galin (Reference 8).

Virtually all of the analytical comminution models studied are based on the key physical concept of energy balance, the energy absorbed being used to form particles with new surface area and with kinetic and possibly thermal energy. These comminution models can be classified as follows, in order of increasing complexity:

(a) Models dependent on material properties only. For instance, according to the adhesive-wear model of Rabiniwicz (Reference 9), average particle diameter is directly proportional to specific surface energy and inversely proportional to penetration hardness of the material.

(b) Models dependent also on a single stress-wave parameter. Peak stress and energy deposited are two such parameters. The grinding laws of Rittinger, Kick, and Bond present three different relations between energy expended and particle size produced (References 10 and 11).

(c) Models dependent in addition on a second stress-wave parameter such as stress rate, or pulse shape. The destruction-wave model of Galin and Cherepanov, for example, involves surface energy, peak stress, and wave speed (Reference 8).

Some of the models considered are briefly described below and examples of the corresponding algorithms are given. Figure 2 lists several of these models and their characteristics.

3.2.1 Adhesive-Wear Model of Rabinowicz (Reference 9). This model describes the conditions under which an asperity (protruding element) on a surface, subjected to a sliding stress, separates to become a particle. The separation or particle-formation condition is that the elastic energy stored in the element exceed the adhesional energy acting over the interface between the element and the main body of the surface. The diameter d of the (hemispherical) particle size is then given by

$$d = \frac{6E\ W_{ab}}{\nu^2\ \sigma_y^2}$$

1. SURFACE ENERGY (RITTINGER)

   NEW SURFACE AREA PROPORTIONAL TO AMOUNT OF ENERGY ABSORBED

2. VOLUME THEORY (KICK)

   EQUAL AMOUNTS OF ENERGY REQUIRED TO REDUCE INPUT PARTICLE SIZE BY EQUAL RATIOS

3. THIRD THEORY (BOND)

   USEFUL ENERGY INVERSELY PROPORTIONAL TO SQUARE ROOT OF PARTICLE DIAMETER

4. SPALL FRACTURE - WAVE THEORY

   SPALL THICKNESS PROPORTIONAL TO WAVELENGTH AND TENSILE STRENGTH AND INVERSELY TO PEAK PRESSURE

5. ROCK-BURST THEORY (GALIN)

   AVAILABLE ENERGY DEPENDS ON PRE-STRESS AND ELASTIC CONSTANTS PARTICLE SIZE PROPORTIONAL TO SURFACE ENERGY, INVERSE TO AVAILABLE ENERGY

6. CRACKING THEORY

   RADIAL CRACKS RELIEVE HOOP STRESSES
   CRACK SPACING DEPENDENT ON SOUND SPEED

Figure 2 Comminution theories.

where E is Young's modulus, W_{ab} the work of adhesion of the contacting materials, ν is Poisson's ratio, and σ_y is the yield stress. Using typical values for material properties, the average value 0.003 is taken for σ_y/E, ν^2 is assigned the value 0.1, and σ_y is assumed to equal one-third of the penetration hardness p; these values are representative of many materials. The result is

$$d = 60{,}000\ W_{ab}/p$$

where 60,000 is a dimensionless number. For identical contacting materials, W_{ab} is twice the surface energy. If we take representative values for silica, of 500 ergs/cm^2 surface energy and 800 kgf/mm^2 (8×10^{10} dyne/cm^2) hardness, this leads to particle diameter of the order of 10 microns. This size is obviously too small to represent average debris from a blasting operation. If, however, dynamic comminution is pictured as consisting of a primary spall process accompanied and followed by a high-speed friction between the ejected spall fragments, then the Rabinowicz model may account for the tail of the size distribution produced by this secondary process.

3.2.2 Rittinger's Law (Reference 11). The energy expended per unit volume to produce fragments, E, is proportional to the new surface area produced, or

$$E = k\left(S_2 - S_1\right)$$

where k is a dimensioned constant and S_2 and S_1 are the final and initial surface areas per unit volume. The factor k includes the effect of material properties and of the less than 100 percent efficiency in conversion of elastic energy to surface energy. In fact, a 1 percent efficiency factor is representative of comminution by grinding.

3.2.3 Kick's Law (Reference 11): Expenditures of equal amounts of energy result in equal geometrical changes in particle size, so that

$$E = k \ln \left(d_1/d_2\right)$$

where d_1 and d_2 are input (feed) and output (product) particle sizes and k is another constant. The Kick theory does not specify the value of the reduction ratio, d_1/d_2. Furthermore, in comminution of in situ rock the initial reduction ratio is infinite unless a value of natural fracture spacing is taken as the feed size. Thus, the Kick theory is not directly convertible into a fracture/comminution algorithm.

3.2.4 Bond's Law (Reference 11): Of the total energy expended, the portion useful in breakage is inversely proportional to the square root of particle diameter. Bond's law is usually defined in terms of the work index, W_i, the work required to crush material from infinite size to a 100-micron reference size. In these terms, total work per unit mass, W, required to crush material from feed size F to product size P is given by

$$W = W_i \left(\sqrt{\frac{100}{P}} - \sqrt{\frac{100}{F}}\right)$$

for both sizes measured in microns.

3.2.5 Wave Theory of Spall Fracture (Reference 7): For a plane shock wave of length L arriving with peak pressure p at a plane parallel free surface in a rock of tensile strength S_t, the thickness ℓ of each spalled slab is predicted to be

$$\ell = \frac{L}{2}\frac{S_t}{p}$$

and the number of slabs spalled, N, is given by

$$N = L/2\ell = p/S_t$$

Because the value of p cannot exceed the compressive strength S_c, it follows that

$$N \leq S_c/S_t = B$$

The blastability coefficient B ranges from 13 to 16 for marble, granite, and sandstone.

3.2.6 Destruction Wave Theory (Reference 8): According to this model, stored elastic energy is converted to surface energy and to kinetic energy of the fragments as the destruction wave propagates inward from a free surface. The energy partition is determined by the conservation equations. No allowance is made for thermal energy (in the form of waste heat, for example) in the partition. The model appears to have been developed to describe rock bursts.

3.2.7 Cracking Model: In the tensile cracking model for diverging geometries it is assumed that all failure is by hoop tension. This model is discussed in detail in another section of this report.

Of the foregoing size prediction theories, laws, or models, those of Rittinger, Bond, and Galin were selected for programming and computation. As the project developed (see Section 3.4) most attention was devoted to use of the Rittinger algorithm and analysis of the corresponding results.

3.3 DEVELOPMENT OF THE COMPUTATIONAL MODEL

The discussion is arranged in accordance with the schematic diagram of the comminution model shown in Figure 3. The figure represents both a task breakdown used in model development and a conceptual block diagram of computer-program structure. Blocks A through D include the main body of analytical and computational work.

3.3.1 Block A, Initial Conditions

Rock Material Properties. The properties considered in the fracture and comminution model can be divided into two classes: (a) those properties associated with stress-wave propagation and attenuation in the rock and (b) those properties directly associated with comminution.

The properties associated with stress-wave propagation include the elastic constants, the density, the P- and S-wave speeds, and dynamic and static compressive and tensile strengths. Another parameter that can be considered is the nondimensional damping constant, Q. The fraction of elastic strain energy dissipated per stress cycle is $2\pi/Q$ (Reference 12). Because the interest is in the conversion of strain energy into surface energy of a new surface area, some estimate of absorbed energy is required as input to the comminution model. Although the Q concept was developed for low-amplitude, quasi-elastic wave propagation, its apparent association with solid-friction and grain-size concepts makes it attractive to apply at the stress levels considered.

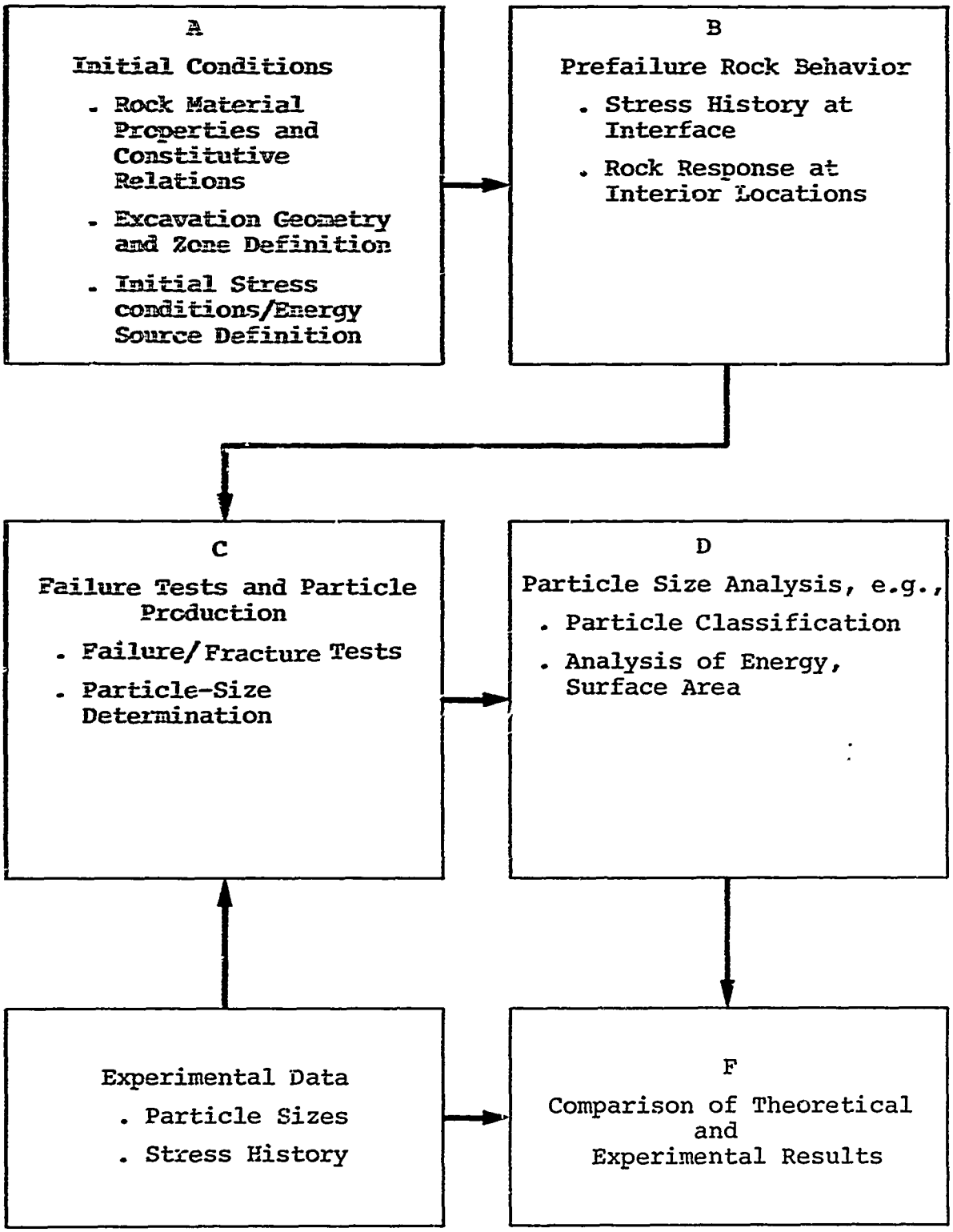

Figure 3 Schematic of fracture and comminution model structure.

Rock properties directly associated with comminution include specific surface energy, Bond work index, W_i, hardness, representative grain diameter, and natural fracture spacing and orientation.

Table 1 is a list of material properties that are relevant to comminution, with some representative numerical values typical of Westerly granite or similar granitic rocks. Not all of these properties were used in the program. The specific properties and values used in the test computations with the fracture and comminution program are tabulated later in this report.

Excavation and Specimen Geometry. In deciding on the geometry for these investigations, consideration was given to field-scale configurations of practical importance in fracture and comminution but of sufficient simplicity to lend themselves easily to laboratory and numerical simulation. Configurations considered included spherical and cylindrical cavities with and without adjacent free surfaces. A plane geometry was also considered; a small sector of the shock front at a large distance from a single source or from an array of sources would be approximately planar. Figure 4 shows several of these idealized geometries. Most of the computations were performed for the one-dimensional cylindrical borehole geometry. In some of the later computations a parallel free surface was introduced to test the Galin spall model. For computation the rock was divided into a specified number of discrete zones. The computer program calculates the stress history and particle size produced for each zone.

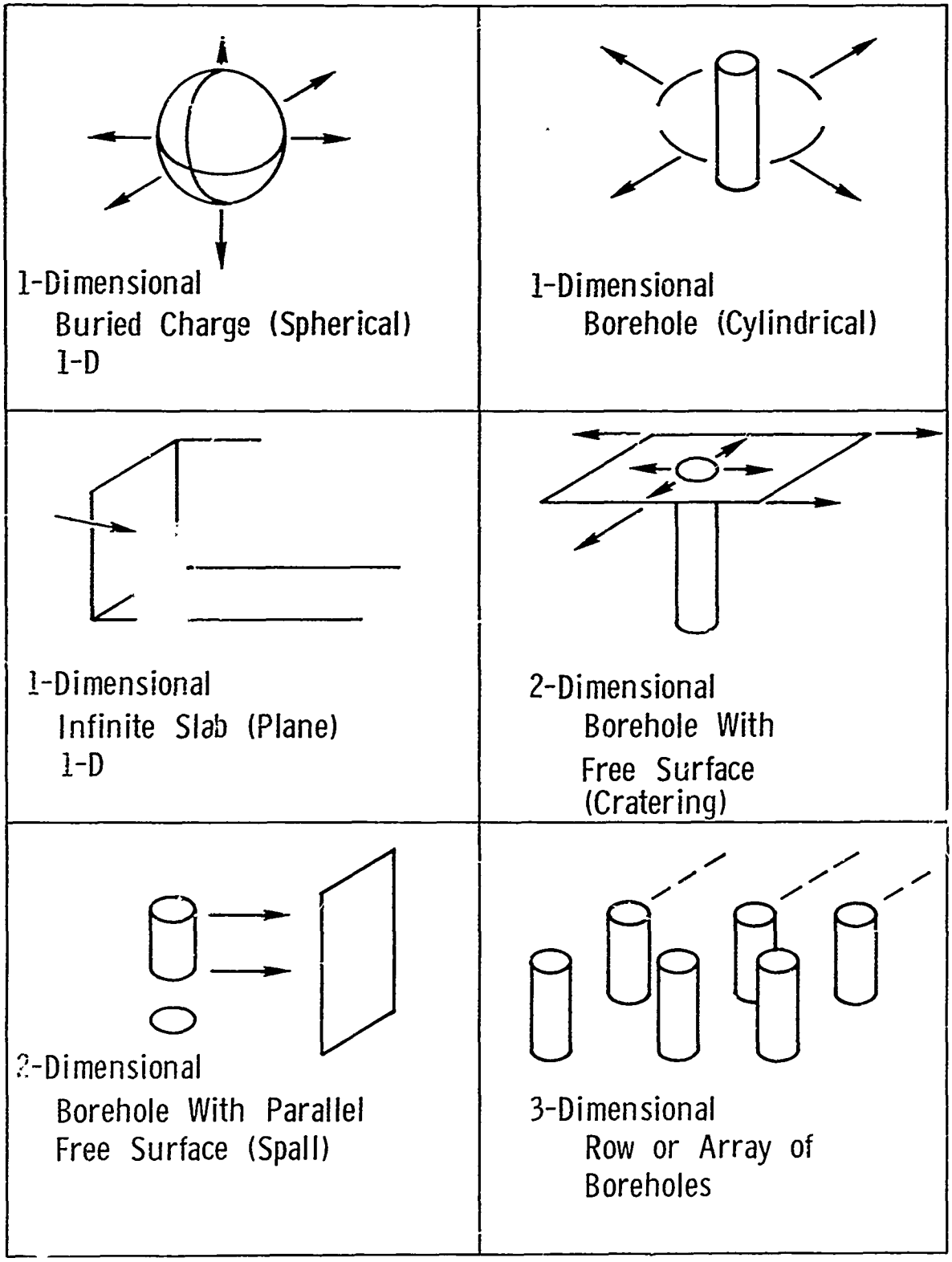

Figure 4 Material geometries.

TABLE 1

MATERIAL PROPERTIES RELEVANT
TO COMMINUTION AND REPRESENTATIVE VALUES

Property	Symbol Used in Text	Value
Density	ρ	2.65 g/cm^3
Young's modulus	E	7.5 x 10^{11} dyne/cm^2
Poisson's ratio	ν	0.25
Compressive strength	S_c	2 x 10^9 dyne/cm^2
Tensile strength	S_t	3.5 x 10^7 dyne/cm^2
P-wave speed	c_p	5.0 x 10^5 cm/sec
S-wave speed	c_s	3.0 x 10^5 cm/sec
Damping constant	Q	40
Specific surface energy	T	500 erg/cm^2
Bond work index	W_i	10 kwhr/ton
Penetration hardness	p	8 x 10^{10} dyne/cm^2
Grain size	-	0.075 cm
Natural fracture spacing	-	70 cm
Rittinger efficiency factor	K	0.01 (for grinding)
Crack propagation speed	-	1.88 x 10^5 cm/sec
Protodyakonov hardness	-	12 to 14 (kgf/cm^2)/100

Input Stress Conditions. The input stress condition corresponding to an explosive source in a cavity was used in the computations. The source was represented by an instantaneous pressure rise followed by a gradual decay. Such a source was simulated in the laboratory experiments by an exploding wire configuration. The analytic form of the source is described below.

3.3.2 Block B, Pre-Failure Rock Behavior

Stress History at the Cavity-Rock Interface. The energy input to the rock was specified by an analytic pressure-time history at the cavity-rock interface. The functional form of the pressure history used was an instantaneous rise to peak pressure, P_o, followed by a decay given by the difference of two exponentials. This form represents the stress-wave effect of a high-explosive source. The explosive-rock interface is assumed to be at a distance r_o from the origin of coordinates. The interface pressure is then

$$P\left(r_o,t\right) = P_o\left[Ae^{-a\alpha t} - Be^{-b\alpha t}\right]$$

where A, B, a, and b are nondimensional constants which may be selected to generate the desired wave form. The quantity $1/\alpha$ has the dimension of time and is a measure of pulse duration. Figure 5 is a graph of the input pulse shape (at r_o = 1 cm) used in most of the test computations. The figure also shows the pulse at r = 10 cm.

Rock Response at Interior Locations. The elastic response of the interior rock locations for a plane-wave geometry is simply the forcing function $p\ (r_o,t)$ evaluated at some coordinate r using the retarded time appropriate to finite wave speeds. Thus,

$$P\ (r,\ t) = P\left(r_o,\ t'\right)$$

where

$$t' = t - \left(r - r_o\right)/c_p$$

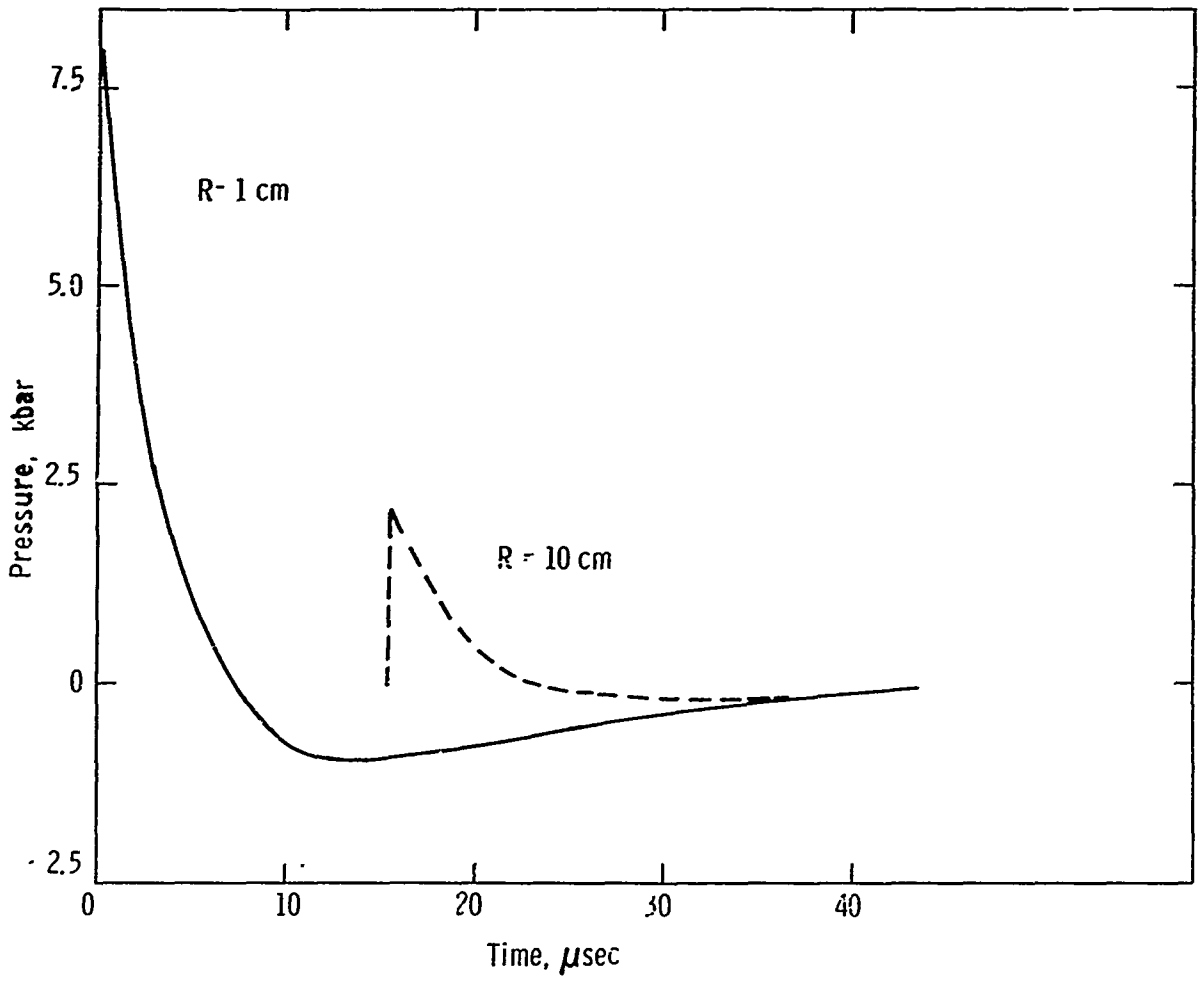

Figure 5 Pressure versus time at different distances (test 19).

and c_p is the P-wave speed. For other possible symmetries, cylindrical and spherical, there is a geometric amplitude attenuation so the final expression is

$$P(r,t) = P\left(r_o,t'\right)\left(r_o/r\right)^n$$

where n is 0, 1/2, or 1 for plane, cylindrical, or spherical symmetries. Figure 6 shows peak pressure versus distance in the three geometries for typical computations.

A solid-friction model of rock response was used to model energy absorption. In this model, peak stress attenuates according to a damping or dissipation constant, Q. The solid-friction model has been related to microfracturing and grain-size effects (Reference 13). It has been found (Reference 12) that a single crystal has a higher Q (lower dissipation) than an aggregate of crystals of the same material, suggesting that the dissipation depends on the surface or interfacial area of the crystals. Thus, the solid friction model is of particular interest for a comminution model that emphasizes creation of surface area. According to this solid-friction model, peak stress attenuates with distance according to the factor $\exp[-(r - r_o)/x_o Q]$ for a plane wave, where Q is the damping constant of the material, and x_o is the wavelength of an individual Fourier component. For the purpose of these computations, however, x_o was taken to be αc_p; i.e., if the wave travels a distance αc_p, it has attenuated by 1/Q. This is, of course, over and above any geometric attenuation. While this model is only an approximation of rock behavior, it reproduces some of the theoretical and observed characteristics of stress-wave propagation.

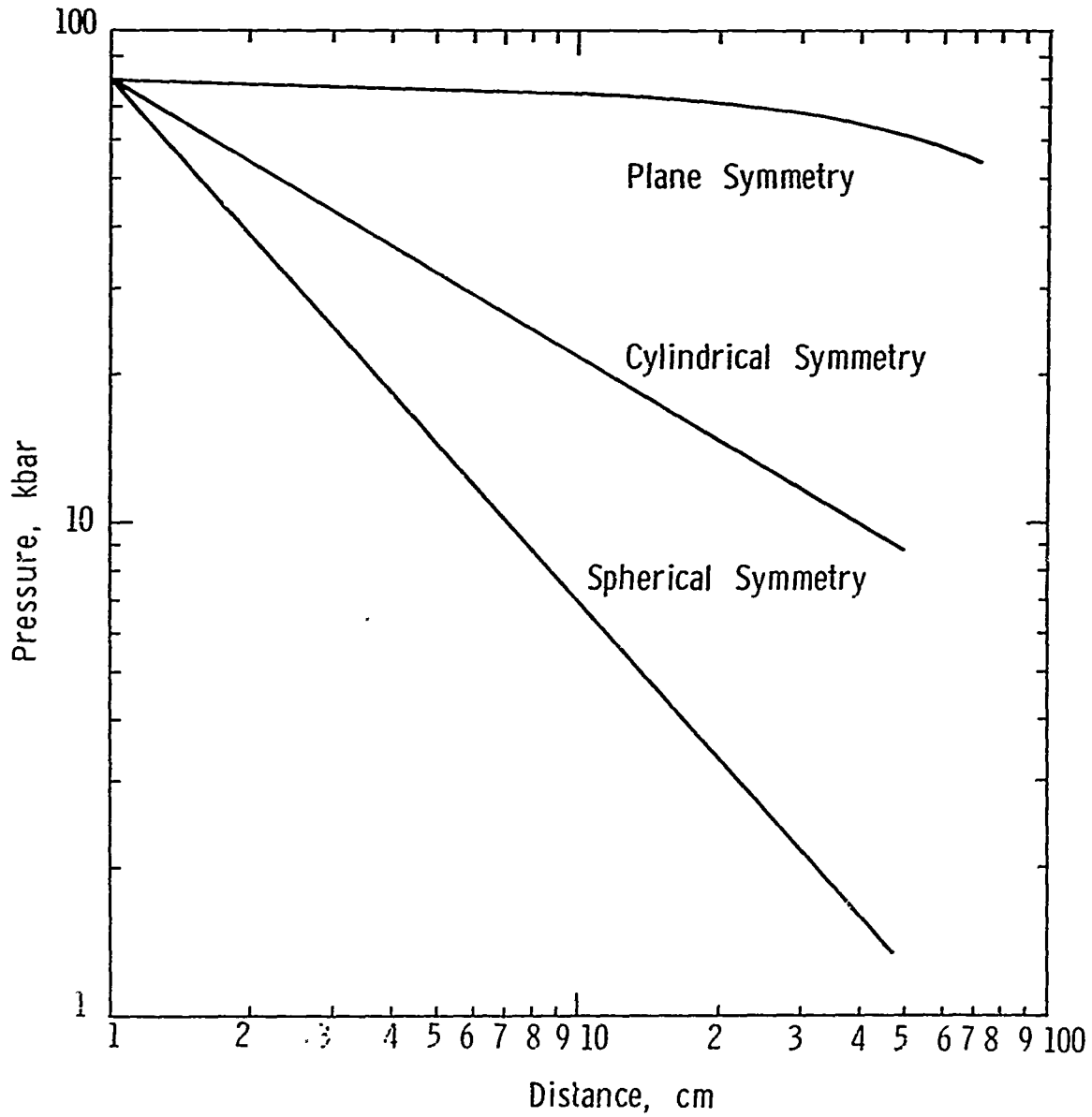

Figure 6 Peak pressure versus distance.

The values of the constants associated with the stress pulse profile were chosen so that the pulse consisted of a short compressive phase followed by a longer, lower-magnitude tensile phase. In cylindrical geometry, a close-in compressive failure is actually due to radial compression, while the tensile failure further out is due to hoop (azimuthal) tension. Typically the constants were chosen to produce both a region of compressive failure and a region of tensile failure.

The pressure, (elastic) energy density, and the accumulated absorbed energy density are computed in each space zone in a series of discrete time steps. The energy absorbed in compression while pressure exceeds the compressive strength is considered to be available for creation of surface area due to compressive failure. In the case of the Rittinger algorithm, the available energy is thus absorbed energy multiplied by the Rittinger efficiency factor. The energy absorbed during the tensile phase is treated similarly if the zone did not already fail in compression.

3.3.3 Block C, Failure Tests and Particle Production. The test for rock failure is a branch point in the procedural flow through the fracture and comminution program (Figure 3). At each time step, the pressure-energy conditions in each space zone are computed. If the result of the test indicates that the rock has failed, then the "comminution" subprograms of Blocks C and D are entered. If the rock in a zone has not failed, the pre-failure (Block B) computation continues. The failure criteria used in the program are the stress exceeding the compressive strength and/or the (negative) stress exceeding the

tensile strength of the rock. Typically, in the cylindrical-geometry computations, the compressive-strength criterion determines failure in the close-in region around the borehole. The tensile strength criterion determines failure in the more distant region, and also near an assumed free surface in tests of the Galin spall model.

Particle Size Determination. Once it has been determined that the rock has failed, one of the candidate comminution models is used to determine the particle size. The models incorporated in the computer program are those of Rittinger, Bond, and Galin. The formulations of the simplified versions of these models used in the program are described below. Both the physical description of the comminution rules and the associated algorithms are given.

Rittinger Surface-Energy (Reference 11):

Description: The energy required for crushing is proportional to the new surface area formed.

Variables:

f_a, f_v	area and volume shape factors
k	efficiency factor
ΔE	increase in available energy per unit volume
V	zone volume
T	specific surface energy
d	particle size

Particle size algorithm:

$$d = 6\ T\ f_a / k \Delta E\ f_v$$

If the material consists of pre-existing particles of size d_o, then the increase in energy is used to create only the additional surface area; so the new size d is given by

$$d_1 = d_o d/(d + d_o)$$

where d is as given above, so that $d_1 \leqslant d$. For in-situ comminution, an appropriate choice for the initial particle size d_o is the pre-existing fracture spacing.

The number of particles of size d is given by

$$N = V/d^3 f_v$$

since it is assumed that each zone contains particles of uniform size.

Bond Third Theory (Reference 11):

Description: The energy required for crushing is proportional to the square root of the new surface area formed.

Variables:

ΔE	increment of available energy density
W_i	Bond work index--the specific energy input required to crush a large sized particle to 100 μ
d_o	pre-existing particle size
d_1	new particle size
V	zone volume

Particle size algorithm:

$$\sqrt{d_1} = d_o \frac{W_i \sqrt{100\ \mu}}{W\sqrt{d_o} + W_i \sqrt{100\ \mu}}$$

The number of particles of size d is similarly given by

$$N = V/d^3 f_V$$

Galin Destruction-Wave Theory (Reference 8):

Description: That part of the stored (potential) elastic energy which is not kinetic is the energy required to form new surfaces.

For one-dimensional plane symmetry:

Variables:

- T specific surface energy
- σ stress normal to free surface
- E Young's modulus
- ρ density
- c P-wave velocity
- V zone-volume

Particle-size algorithm:

$$d = 6T/\frac{1}{2}\left[\frac{\sigma^2}{E} - \frac{\sigma^2}{\rho c^2} + 2\sigma\right]$$

The number of particles of size d is given by

$$N = V/d^3 f_V$$

3.3.4 Block D Particle-Size Analysis. The program structure described in Block D is intended to be capable of accepting experimental stress-history and particle-size data as well as input from Blocks A through C of the fracture and comminution model.

Particle Classification. The particle-size classification program is in essence a set of mathematical sieves; that is, the particle sizes calculated (Block C) or measured (Block E) are reassigned to a set of discrete size intervals.

The classification algorithm used is that a particle in Class j has a volume of v_j given by $v_j = Rv_{j-1}$. It is convenient to take the ratio R = 2, for simplicity in computation of agglomeration and of further comminution. (If R = 2, then when a particle of Class j breaks in two, two particles of Class j-1 are created.) In the test computations, however, the value $R = 2^{3/2}$ was used. This value is used in the Tyler and United States sieve series, in which the openings of successive sieves are in the ratio $\sqrt{2}$. Once the set of sieve sizes has been chosen, it is a simple matter to determine for a particle of size d the sieve number j such that

$$v_j \leqslant d^3 f_v < v_{j+1}$$

that is, the particle passes sieve j+1, but not sieve j.

3.3.5 Output Summary. Additional output of the program includes the cumulative size distribution in terms of mass, area, or volume, and the comminution efficiency, defined as the ratio of new surface energy to the input energy.

3.4 RESULTS OF COMPUTATION

A series of 24 test runs was made with the fracture and comminution program. Most of the inputs shown in Figure 7 were kept constant. (Figure 7 is taken from test 19.) The inputs were varied as follows.

```
 INPUT DATA   F4C TEST 19 DATA SAME AS 18  TEST FORMAT + CALL P WITH R - PD

     GEOMETRY
               G= 1.
            RMAX=  41. CM
              R0=   1. CM
                    40 ZONES
          PPRIN=  2.0
          FREESU=  1.0


     FORCING FUNCTION
                    PMAX =  .800E-02 MBAR
                    ALPH =  .200E+00 PER MIC.SEC
                      X0 = 4.70 CM
          INPUT TIME STEP =      1.00 MICSEC
                    BETA =  .100E+00 PER MIC SEC
                       A =  .200E+01
                       B =  .100E+01


     MATERIAL PROPERTIES
               DENSITY = 2.650 GM/CC
               YOUNGS MODULUS =  .750E+00 MBAR
               POISSONS RATIO =   .250
               DAMPING CONSTANT =  .400E+02
               ULTIMATE STRENGTH =  .200E-02 MBAR
               TENSILE STRENGTH = -.350E-04 MBAR


     COMINUTION PARAMETERS
               SPECIFIC SURFACE ENERGY =  .500E-09
               RITTINGER EFFICIENCY =  .100
               VOLUME SHAPE FACTOR =1.0000
               BOND WORK INDEX =  .955E-03
               SHAPA=6.0000
               DIAMIN=  .100E-02
               SIZRAT=  .283E+01
               JMAX=50
 NOTES FOR THE FOLLOWING COMPUTED DATA
     R = POSITION (CM)
     RMD = RITTINGER MEAN DIMENSION (CM)
     BMD = BOND MEAN DIMENSION (CM)
     SUFFIX P IMPLIES COMPRESSION
     SUFFIX M IMPLIES TENSION
     PB = MEAN OVERSTRESS (MBAR)
     TB = DURATION OF OVERSTRESSING
 ALL VARIABLES ARE SCALAR POINT FUNCTIONS


 BULK MODULUS =  .500E+00 MBAR
 SOUND SPEED =  .583E+00 CM/MICSEC
 COMPUTED TIME STEP = .1000E+01 MICSEC
```

Figure 7 Input data for fracture and comminution program.

3.4.1 Geometry. Plane, cylindrical, and spherical geometries were tested corresponding to G = 0, 1, 2, respectively. PPRIN was used to print or omit certain outputs. FREESU was used to test the Galin spall model.

3.4.2 Forcing Function. Runs 1 to 14 were made with PMAX = 80 kbar, and the later runs with PMAX = 8 kbar, except for 4 kbar in runs 16 and 23, and 2 kbar in run 20. Runs 1 to 10 were made with ALPH = 0.1 and BETA = 0.05. Runs 11 through 16, 18 through 20, and 22 through 24 were made with ALPH = 0.2 and BETA = 0.1. Runs 17 and 21 were made with ALPH = 0.4 and BETA = 0.2. Doubling the values of ALPH and BETA results in halving the length of the pressure pulse.

3.4.3 Material Properties. The material properties were taken as shown in Figure 7 for all runs except that compressive and tensile strengths were doubled in runs 22 through 24.

In addition to numerical changes in inputs, the program itself was revised during the series of test runs. Starting with run 9, energy available for comminution in each zone was taken as cumulated absorbed energy, while in earlier runs available energy consisted only of energy absorbed in the time step before fracture. Subroutine CLASIF was introduced starting with run 12 and the Galin spall-model option was introduced starting with run 18.

3.4.4 Representative Results. Figures 8 and 9 show the calculated particle size versus distance in spherical and cylindrical symmetry, respectively. The peak pressure at the cavity-rock interface (radius = 1 cm) was 80 kbar. The particle sizes shown were computed by the Rittinger algorithm. The sizes

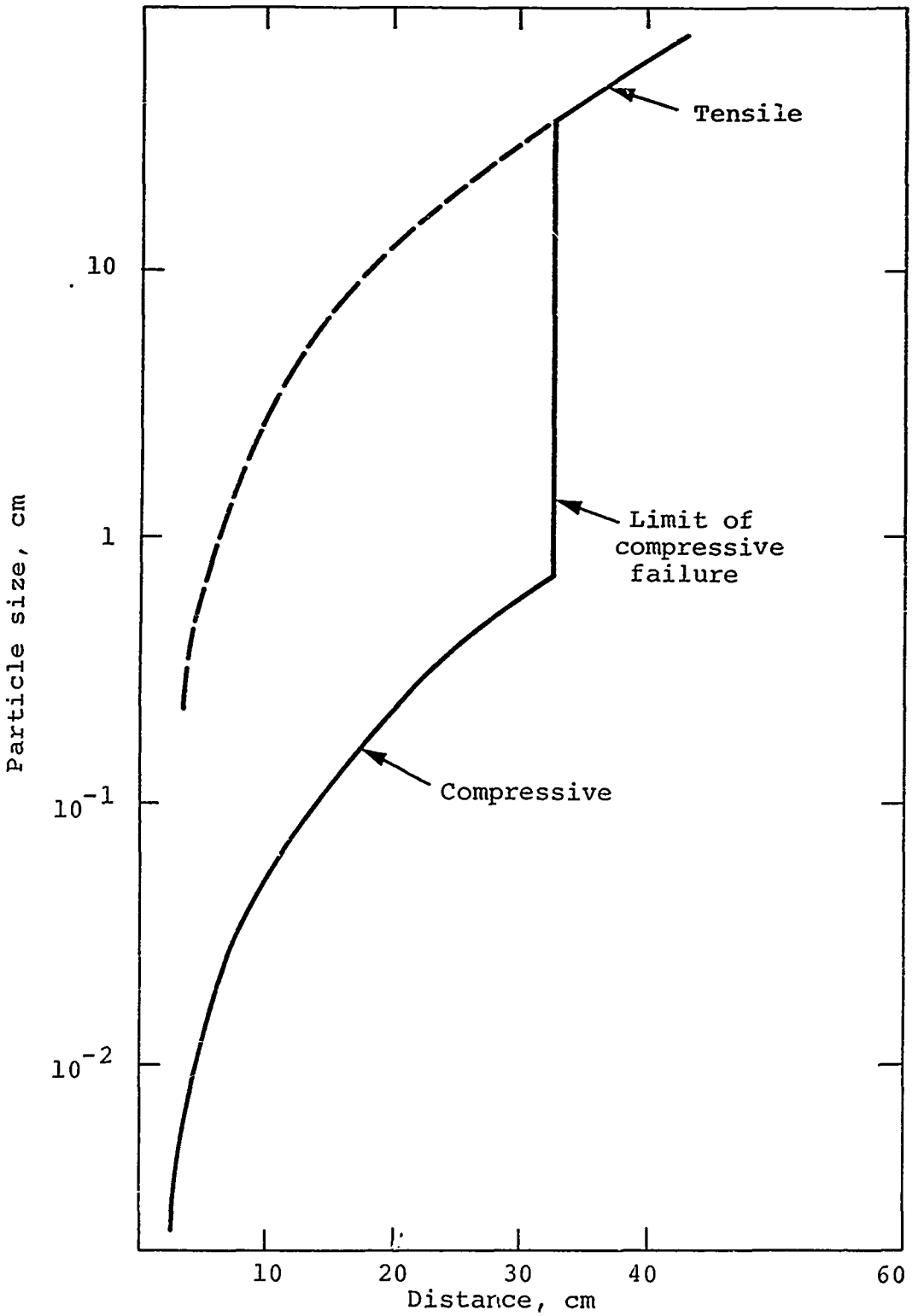

Figure 8 Rittinger particle size versus distance in spherical symmetry (run 2).

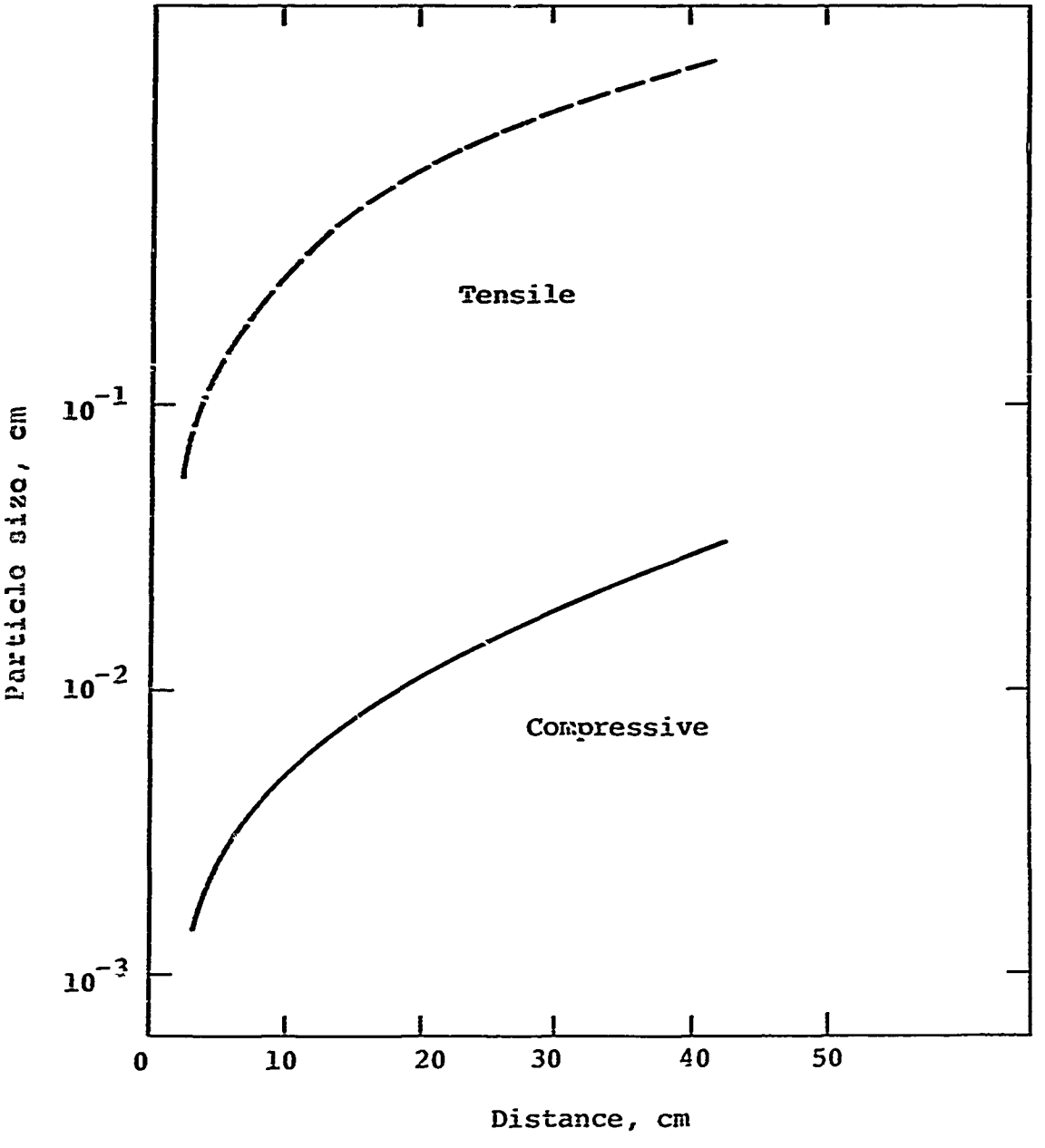

Figure 9 Rittinger particle size versus distance in cylindrical symmetry (run 3).

computed according to the Bond work-index algorithm were several orders of magnitude larger and are not considered realistic. Consequently, little attention was devoted to examination of the "Bond" results in later computer runs although the program still calculates and prints out both Bond and Rittinger sizes. More realistic Bond sizes could be obtained by choosing a much lower value of the work index.

Part of the "tensile" curves in Figures 8 and 9 is given by a dashed line. This line corresponds to regions that also failed in compression and the "compressive" curve is also shown. The dashed tensile curve can be interpreted as the size that would have been produced had the material not previously failed in compression.

The later runs were made with peak pressures of 8 kbar or less. Runs made with these values in cylindrical symmetry show both a close-in crushed region of fine particles and a farther-out tensile-failure region of much coarser particles.

The energy input to the wall in these later runs is of the same order of magnitude as that produced by the exploding wire experiments reported in Section 5. Run 15 used a peak pressure of 8 kbar. The elastic energy input, corresponding to the area under the pressure-time curve at the cavity wall, r = 1 cm, was about 6 joules/cm^2, using a value of bulk modulus of 0.5 megabar. The exploding wire experiments released about 650 joule/cm corresponding to 80 joules/cm^2 for a cavity diameter of 1 inch. For an air-filled cavity it was estimated that about 10 joules/cm^2 were coupled into the rock. Thus, the computational and experimental energy inputs were of nearly the same magnitudes.

Figures 10 and 11 show the particle sizes for runs 15 and 16, at peak pressures of 8 kbar and 4 kbar, respectively. Attention is called to the dashed line in Figure 11 captioned "Diameter = Distance." It is suggested that at a given radial distance a calculated particle size greater than that distance is unrealistic. Thus, at a radial distance of 20 cm a particle size greater than about 20 cm should probably be interpreted as indicating an unfractured region.

The size-classification subroutine CLASIF was first tested on run 12. Figure 12 shows the cumulative surface-area and volume distributions from run 15. The smoothed curves have been faired through the computed data points, which present a more irregular, zigzag appearance due to the coarse grid and size-classification scheme. The size distribution is divided into a fine component (less than 1 cm) from the compressive-failure region and a coarse component (greater than 3 cm) from the tensile-failure region. The "compressive" debris carries only 8 percent of the particle volume but 66 percent of the surface area, illustrating that a disproportionate amount of explosion energy is consumed in producing fines. The distribution is plotted on log-probability (log-normal) coordinates. Some distributions of explosively fractured material have been found to be approximately log-normal, and certain hypotheses about the grinding process result in a predicted size distribution that tends asymptotically to log-normal.

The Galin rock-burst model (called "spall model" in the figure) was tested on run 18 and later runs. Figure 13 shows results from run 14. The input conditions were the same as for run 15 except that the outer boundary, r = 41 cm, was assumed to be a free surface. Consequently the "compressive" and "tensile"

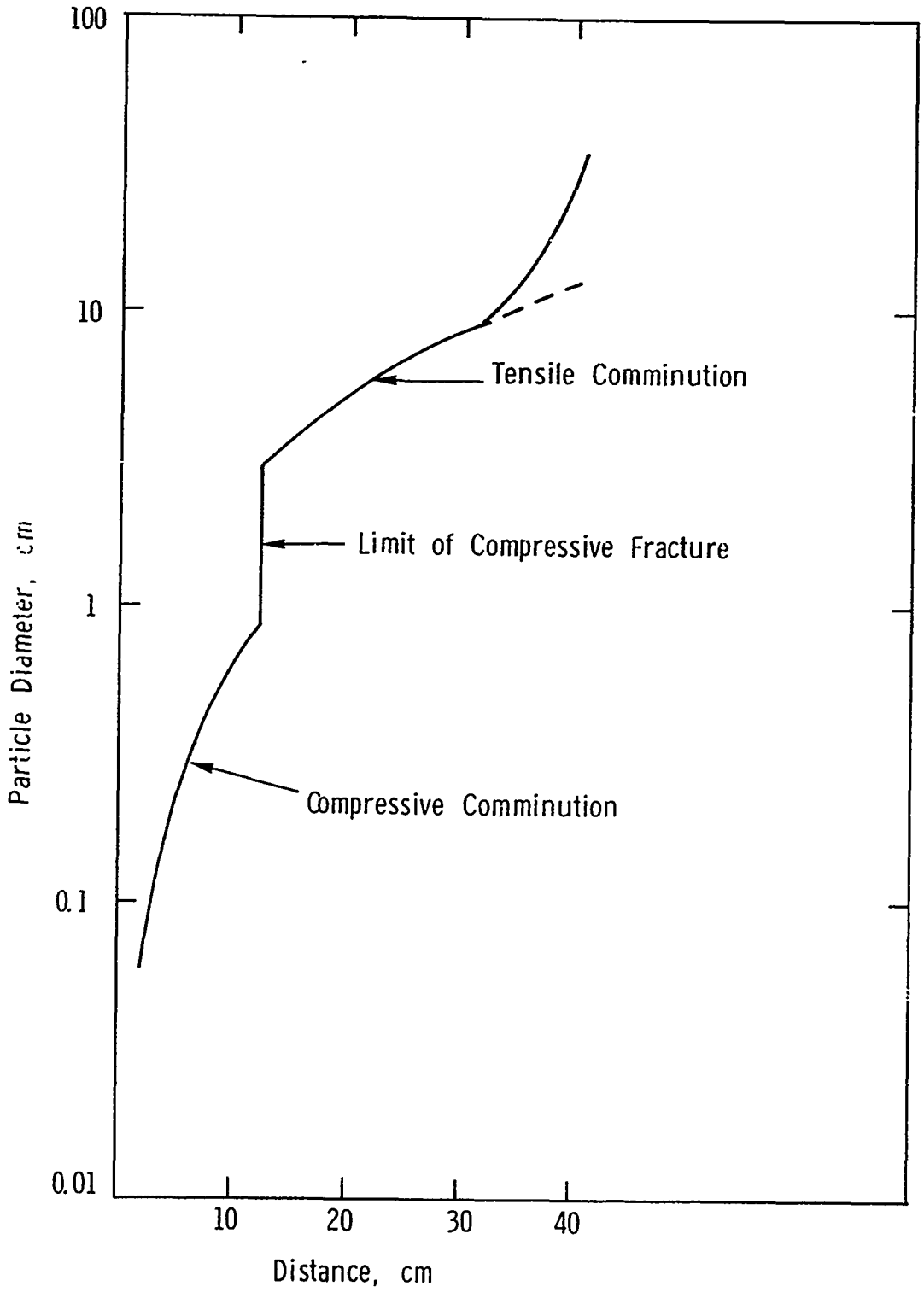

Figure 10 Test 15 (P_o = 8 kbar) Rittinger particle size versus distance.

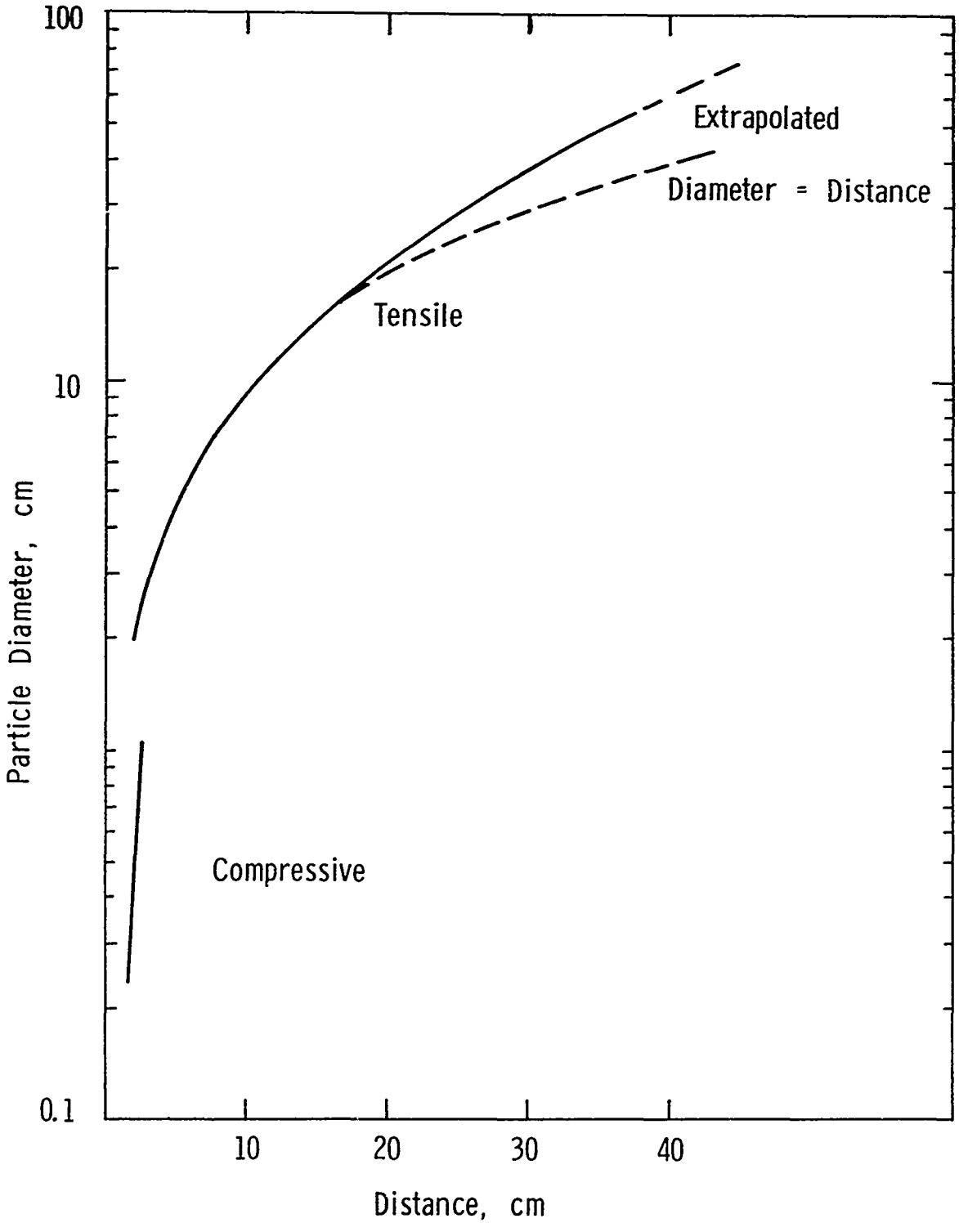

Figure 11 Test 16 (P_o = 4 kbar) Rittinger particle size versus distance.

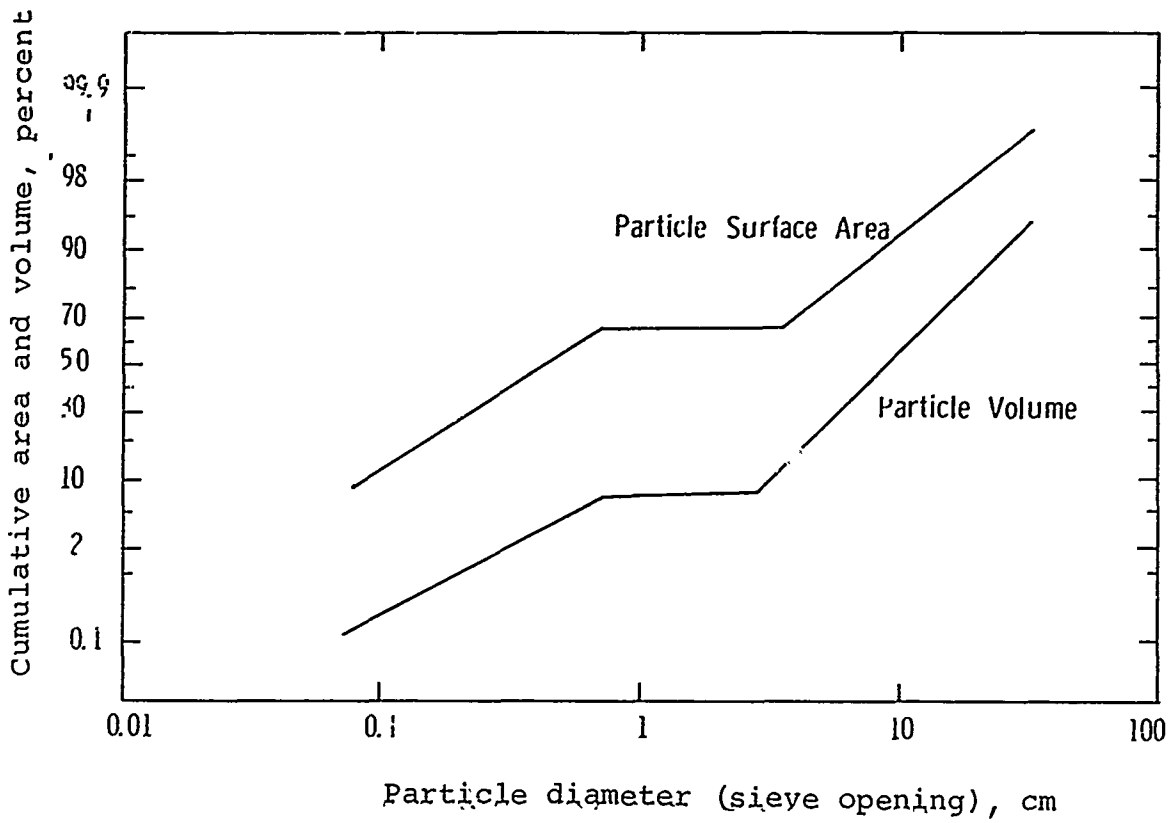

Figure 12 Test 15 cumulative particle size distribution.

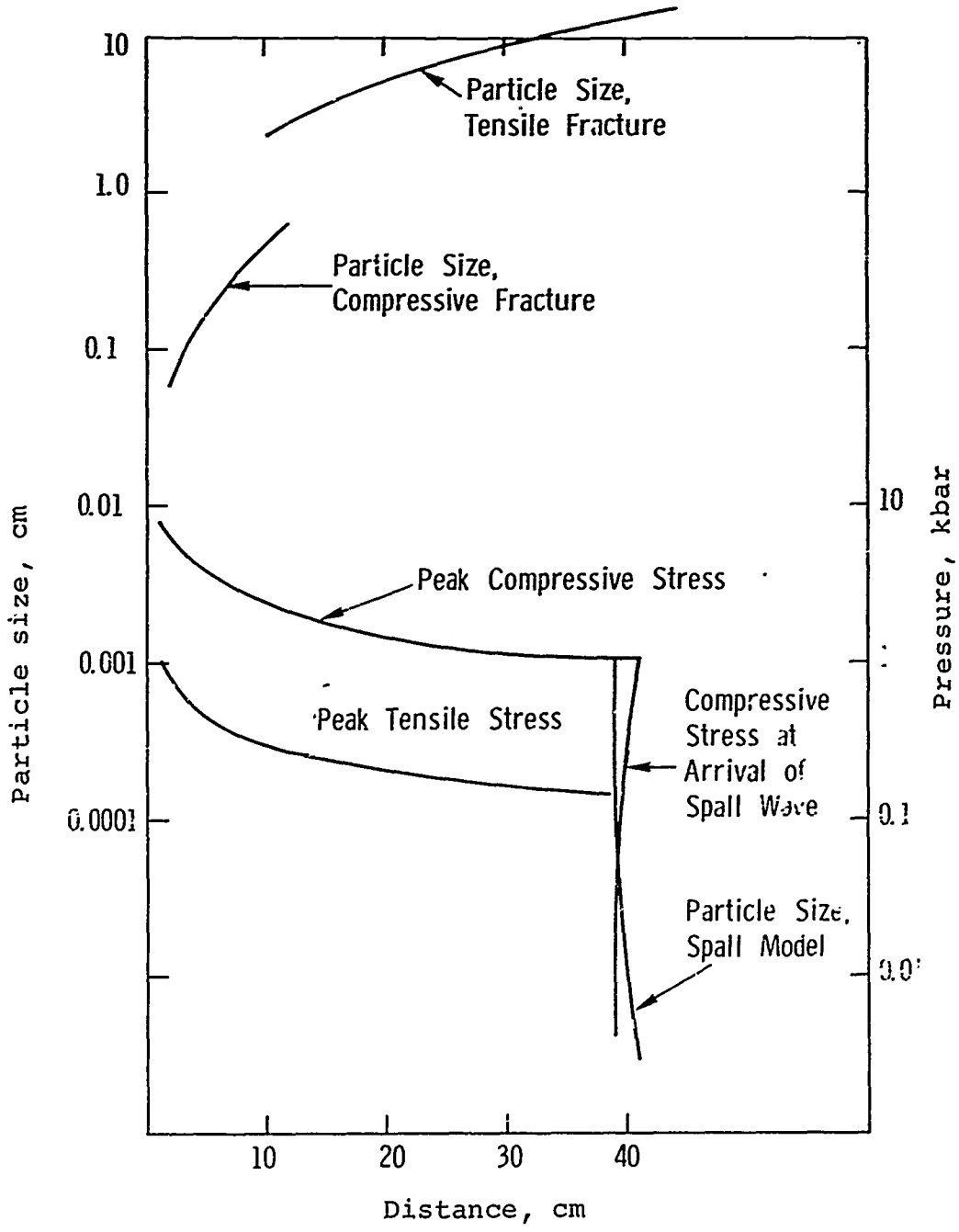

Figure 13 Test 19 (P_Q = 8 kbar) peak stress and (Rittinger) particle size versus distance.

sizes shown are the same as in Figure 10 although the coordinates are different. The "spall" sizes are extremely small, ranging up to a maximum of 0.001 cm at the point (r = 38 cm) where the in-running destruction wave is cut off by arrival of the tensile phase of the incident wave. An explanation for these unrealistic sizes is that the Galin theory assumes that elastic energy of compression is converted entirely to surface energy and kinetic energy of the fragments. It is likely that much of the energy is dissipated as waste heat either by irreversible distortion before spall occurs or by the dissipation of residual stress reverberations in the spalled fragments.

3.5 COMPARISON OF COMPUTED AND EXPERIMENTAL PARTICLE SIZES

The level of effort on this project did not permit extended comparison of computed and observed particle size distributions. Furthermore, the modeling effort emphasized development of a functioning model and program, which could subsequently be made more realistic. However, two measured particle-size distributions were available from PILEDRIVER, a nuclear explosion in granite (Reference 14). These distributions are shown in Figure 14, together with the calculated sizes from our run 19. The distributions show rather surprising and unpremeditated agreement. What is physically significant is perhaps the similar shape of the distributions. The distribution from run 19 consists of a small (8 percent by volume) amount of fines produced by compressive failure and a much larger amount of coarser, tensile-failure material. The PILEDRIVER distributions may be interpreted similarly. Since each PILEDRIVER sample was taken from a single location, however, it may be that both compressive and tensile processes operate successively at these locations. For instance, the comminution process may have consisted of an initial tensile failure, followed by frictional "grinding" movements which produced the small percentage of fines.

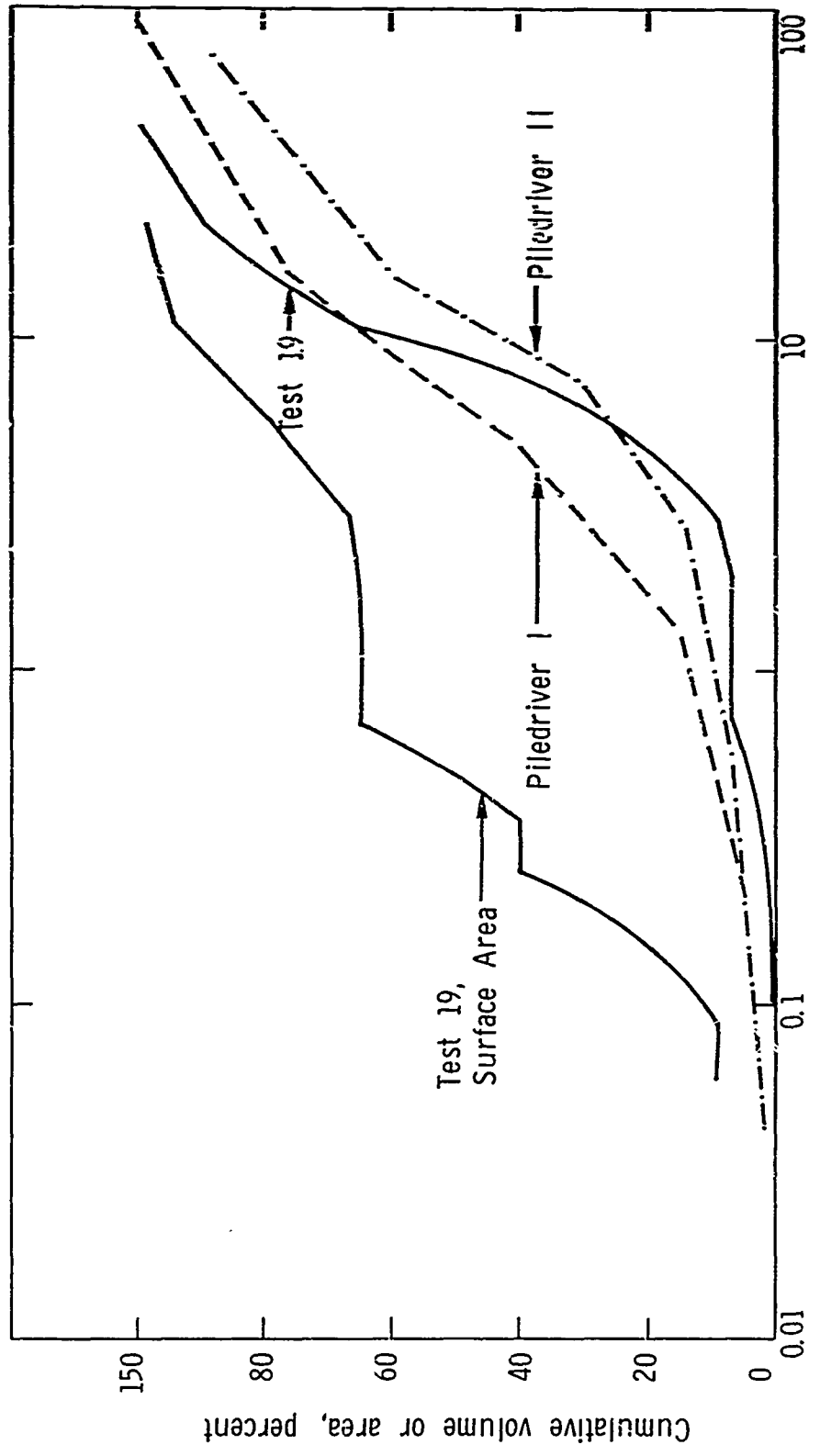

Figure 14 Experimental and computed particle size distributions.

3.6 DISCUSSION OF RESULTS

The development of the model and the results of computation have shown that many uncertainties stand in the way of obtaining detailed accurate results from a comminution model, if indeed such an objective is feasible. Some of these uncertainties relate to inherent variability in rock material properties and in the consequent rock response to a shock wave. These considerations are shown schematically in Figure 15. The stress and size curves shown are based, approximately, on run 19.

An upper limit on particle size is imposed by the natural fracture spacing in the rock. This spacing is represented by a horizontal line at about 70 cm in Figure 15. The portion, if any, of a calculated size curve extending above this line should be disregarded. For instance, if the "tensile" curve that is shown ending at size 10 cm and distance 38 cm extended up to size 70 cm, then it should be truncated at the 70 cm point.

A lower limit or at least a transition line on particle size is imposed by the grain size of the rock. This size is shown at 0.075 cm in Figure 15. The energy required to create a unit surface area is much greater when intra-granular (especially intra-crystal) fracture is involved than for fracture between adjoining grains. This is true even for a well-cemented rock. Thus, moving to the left on the "compressive" size curve, the curve should probably nearly level off at the grain-size line unless the peak compressive stress far exceeds the compressive strength.

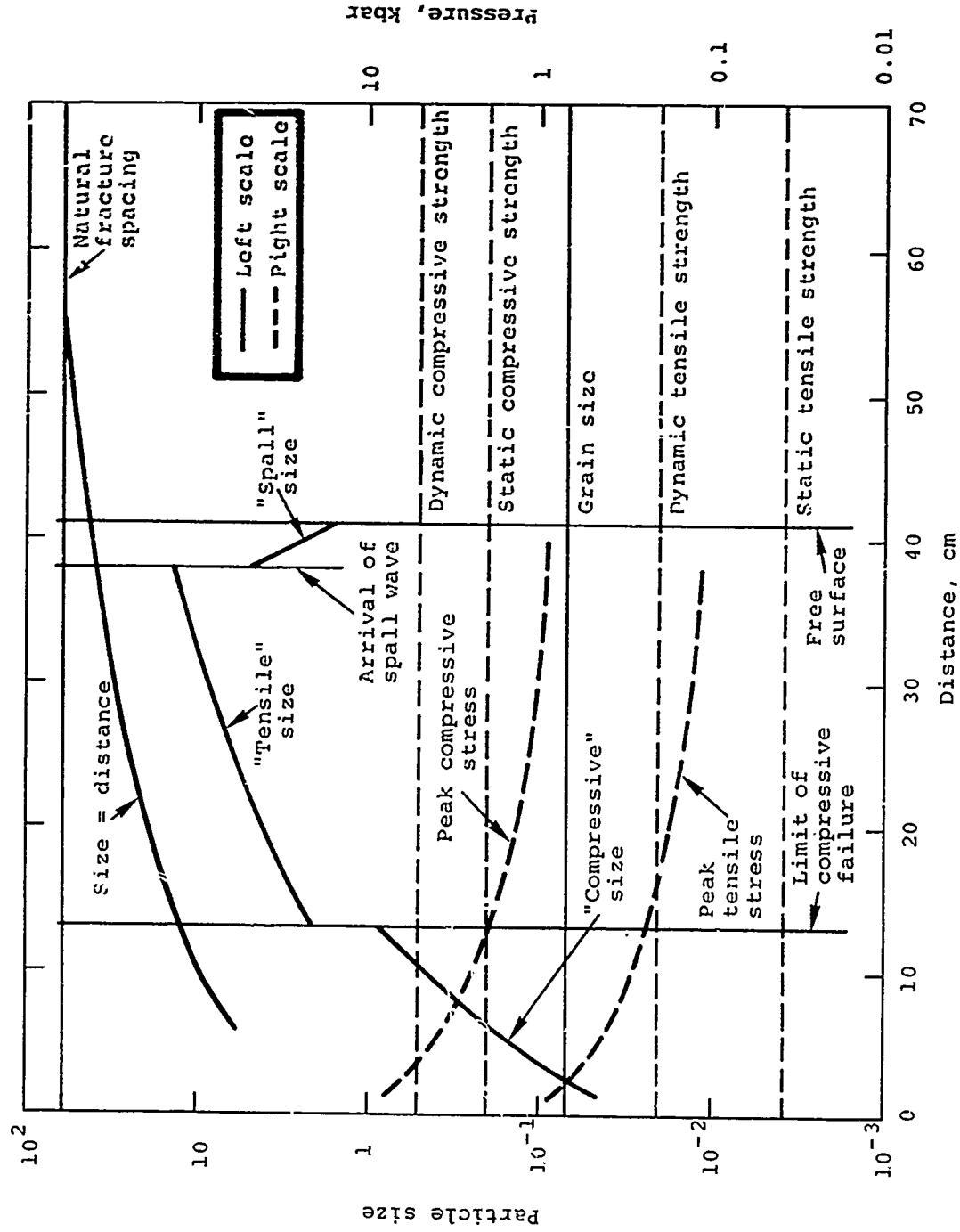

Figure 15 Conceptual diagram of interaction of comminution, material properties, and geometry.

The compressive and tensile strengths of rock vary between minimum "static" values and maximum "dynamic" values. The shorter and sharper the stress pulse, the more closely the effective strengths approach the "dynamic" values. In our computations, the "static" strengths were used. Thus, moving to the right on the "compressive" size curve, the curve ends at the distance (13 cm in the figure) at which the peak-compressive-stress curve intersects the horizontal, static-compressive-strength line, which is marked at 2 kbar (right scale). If twice as large a value of compressive strength were used, as on the line labeled "dynamic compressive strength," then a much smaller volume of crushed material would be produced by the same stress wave. In the illustration only material within a 3-cm radius would then be crushed instead of material out to 13 cm, because the peak compressive stress curve intersects the dynamic compressive strength line at 3 cm. Similar considerations apply to the value of tensile strength relative to the peak tensile stress.

The location of a free surface plays at least two parts in the interactions shown in the figure. First, the free surface puts an obvious limit on the amount of material fractured. Second, the "spall" or rock-burst wave, in the Galin model, travels in from the free surface and material near the surface may have already failed before the tensile tail of the incident wave arrives. In the figure the "tensile" size curve is shown truncated by a vertical line at the distance where the tensile wave meets the returning "spall" wave. Finally, the "size = distance" line discussed in reference to Figure 13 must be considered in relation to calculated particle size.

The foregoing considerations inevitably limit the accuracy of detailed particle-size prediction. It is suggested that most of the lines on Figure 15 should be replaced by relatively broad bands whose thickness is a measure of the variability of the material properties.

In summary, a simplified one-dimensional model of the dynamic comminution process has been developed; the model is clearly a long way from practical application. Any further development of the model should allow for statistical variations in material properties. Results should be compared with laboratory data on fracture and comminution under controlled conditions, as well as with large-scale field data. The assumed input pulse could be replaced by a calculated pulse form that is interactive with the assumed comminution mechanisms. Multi-dimensional stress effects must be allowed for. It is felt that the present effort has at least suggested the feasibility and usefulness of further development.

SECTION 4
MODELS OF COMPRESSIVE AND TENSILE FAILURE

4.1 FRACTURE MODELS IN NONLINEAR WAVE PROPAGATION COMPUTER PROGRAMS

In the previous section, the basic scheme for calculating fracture and comminution were described as well as several empirical schemes for determining particle sizes. However, when the elements of this fracture and comminution model are used in conjunction with a finite difference code, a different and more accurate approach to modeling these processes is possible. This approach is to model or describe the processes of fracture in sufficient detail to enable the interaction of fracture, an inherently nonlinear process, and the dynamic stress and velocity field causing fracture to be examined.

It is assumed that the fracture process influences the propagation of stress and strain. It is further assumed that certain aspects of asymmetric fracture can be modeled as a continuum process, thereby restoring symmetry and making it feasible to ignore one or more additional spatial coordinates. The first assumption is borne out by calculations using particular models of fracture. The second assumption is justifiable to the extent that experimental gauges, which typically subtend small angles from the source, can be expected to be representative. Certainly the influence of one major fault between source and measuring point is not well represented by this approach. With many fractures or fault lines (pre-existing fractures), however, reasonable results should be obtained.

There are three problems which can be addressed by the use of fracture models in nonlinear wave propagation computer programs:

a. dynamic fracture criteria

b. particle-size distribution

c. effect of fracture on wave propagation

The usefulness of dynamic fracture criteria is not limited to their application wave propagation programs, for they can point to relative efficiency of various fracturing techniques. Particle size distribution is difficult to estimate precisely with a one-dimensional program without certain assumptions as to the process of fracture. In the tensile failure model described below, it is assumed that the dynamic failure criterion is a critical tensile stress. Further, tensile stress relief from an open radial fracture is propagated normal to the fracture plane at finite speed. In the compressive failure model, particle size depends on mean stress at failure, as well as duration of applied stress. Ductile failure at the plastic flow limit does not cause fracture.

The effect of failure on subsequent wave propagation is governed by the constitutive relation for the failed (or pre-failed) material. For the tensile failure model, the material properties are dominated by crack formation and crack volume strain. The effect is to make the rock more easily compressible, so that propagation velocities are slower. For the compressive wave damage, the formation of microfractures as failure is approached slows velocities in a similar manner.

4.2 ACQUISITION OF CONSTITUTIVE RELATIONS DATA

Historically, two types of experiments of geologic materials have been performed to obtain data on the materials' constitutive relations. These are triaxial tests, where a cylinder of rock undergoes end and side stresses, and dynamic tests using diverging shock waves. Some recent examples of the first type include tests done by Swanson (Reference 15) and Swanson and Brown (Reference 16); examples of the second type include Kutter (Reference 17), and Kutter and Fairhurst (Reference 18).

The data extracted from these references show considerable nonlinear behavior of these rock materials. Figure 16, for example, shows the pressure-volume strain (or mean stress-total strain) measured in triaxial experiments on granite (Reference 15). This is clearly nonlinear volume behavior; further, the granite mean stress is not obviously a state property, in the sense of path independence. Fracture is also a nonlinear process, and the typical fracture patterns shown in Figure 31c which occur in the diverging shock experiments discussed later show changes in the rock structure. It has also been known (Reference 19) that the presence of randomly oriented cracks affects the bulk elastic properties. It is concluded that the process of fracture is not linear and also that fractured rock has different properties, when viewed in the large, than competent rock.

The study of the dynamics of fracture, and the intimate relationship of fracture and stress-wave propagation that is appropriate to blasting, then becomes greatly complicated by constitutive relations that would describe the material behavior. One of the several possible approaches is to use a general purpose, explicit, finite-difference computer program to solve the

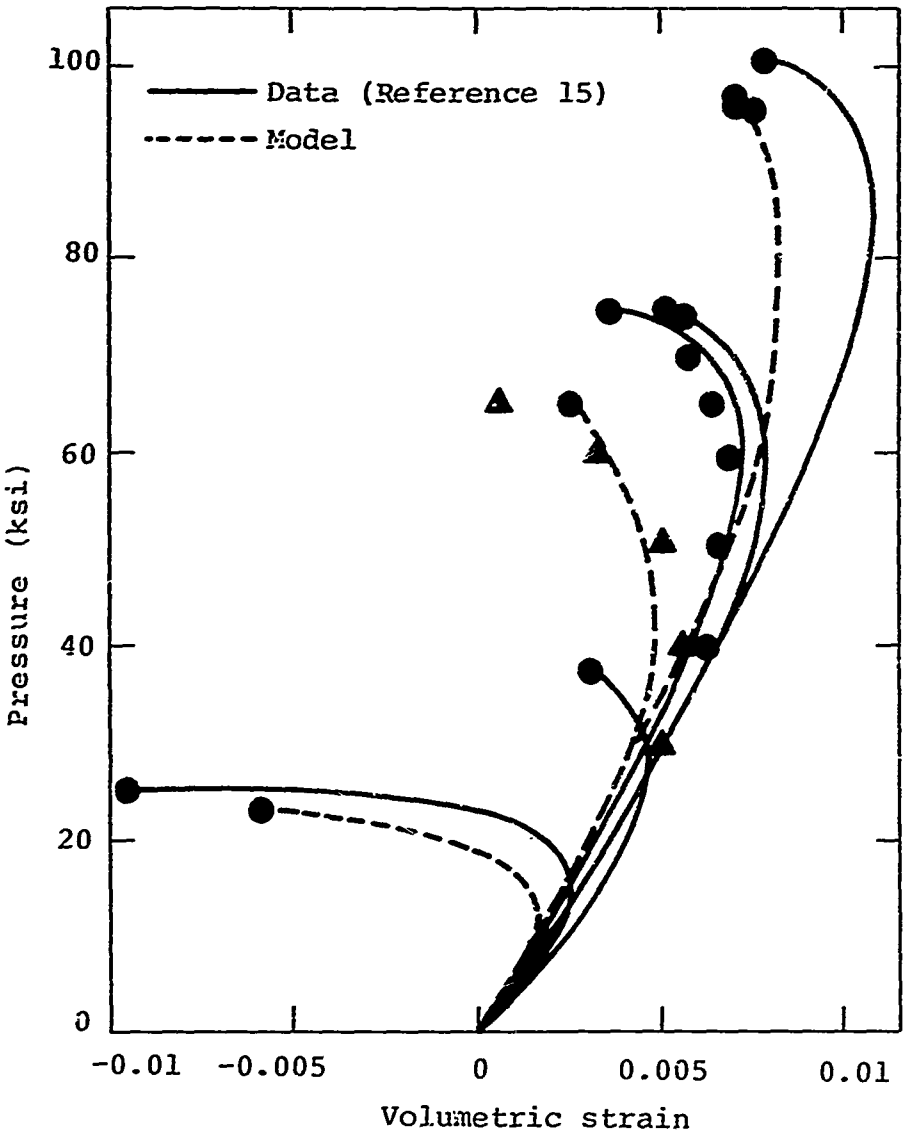

Figure 16 Volumetric stress-strain for Westerly granite.

equation of motion of a compressible, nonlinear solid. In the following paragraphs, models of material properties that approximate some of the effects shown previously will be described.

4.3 DILATANT MODEL FOR COMPRESSIVE FAILURE

A model has been formulated and used in calculations which exhibit dilantancy--a superficial volume increase of competent rock during compressive loading. It is assumed in this model that failure is independent of the intermediate principal stress, so that failure can be represented as a line on the plane whose coordinates are the first and second invariants of stress J_1, J_2. In what follows the yield stress in simple tension, $Y = 3J_2$, and the mean stress $P = 1/3\ J_1$ will be used.

Swanson's data (Reference 15) indicate that the failure surface is independent of path and that there are two surfaces Y_{fail} and $Y_{initial}$. The surface at which maximum dilatancy (for a given path) is produced and where catastrophic failure occurs is Y_{fail}. The surface below which no dilatancy occurs is $Y_{initial}$. A measure of the nearness to failure can be given by

$$x(P) = \left[\sqrt{3J_2} - Y_{init}(P)\right] / \left[Y_{fail}(P) - Y_{init}(P)\right]$$

Thus $x(P)$ is the fractional penetration of $\sqrt{3J_2}$ into the region between $Y_{init}(P)$ and $Y_{fail}(P)$. This meaning is illustrated in Figure 17.

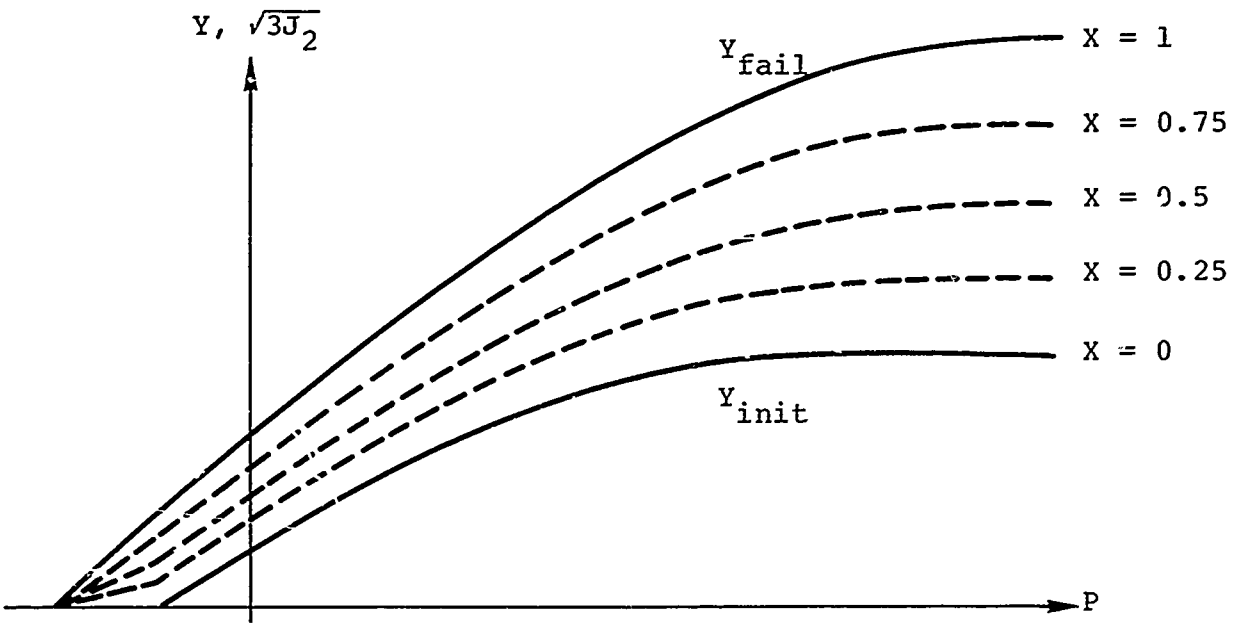

Figure 17 An illustration of the meaning of the parameter X (P) used in the compressive failure model.

It is assumed that the dilatancy is caused by the formation of microcracks during loading. It is useful to imagine that the number of microcracks produced on a given path is proportional to the maximum of $f(x) \cdot g(P)$ on this path where $f(x)$ and $g(P)$ have the properties:

$$\begin{aligned} f(x = 0) &= 0 \\ f(x = 1) &= 1 \\ g(P \leqslant 0) &= 1 \\ g(P > P_{plas}) &= 0 \end{aligned}$$

where P_{plas} is the pressure beyond which microcracks are not formed during failure. This occurs at the von Mises limit where $\partial Y_{fail}/\partial P = 0$. For this model, P_{plas} is an adjustable parameter. The functional forms of $f(x)$ and $g(P)$ will be given later for a fit to Swanson's Westerly granite data.

It is imagined that each microcrack has an associated volume which is compressible according to $\Delta V(P) = \Delta V(0)h(P)$, where

$$\begin{aligned} h(P) &= 1 \text{ at } P \leqslant 0 \\ h(P) &= 0 \text{ at } P > P_{limit} \end{aligned}$$

where the pressure P_{limit} is sufficient to close the microvolumes completely. Then the dilatant volumetric strain associated with a current pressure, P, and a past history value of $[f(x') \cdot g(P')]_{max}$ is given by

$$dV\left\{P,[f(x') \cdot g(P')]_{max}\right\} = dV(0,1) \cdot h(P) \cdot [f(x') \cdot g(P')]$$

where dV(0,1) is a material constant and the pressure, P, in the presence of dilatancy is consistent with P(V - dV,E) where P(V,E) is the corresponding pressure without dilatancy. Thus pressure is computed on the basis of rock strain, not superficial strain. This is similar to the way pressure is calculated in models of porous materials (Reference 20).

The fit to Swanson's data for uncracked Westerly granite was made with no regard to flow rule. In particular, the work-hardened yield surface was made a function of total distortional energy for coding convenience.

Work-Hardened Yield Surface:

$$\tilde{Y}_{WH} = \begin{cases} 0.000414 \text{ (Mbar)} & \text{if } Z \leq 0 \\ 0.000414 + 0.661\ Z & \text{if } Z > 0 \end{cases}$$

where $Z/\rho_o = Z/2.65$ is the total distortional energy in units of 10^{12} ergs/gram consistent with the code standard Mbar-cm-μsec units.

The function $f(x)$ was

$$f(x) \quad \begin{cases} 0 & \text{for } x \leq 0 \\ 0.015\ (0.015/1.015)^{(1-x)} - 0.015 & \text{for } 0 < x \leq 1 \\ 1.0 & \text{for } x > 1 \end{cases}$$

g(P) was

$$g(P) \quad \begin{cases} 1 & \text{for } P \leq 0 \\ 1 - \dfrac{P}{0.013} & \text{for } 0 < P \leq 0.013 \text{ Mbar} \\ 0 & \text{for } P > 0.013 = P_{plas} \end{cases}$$

h(P) was taken as

$$h(P) = \begin{cases} 1 & \text{for } P \leq 0 \\ 1 - \dfrac{P}{0.030} & \text{for } 0 < P \leq 0.030 \text{ Mbar} \\ 0 & \text{for } P > 0.030 \text{ Mbar} \end{cases}$$

The maximum volumetric strain was

$$dV\ (0,1) = 0.015$$

The values of D_{max}, x, and f in the region between Y_{fail} and Y_{init} are mapped in Figure 18. It can be seen that driving to Y_{fail} near P = 13 kbar will not result in dilatancy because $[f(x) \cdot D_{max}(P)]$ is small. Driving to Y_{fail} near P = 0, however, gives the maximum effect as $[f(x) \cdot D_{max}(P)] \rightarrow 0.015$. These results are consistent with Swanson's data and form the basis of the conceptual model. The various parameters were finely adjusted to give reasonable agreement over the range of Swanson's data. The extent of agreement is shown in Figure 17.

4.4 TENSILE CRACKING MODEL FOR DIVERGING GEOMETRIES

The basis for this model is a simplified picture of the process of fracture in cylindrical geometry, and it is assumed that all failure is by hoop tension. For example, at the inner radius of a cavity, the local tensile strength is exceeded and a flat crack forms (Figure 19). A relief wave is propagated normally from this crack, and during a time δt it will have progressed a distance $\delta \ell$ given by

$$\delta \ell = c_p \, \delta t$$

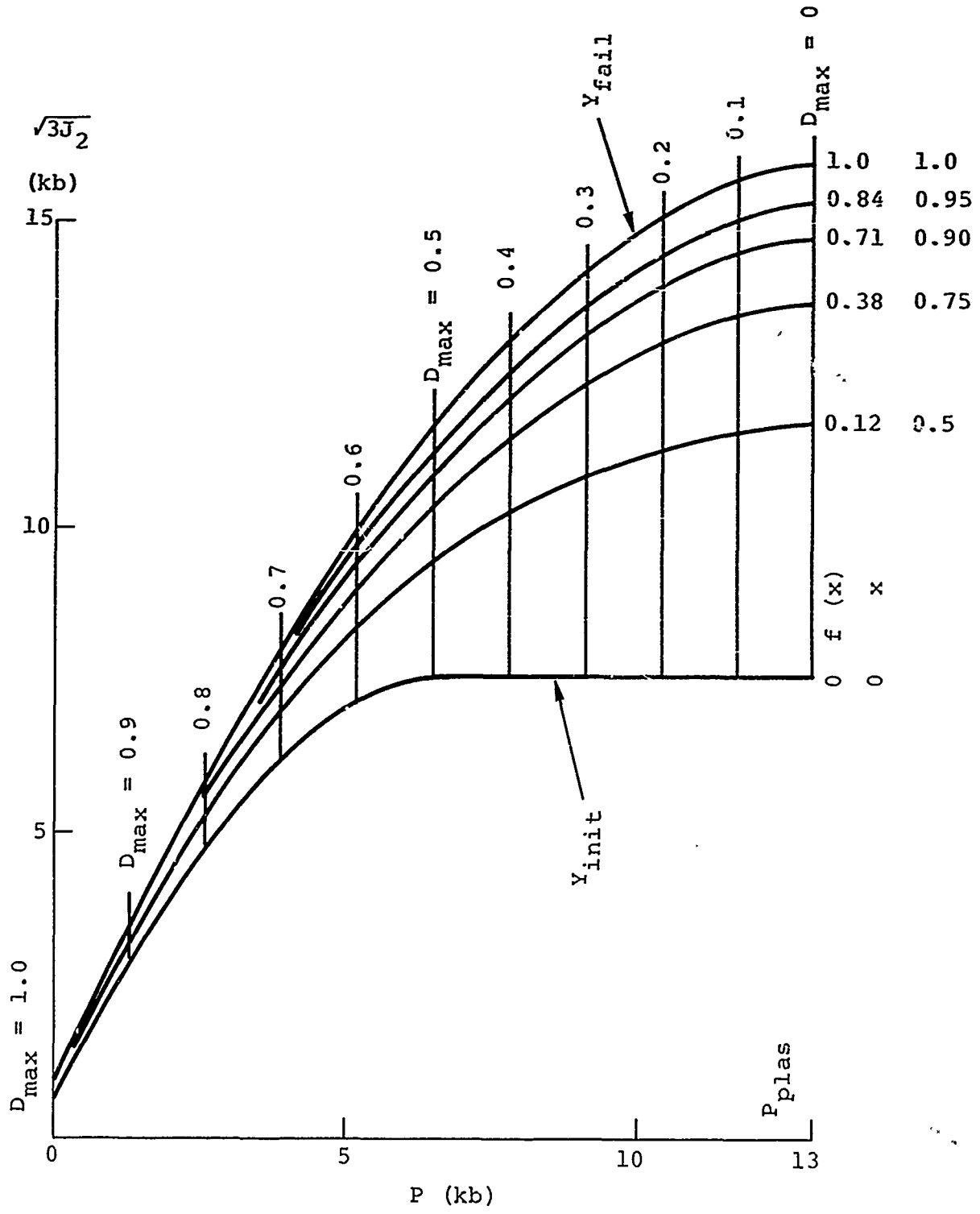

Figure 18 D_{max}, x and f map in Y, P space.

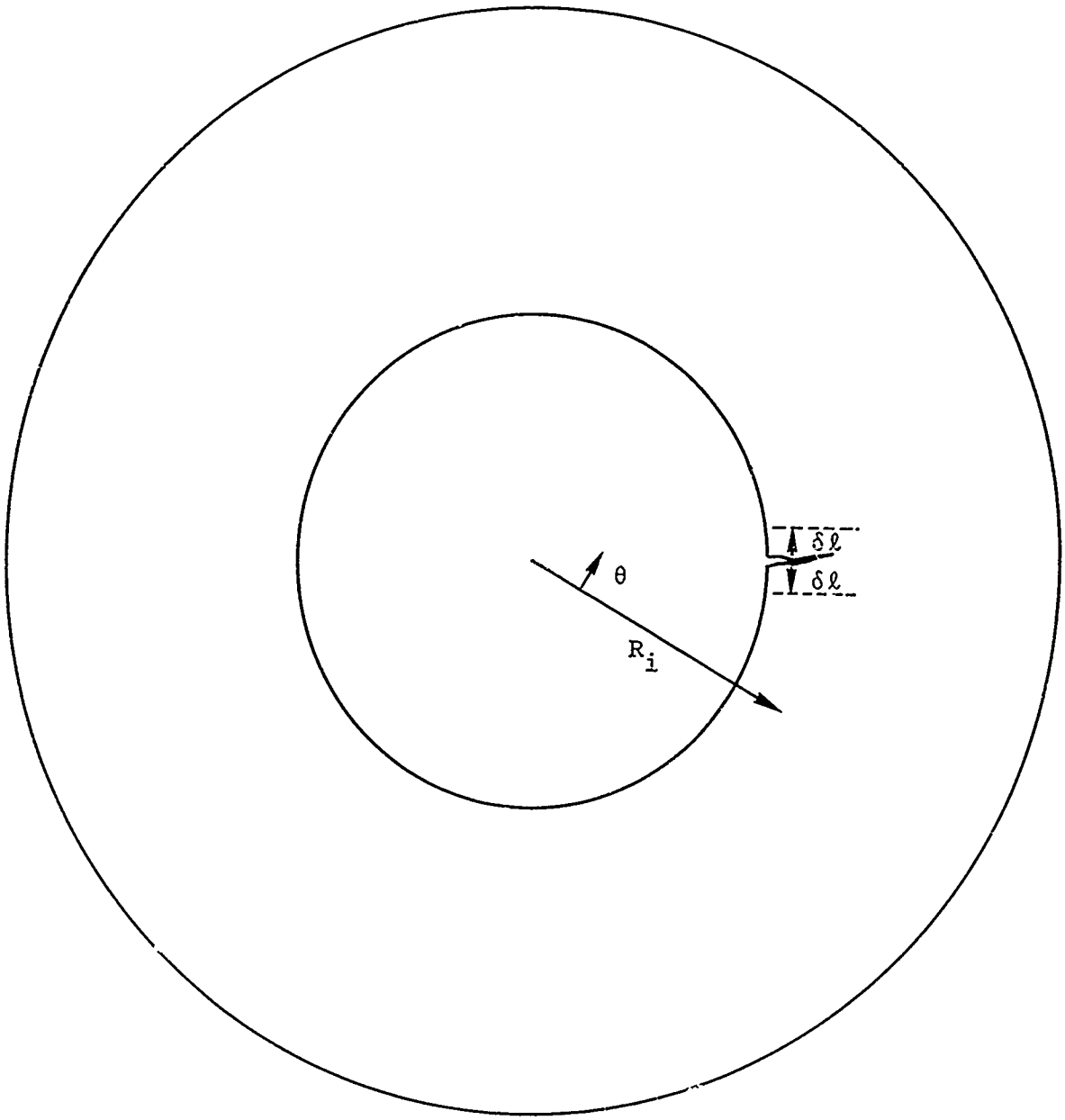

Figure 19 Flat crack formation.

where c_p is the longitudinal (elastic) sound speed. The hoop stress averaged over the circumference at a radius R_i, then, has decreased by a fractional amount proportional to $\delta\ell/\pi R_i$. At some other location, then, if the tensile strength is still exceeded, another crack can form and relieve more of the circumference.

In the process of tensile stress relief, a crack opens and this void strain, although part of the superficial volume, is not part of the rock strain for which elastic constants are appropriate. This strain is assumed to be only in the θ-direction, and is just the ratio of the stress relieved to the elastic modulus $(\lambda + 2\pi)$. This hoop strain affects the other stresses, however, so that although the rock retains a radial stiffness it is weakened in the hoop direction.

For consideration of smooth changes in numerical solutions, it is assumed that the hoop stress is relieved exponentially with a time constant given by twice the propagation time (along the circumference) between cracks. It is assumed that cracks form symmetrically at the points farthest from the last cracks to form, as long as the stress averaged over a circumference exceeds the tensile strength. Thus for purposes of the computation, the time constant is given by the average spacing and the exponential approach smooths out asymmetries as would be appropriate to the average response of many gauges spaced on a circumference.

Several calculations have been made with a one-dimensional Lagrangian finite difference code, PISCES^{TM} 1D-L (Reference 4) using this model of fracture. The first calculations were a pre-experiment simulation to obtain reasonable size and spark pulse requirements for the experimental part of this program.

The results of one such particular calculation are shown. The simulation geometry was a one-inch-diameter cavity with a pressure history on the wall given by

$$P = P_o e^{-t/\tau}$$

where P_o = 1 kbar, τ = 5 μsec and a tensile strength of 80 bar (1150 psi) was assumed. Calculated hoop stresses were recorded at 1.6 and 4 cavity radii, and are shown in Figure 20. The much slower decay of tensile hoop stress at the outer radius is a result of much larger crack spacing. This spacing as a function of radius is shown in Figure 21. When no cracks are formed, the spacing is recorded as the circumference (in centimeters).

Actual data on the tensile strength of rocks is very scarce. To add to the existing data, a series of experiments was performed in bore-hole geometry using an exploding wire to generate low compressive stress and thereby limit damage to the specimens to tensile fracture only. The experiments and their interpretation using the tensile crack model are described in the following section.

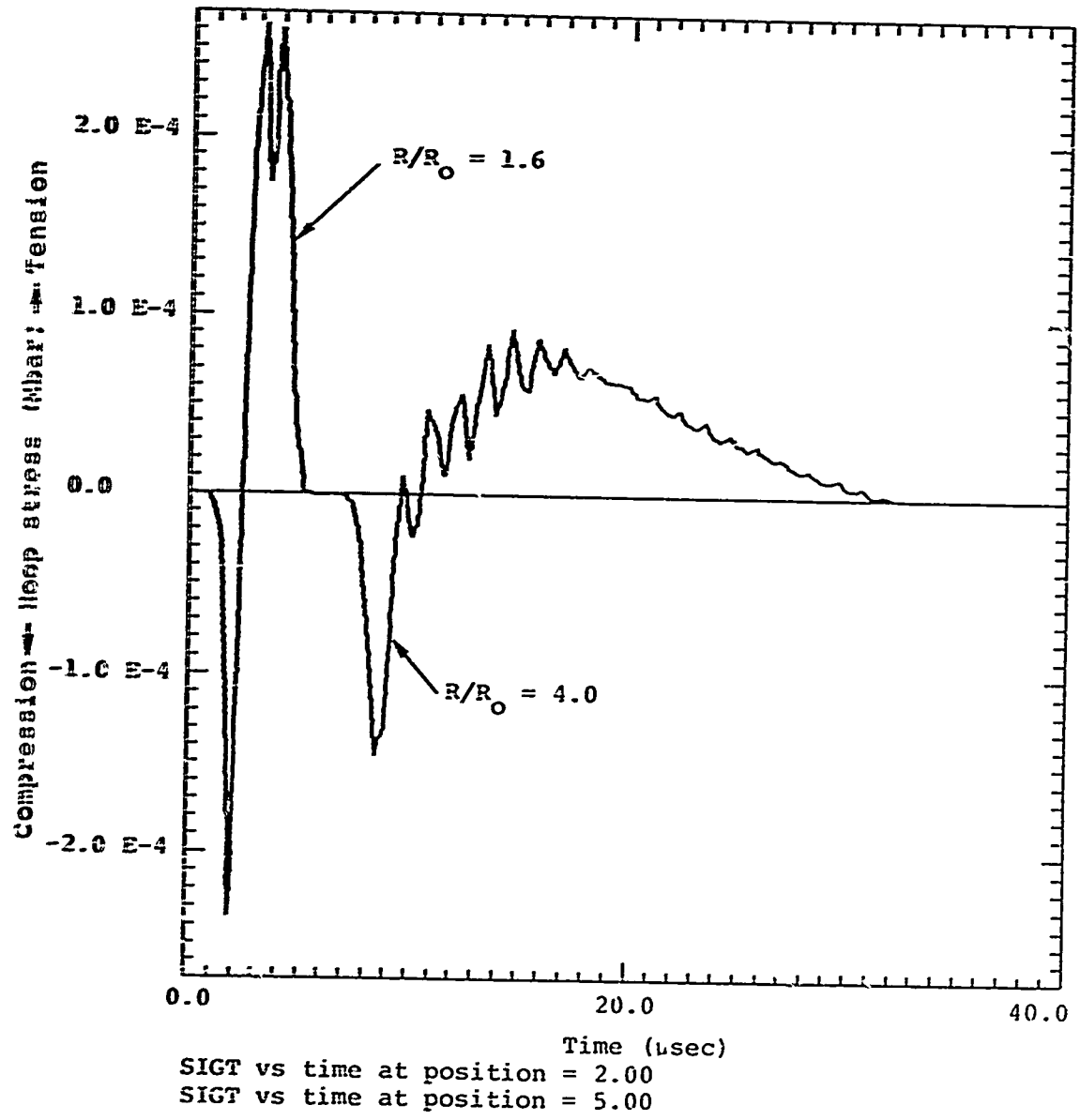

Figure 26 Hoop stress (σ_θ) versus time at two distances from a cylindrical cavity.

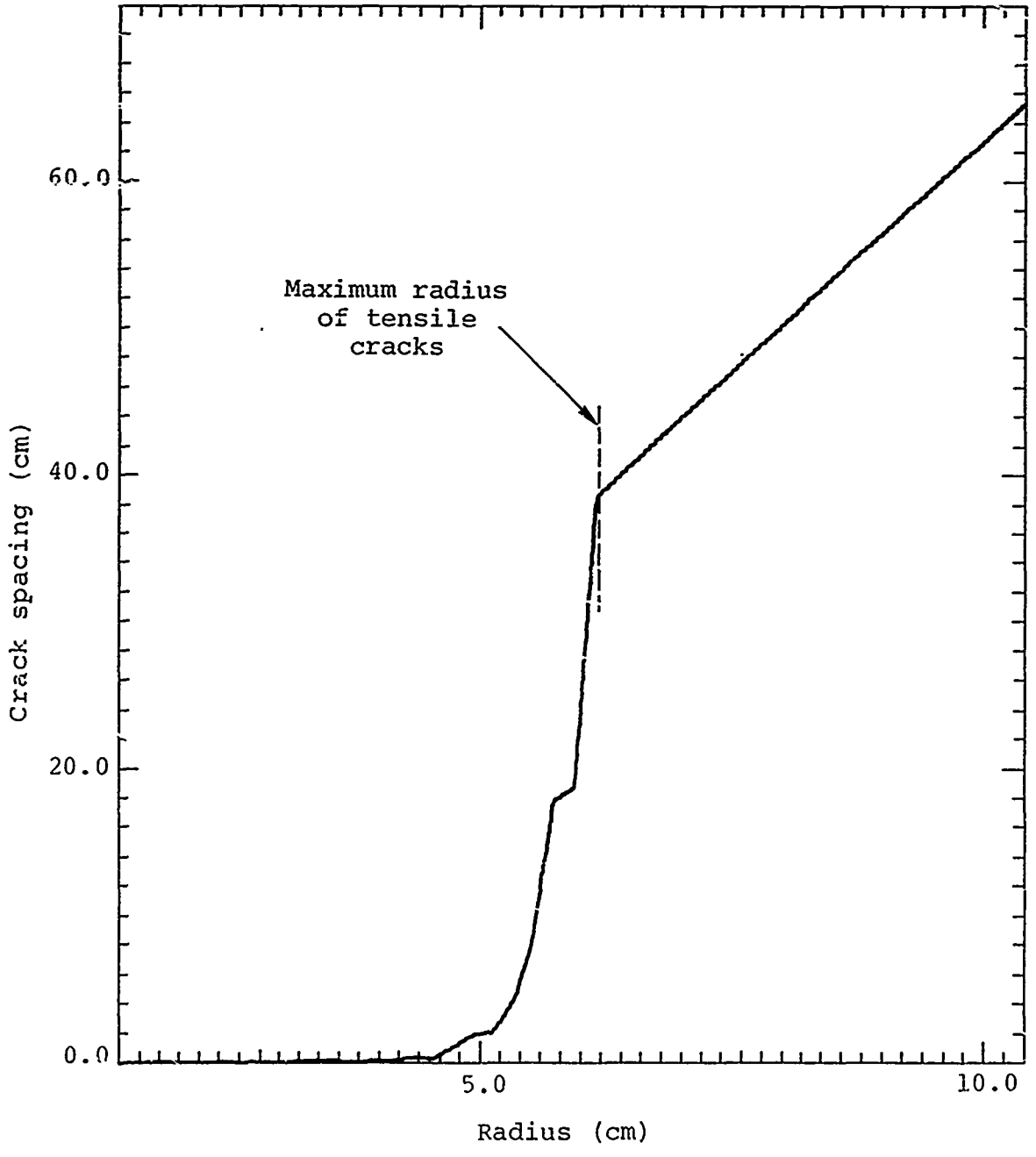

Figure 21 Crack spacing as a function of radius from a cylindrical cavity.

SECTION 5
EXPERIMENTS ON WESTERLY GRANITE

5.1 TECHNIQUE TO GENERATE TENSILE FRACTURE

The experimental effort on this program was directed toward studying the dynamic tensile failure of rock. A divergent (cylindrical) geometry was chosen because it corresponds to a typical geometry used in blasting operations. An exploding wire was used as a source to generate cylindrical stress waves into rock samples, causing radial tensile failure. In a normal blasting configuration, where high explosives are used as the energy source, the region near the borehole is fractured in compression by the high stresses. At larger radii, however, the peak compressive stresses are not large enough to cause failure, but rather fracture occurs because of hoop tensions generated by the divergent material motion. Because the exploding wire technique is essentially a low-peak-stress energy source, the compressive failure region can be eliminated, thus allowing one to concentrate solely on the tensile failure behavior of the rock material.

The technique employed here using the exploding wire to study dynamic fracture behavior is similar to a technique used extensively to study the material response of hollow cylindrical samples to cylindrical stress waves (References 21, 22, and 23) and the dynamic buckling of long cylindrical shells (Reference 24).

By placing a wire along the axis of a cylindrical cavity (Figure 22) and vaporizing it with energy released rapidly from a capacitor storage system, an axisymmetric disturbance can be generated which propagates through the medium surrounding the wire to impinge uniformly on the cavity wall, thus inducing a uniform cylindrical stress wave into the rock specimen.

A similar technique to study dynamic tensile fracture in rock by an electrohydraulic effect was used in Reference 17. In this work a wire was exploded underwater creating an electrical breakdown between two electrodes to generate an electrohydraulic disturbance that loaded the cavity wall of thin cylindrical disks. Although the experiments provided a great deal of qualitative data on radial tensile fracture, the interpretation of the data is quite difficult because the resulting deformation and subsequent fracture cannot be viewed in a one-dimensional manner. The lateral release waves give rise to a complex state of stress and strain and undoubtedly had some influence on the resulting fracture. The experiments carried out in the present program demonstrate that this influence is quite significant where for the same initial loading configuration and cavity size, but for varying cavity lengths, a marked decrease in the extent of tensile fracture damage is observed as the cavity length is decreased.

The success of using the exploding wire technique to study the dynamic tensile failure of rock in a tractable manner is dependent on several factors: the unidimensionality of the generated loading pulse, the ability to vary the loading pulse so that only tensile failure caused by the divergent nature of the wave occurs and not compressive failure caused by crushing, and the ability to measure the pressure loading time history on the cavity boundary.

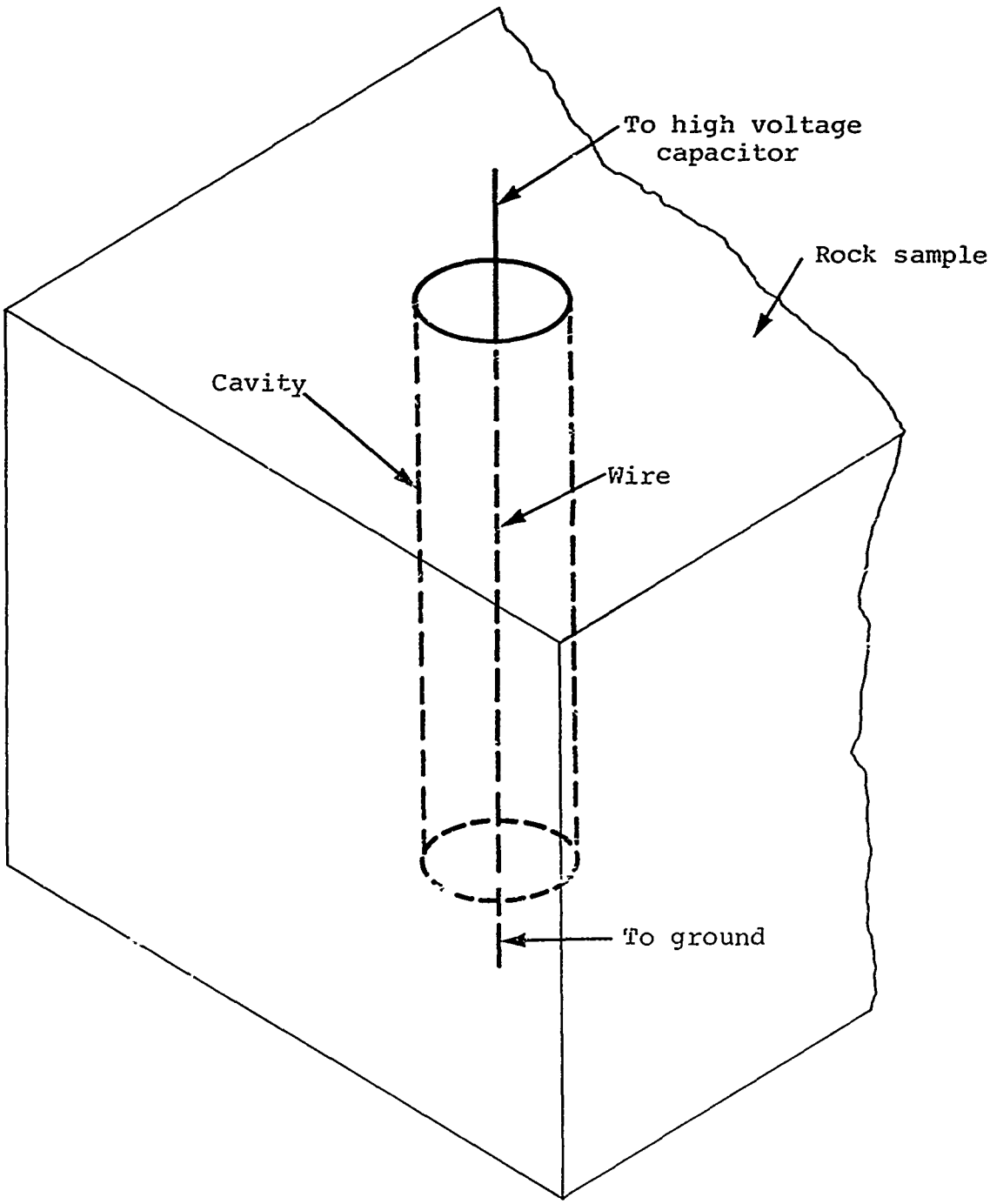

Figure 22 Exploding wire as a cylindrical cavity loading source.

The very nature of an exploding wire is indicative that radial symmetry can be expected. The uniformity of the vaporization along the length of the wire and the subsequent disturbance imparted to the sample cavity has been effectively demonstrated (References 21, 22, and 23). For this configuration then, the motion is unidimensional, in the radial direction only, making the observed effects easier to interpret and facilitating calculation of these effects.

Pressure pulses of various shapes and amplitudes can be obtained from the exploding wire apparatus. This is accomplished by changing the type or size of wire, varying the amount of energy to be discharged through the wire by using cylindrical cavities with different inner radii, or altering the confinement of the wire itself or by a combination of these methods. Some of the different types of loading pulses that can be used to examine fracture mechanisms are a) blast-wave loading where air serves as the transmitting medium, b) dynamic hydraulic loading where a fluid such as water or oil is the medium surrounding the wire, and c) impact loading where a liner surrounding the wire and initially separated from the cavity wall is accelerated and driven against the wall. Detonable gaseous mixtures and explosives can be initiated by the exploding wire. Surrounding them with various energy absorbing buffer materials can also provide a wide variety of pulse shapes.

With these possible variations in loading configurations, several aspects of fracture and comminution can be investigated. Compressive crushing along with the tensile failure can be obtained, or just tensile fracture can be obtained separately. For the immediate objective of examining tensile fracture, blast wave loading and hydraulic loading were deemed the most suitable.

The blast-wave loading pulse was generated by exploding a bare wire in air at atmospheric pressure. This disturbance produces a pulse with a very fast risetime followed by an exponential decay lasting for a few microseconds. The peak pressure and decay behavior is strongly dependent on the cavity size. The diverging geometry dictates that the smaller cavity will experience higher pressures and faster decay than a larger cavity for the same wire and discharge conditions. The hydraulic loading pulse was obtained by filling the cavity with water. This confinement offers considerably more restraint to the expansion of the wire than air does. Because of this, a much faster rate of energy deposition through the wire is required to generate a shock in the water than would be necessary to create a shock in air.

Measurements of the cavity pressure time-history in the adverse environment created by the current discharge through the wire is quite difficult for small cavities. For the present work, pressure-time loading histories for samples with 1-inch-diameter cavities were obtained with manganin gauges placed on the cavity. Piezoelectric probes were also used which provided a qualitative measurement of the pulse shape that collaborated the quantitative pulse obtained with the manganin gauges.

5.2 EXPLODING WIRE SYSTEM DESIGN

In the past decade, the exploding wire phenomenon has been extensively studied and widely used in several diverse applications. An excellent account of much of the research during this period is given in Volumes 1 through 4 of Exploding Wires (Reference 25). One application is not concerned so much with the physical behavior of the wire as it explodes but, rather, makes

use of the rapid release of energy imparted to the surrounding medium: to use the exploding wire as a cylindrical stress-wave generator to study low-stress-level dynamic tensile fracture.

The apparatus is designed to release a fairly large amount of energy in as short a period as possible. This is accomplished by storing energy in low-inductance capacitors, using a suitable switching mechanism to release the energy, and utilizing a low-inductance, parallel-plate transmission line to transmit this energy through the wire.

5.2.1 Capacitor and Transmission-Line Arrangement. The physical system is shown in Figure 23 and the electrical schematic of the discharge and safety interlock system is shown in Figure 24. The system is designed to accommodate up to ten 14.6 μF Sangamo high-energy discharge capacitors arranged in rectangular geometry and connected electrically in parallel. The capacitors are designed to operate at 20 kV which provides an energy storage capability of 29,200 joules. The inductance of each capacitor is 40 nH, giving a total inductance of 4 nH for the 10 parallel connected capacitors. To obtain as fast a discharge as possible, two parallel aluminum plates are used for the transmission line system to minimize inductance. The plates are 3/8 inch thick and 12 inches wide between the capacitors and the test section. The plates are insulated from each other by four to six layers of 10-mil Mylar sheet. The capacitors are mounted on a cart to provide flexibility, while the transmission plates are rigidly attached to the table. This will prevent gross movement of the system caused by the large magnetic pressures generated as the bank is discharged. The ground plate is connected directly to the bottom part of the test section, while the top plate is separated by 1 foot from the capacitor bank for switching purposes.

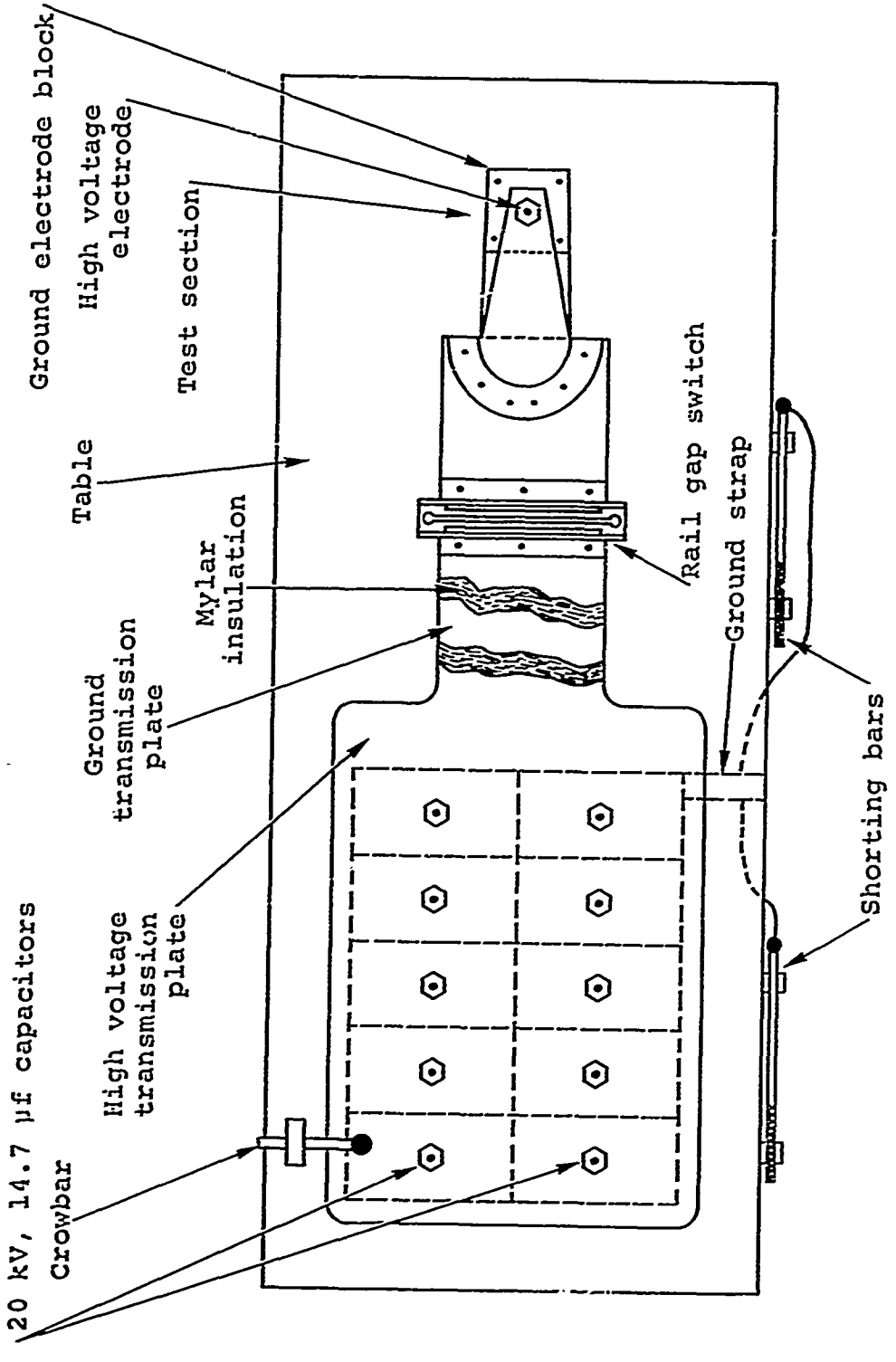

Figure 23 Plan view schematic configuration of exploding wire system.

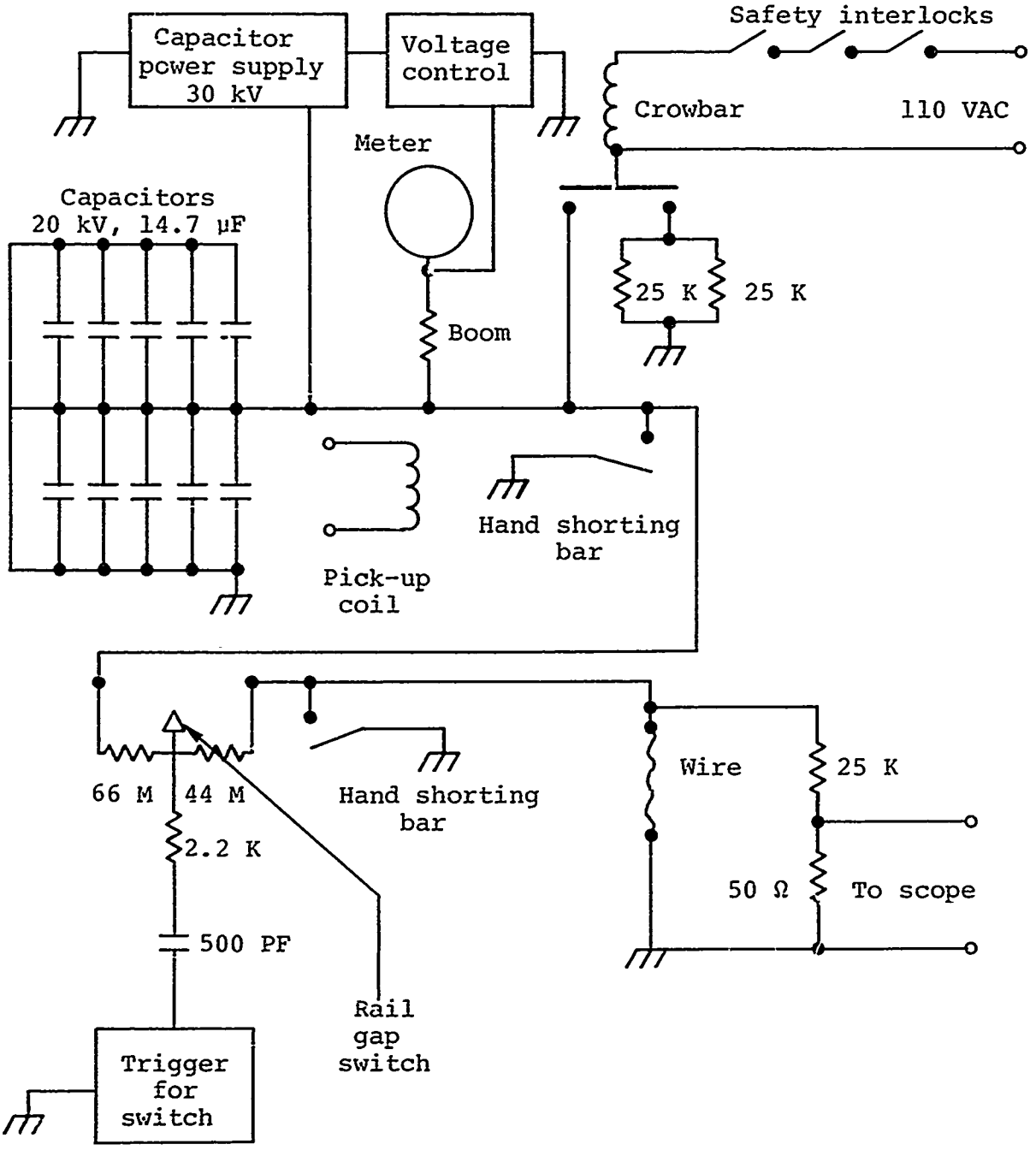

Figure 24 Electrical schematic of exploding wire system.

5.2.2 Test Section. The test section is designed to allow sufficient time for the middle portion of a test specimen to experience true one-dimensional deformation and fracture before end effects invalidate this assumption. The duration of one-dimensional motion is the difference in time between the arrival of the incident radial wave and an unloading wave from either end of the specimen. This period depends directly on the type of material under investigation and the length-to-thickness ratio of the specimen. The test section consists of a rectangular loop initially rising from the end of the transmission line with dimensions of approximately 12 by 13 inches. If necessary, the size of this loop can easily be changed by replacing the transmission line riser and the top plate of the test section with ones of different dimensions. The wire is fastened between two brass electrodes, the top one mounted on an adjustable brass bar which controls the length of wire. This allows wires of lengths up to 11 inches to be used. The present configuration can accommodate specimens as large as 24 inches in diameter by 11 inches in length.

5.3 SYSTEM DIAGNOSTICS

Current and voltage probes are used to monitor and evaluate the discharge characteristics of the exploding wire system. The current in the circuit is measured by a small pickup coil placed between the plates in the transmission line. The voltage induced in the coil by the time-varying magnetic field in the transmission line is

$$V = -N\frac{d\Phi}{dt} = -N\frac{d}{dt}(BA)$$

where N is the number of turns of wire, Φ is the magnetic flux, B is the magnetic field, A is the constant area of the coils. The field in a parallel plate transmission line is given by

$$B = \mu_o \frac{I}{w}$$

where w is the width of the transmission line and I is the current. Combining these expressions, relation between the voltage induced in the coil and the rate of change of current in the circuit is

$$V = \frac{N\mu_o A}{w} \frac{dI}{dt}$$

The output of the coil dI/dt may be integrated electronically to provide a current waveform. A schematic diagram of the current probe circuitry is shown in Figure 25.

A voltage divider is used to measure the voltage waveform across the wire. A schematic diagram of voltage probe circuit is shown in Figure 26. The voltage measured across the wire by a divider is a combination of resistive and inductive drops

$$V_T = V_R + V_I = I(t)R_w(t) + L_I \frac{dI(t)}{dt}$$

where R_w is the resistance of the wire sample and L_I is the sum of $L_w(t)$, the inductance of the wire, and L_p, the inductance associated with the divider's components and the pickup lead from the wire to the divider. With proper shielding and orientation of the pickup lead, the induced voltage caused by L_p is usually very small and can be neglected.

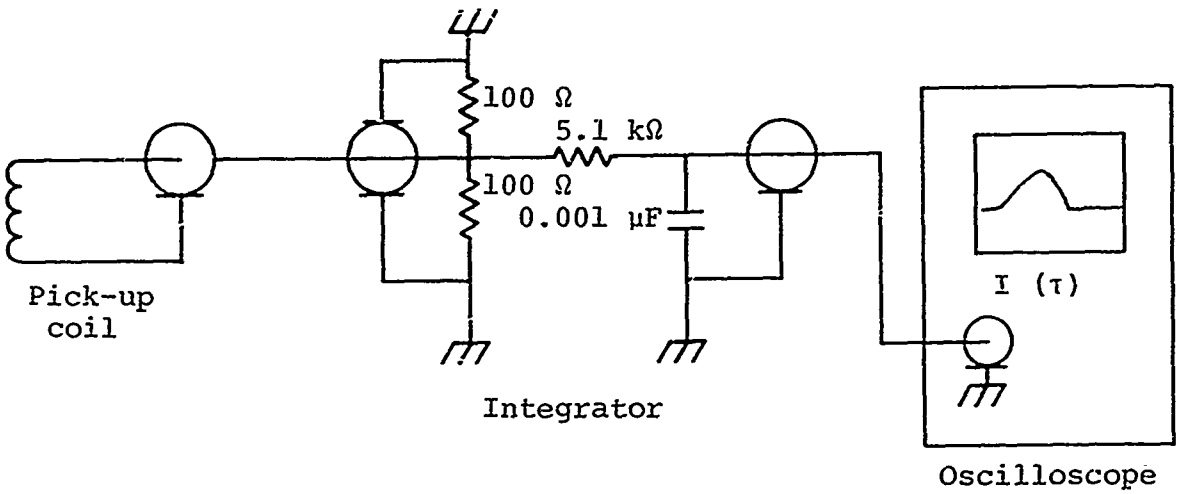

Figure 25 Schematic diagram of current probe circuitry.

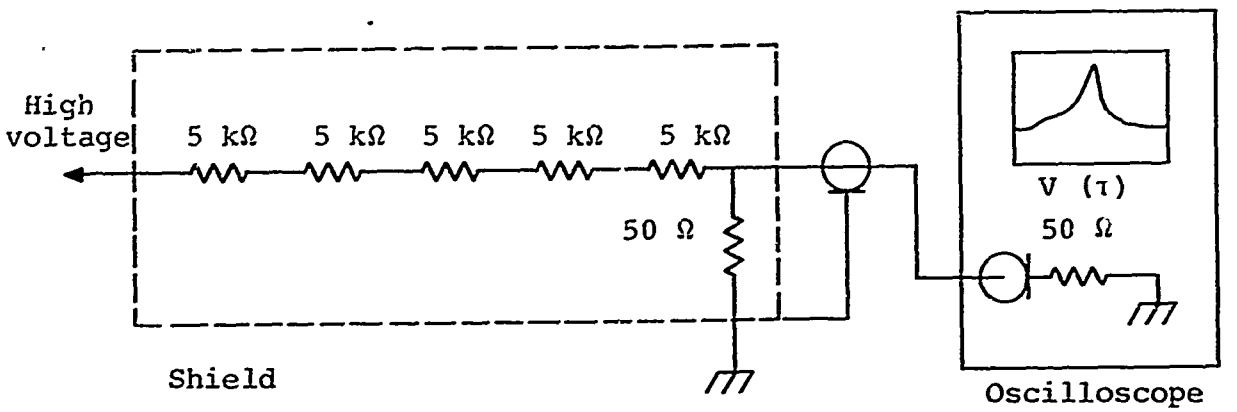

Figure 26 Schematic diagram of resistance voltage divider.

The proper use of current and voltage probes can provide a considerable amount of information concerning the electrical behavior of the wire as it explodes. Measurements of these two parameters are made to check the discharge characteristics associated with the wire and to correlate discharge conditions to peak pressures and pulse shapes. An example of the foregoing diagnostics recording discharge characteristics are shown in the oscilloscope traces in Figure 27. Figure 27 shows the damped ringing behavior of the system through a direct short using six capacitors charged to 20 kV. The period of 43 μsec and the total inductance of the system is 0.531 μH. The voltage and current waveforms for a 51-mil diameter phosphor-bronze wire, 11 inches long, is shown in Figure 27 for the same discharge conditions.

5.4 FRACTURE EXPERIMENTS

The experiments were carried out in three separate steps. Initial tests were made with various types and sizes of wires to determine suitable wire-discharge combinations for the fracture tests. Next, fracture tests on samples of Westerly granite were conducted using various wire-discharge combinations. The third step, the most difficult, was directed toward measuring the cavity boundary condition.

5.4.1 Wire Characterization. Several wire-discharge combinations were tried. These tests consisted mainly of exploding a wire in atmospheric air and monitoring the current and voltage waveforms. A typical current and voltage waveform for a 51-mil-diameter phosphor-bronze wire, 11 inches long, was shown in Figure 27b. The sudden spike in the voltage trace is mostly due to the inductive pickup by the voltage probe caused by the collapsing electrical field. This inductive peak decreased when the

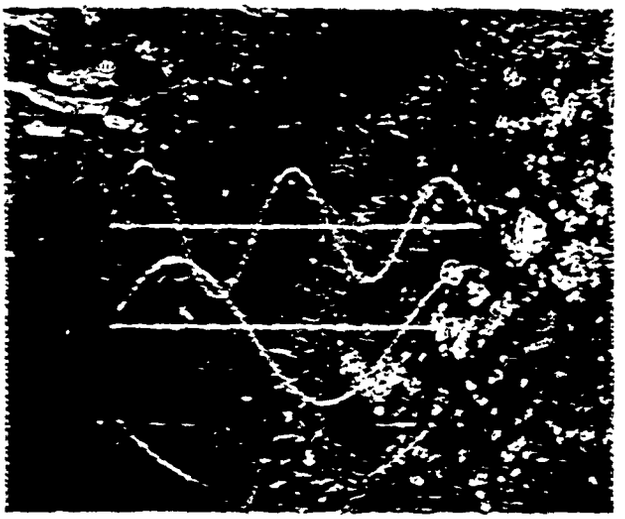

a. 141,600 amps/cm
10 μsec/cm

b. 141,600 amps/cm
5 μsec/cm

a. Discharge current through shorting bar.

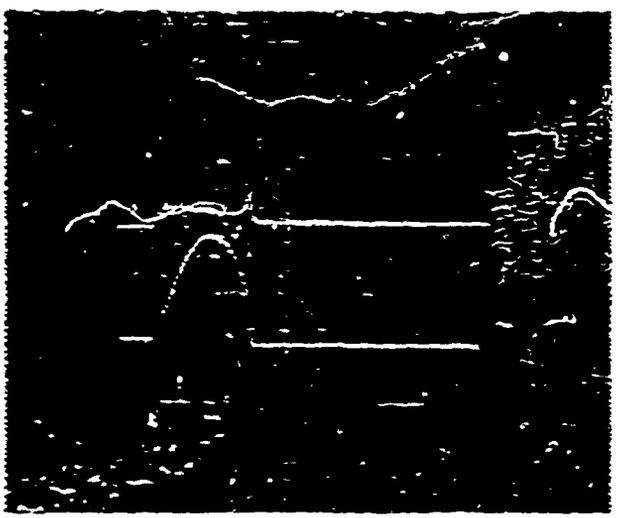

a. Voltage 20,000 volts/cm
5 μsec/cm

b. Current 60,800 amps/cm
5 μsec/cm

b. Discharge through 0.051 inch diameter by 11 inches long phosphor bronze wire in atmospheric air.

Figure 27 Typical current and voltage wave forms, V_o = 20 kV.

A758

wire was exploded in water and the time of discharge increased slightly. Also, the peak decrease as the length of the water column surrounding the wire increased.

It is possible to use only mechanical methods to obtain different pulse amplitudes and shapes, maintaining a single wire/discharge combination that results in the system being well matched. This corresponds to the total stored energy being consumed in a single discharge pulse. The maximum impulse imparted to the surrounding media is normally associated with the wire being well matched to the discharge system. Because a large portion of the stored energy is dissipated by joule heating to vaporize the material, the remaining energy is distributed to the surrounding media by radiation, ionization, and the rapid expansion of the vaporized products. For a given wire and a certain combination of system parameters, i.e., capacitance, charging voltage, and inductance, some of the charge energy can either be left in the capacitor or, sometime after the initial discharge, dissipated when a restrike occurs. With a restrike, a second wave usually results whose characteristics are difficult to ascertain. Care was taken to avoid using wires exhibiting restrike for the fracture experiments.

After a considerable amount of trial and error, testing a variety of wire materials and sizes, the wire/discharge combinations chosen as a line source for the fracture experiments were a 51-mil-diameter, 11-inch-long phosphorus-bronze wire exploded at 20 kV and 32-mil-diameter, 11-inch-long phosphorous-bronze wire exploded at 20 and 15 kV. Figure 28 shows some data of discharge time versus charging voltage for exploding wires in atmospheric air and in distilled water for a storage capacitance of 88 μF. As previously indicated, the water containment slightly decreases the rate of discharge.

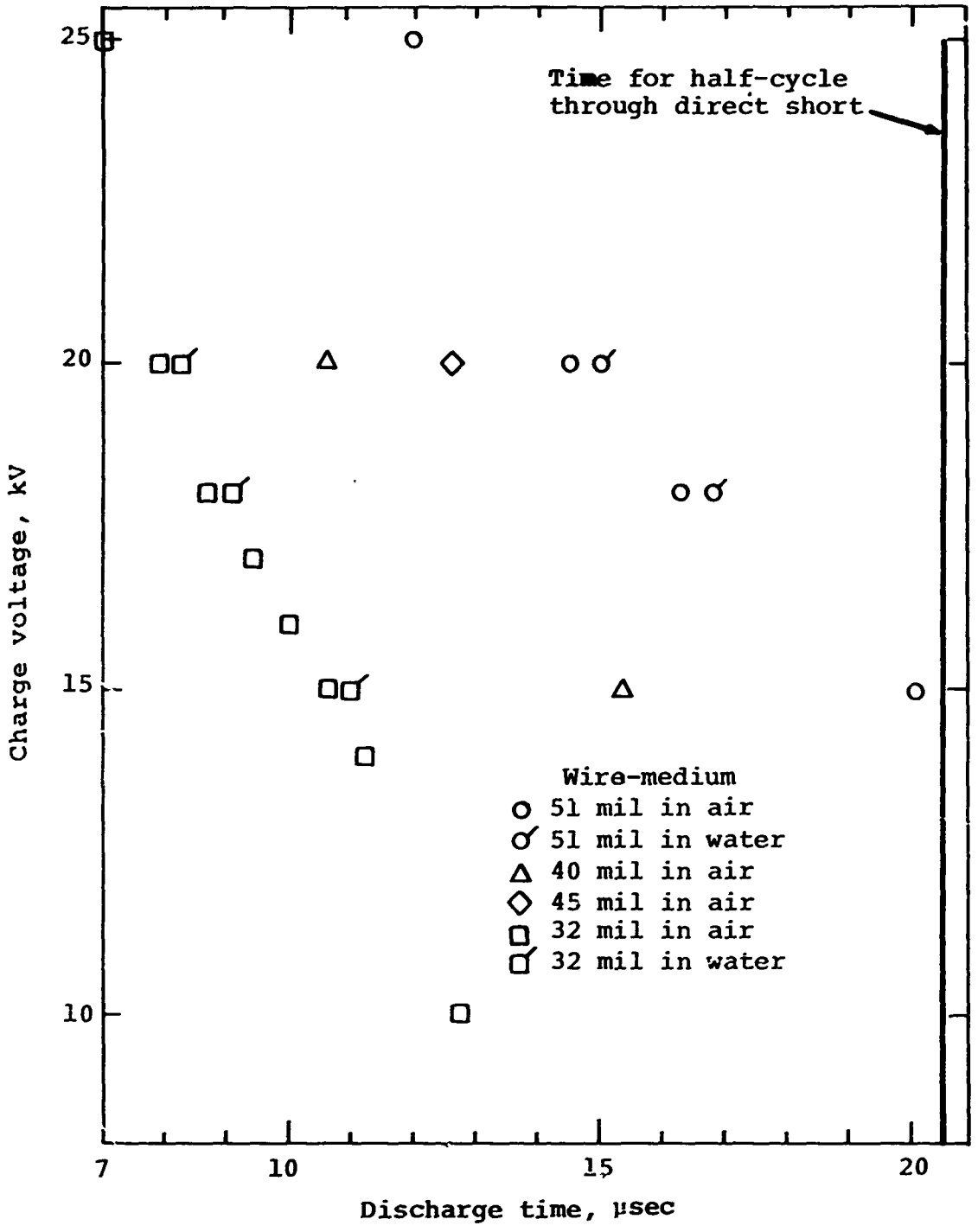

Figure 28 Discharge voltage versus time of discharge for 11-inch long phosphor bronze wires.

5.4.2 Fracture Tests in Westerly Granite. The rock material used in the fracture tests was Westerly granite which is a very fine-grained and homogeneous type of granite. Two main reasons for using this granite were its homogeneity and the existence of a considerable amount of material response data to characterize its static and dynamic behavior.

The configuration used for the fracture experiments is shown in Figure 29. The test samples were nominally 7-inch cubic blocks, although several tests were made with shorter samples. The cylindrical cavity sizes were either nominal ½- or 1-inch diameter and were made with diamond core drills. Concentric end caps were placed at ends of the sample with a hole drilled through the center of each end cap to accommodate the wire. These served the purpose of positioning the wire along the axis of the cavity and of acting as a seal for retaining water in the cavity. 2024-T4 aluminum plates were used as momentum-wave traps to eliminate the effects of the reflected wave from the free surface. The mechanical impedance of the aluminum plates is nearly the same as that of granite, thus providing an excellent means of absorbing the incident compressive pulse.

A summary of the fracture experiments conducted on Westerly granite is shown in Table 2. After a sample was subjected to the blast wave or hydraulic-type loading, it was sectioned in half to examine its midplane portion for fracture damage. The sectioned surfaces were treated with a penetrating fluorescent dye to bring out the very fine cracks. Samples with a 1-inch cavity diameter subjected to the blast wave loading (i.e., shots 001 and 002) exhibited no evidence of fracture damage even after the sectioned surface was treated with the penetrant and inspected with a microscope. A sample with a ½-inch-diameter cavity (i.e., shot 004)

TABLE 2

EXPLODING WIRE FRACTURE EXPERIMENTS
ON WESTERLY GRANITE

Shot No.	Cavity Dia. x Length (inches)	Lateral Dim. (inches)	Cavity Medium	Wire Type-Size	Charge Voltage (kV)	Charge Energy (joules)	Peak Pressure (kbar)	Remarks
001	1.020 x 7	6 x 7	Air, 1 atm.	Phosphor bronze 0.032 in. dia x 10-7/8 in. long	20	17,600	?	No fracture
002	0.510 x 4	6 x 6	Air, 1 atm.	Phosphor bronze 0.032 in. dia x 10-7/8 in. long	20	17,600	?	No fracture
003	1.020 x 6	6 x 7	Air, 1 atm.	Phosphor bronze 0.051 in. dia x 10-7/8 in. long	20	17,600	1.78	No fracture
004	0.510 x 7	6 x 6	Air, 1 atm.	Phosphor bronze 0.051 in. dia x 10-7/8 in. long	20	17,600	2.5	1-2 cm cracks; 10 μsec momentum plates
005	1.020 x 2	6 x 7	Water	Phosphor bronze 0.051 in. dia x 10-7/8 in. long	20	17,600	?	1-2 cm cracks; no momentum plates
006	0.510 x 3	6 x 6	Water	Phosphor bronze 0.051 in. dia x 10-7/8 in. long	20	17,600	?	No momentum plates; four complete breaks; several small fractures
007	1.020 x 6	6-3/4x6-3/4	Water	Phosphor bronze 0.051 in. dia x 10-7/8 in. long	20	17,600	1.6	No momentum plates; five major breaks; extensive fracture between breaks
008	1.020 x 6	6-3/4x6-3/4	Water	Phosphor bronze 0.051 in. dia x 10-7/8 in. long	20	17,600	1.6	10 μsec momentum plates; four major breaks; damage less than 007
009	1.020x2-3/4	6-3/8x6-7/8	Water	Phosphor bronze 0.032 in. dia x 10-7/8 in. long	15	9,900	?	10 μsec momentum; 1-6.5 cm cracks; sample remained intact
010	1.020 x 6	6-1/2x6-1/2	Water	Phosphor bronze 0.032 in. dia x 10-7/8 in. long	15	9,900	1.36	10 μsec momentum plates; 2-7 cm cracks; sample remained intact; more damage than for 009
011	1.020x2-3/4	6-1/2x6-1/2	Water	Phosphor bronze 0.032 in. dia x 10-7/8 in. long	15	9,900	?	No momentum plates

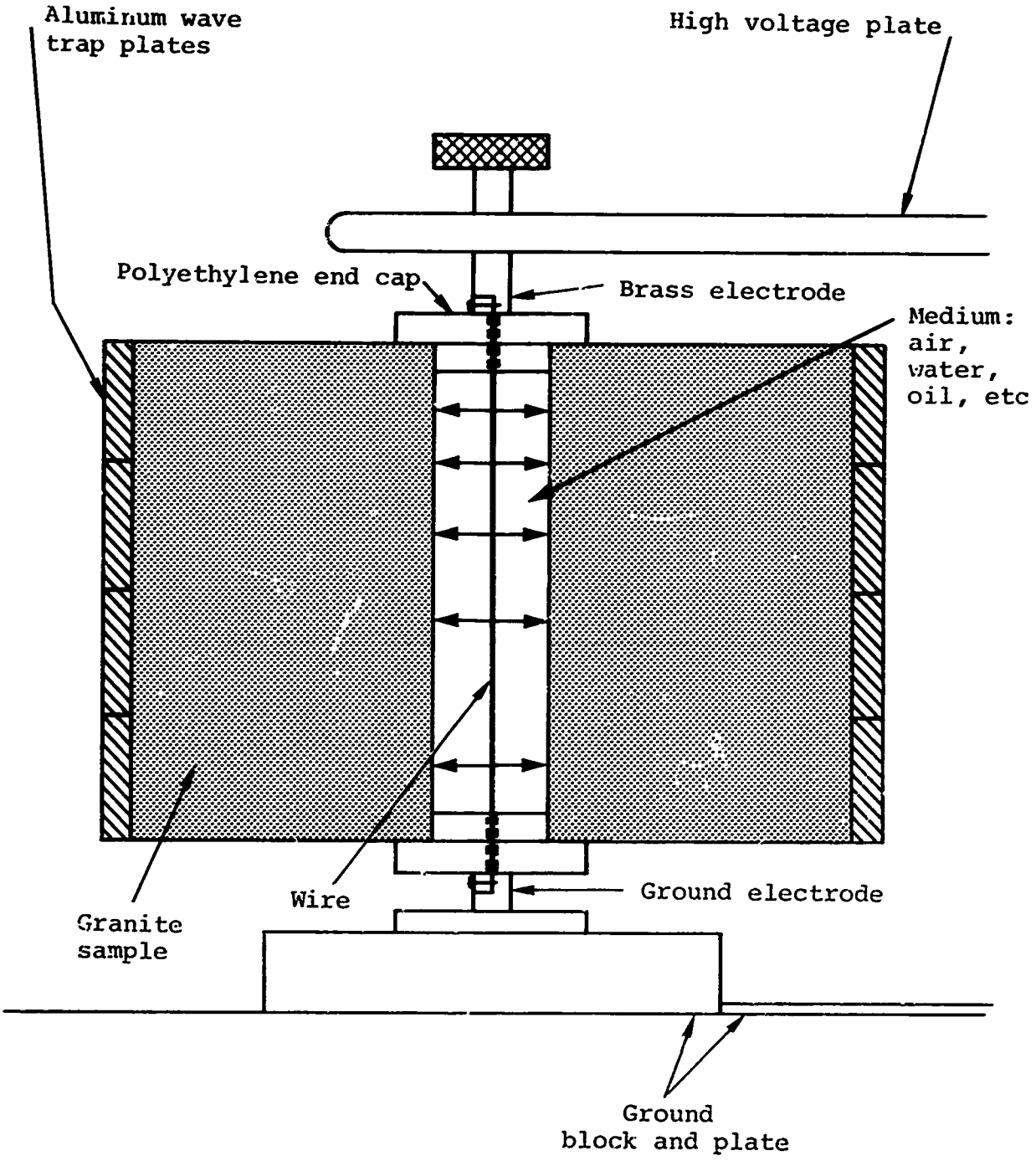

Figure 29 Cross section configuration of tensile fracture experiment.

tested with the wire-discharge combination of a 51-mil-diameter phosphorus-bronze wire exploded at 20 kV showed several cracks between 1 to 3 cm in length. A picture of the midplane section for shot 004 is shown in Figure 30.

In shots 005 through 01, water was used in the cavity instead of air. Extensive fracture damage was obtained with the 51-mil-diameter phosphor-bronze wire at 20 kV. A comparison of the fracture damage in shot 008 with momentum plates (Figure 31a) and shot 007 without them (Figure 31b) shows the effect of the free surfaces. The difference is not very pronounced because the incident pulse length was longer than 10 μsec, which was the length of pulse the momentum plates could trap. Measurements of this pulse indicated its total duration was 20 μsec and parabolic in shape having a peak of 1.6 kbar. The same wire-discharge combination applied to a sample having a shorter cavity length (2 inches) shot 005, showed significantly less damage (Figure 31c) than that for the cavity lengths of 6.5 inches (Figure 31a and b). This demonstrates that the hydraulic loading pulse is greatly altered by the influence of the top and bottom surfaces of the shorter sample which undoubtedly attenuates the peak and shortens its duration. For the short cavity length, the response of the midplane is not truly one-dimensional, in the sense of cylindrical plane strain, beyond 4 μsec, but is more like the response associated with the work of (Reference 17) of cylindrical plane stress. These experimental results are consistent with elastic theory which predicts that the maximum hoop tension for cylindrical plane stress is less than that for cylindrical plane strain for the same loading. Thus, for the shorter length samples the loading pulse can be altered significantly. This, along with the change in the state of stress from plane strain to a more complex state approaching plane stress, results in a pronounced decrease in the damage imparted to the rock.

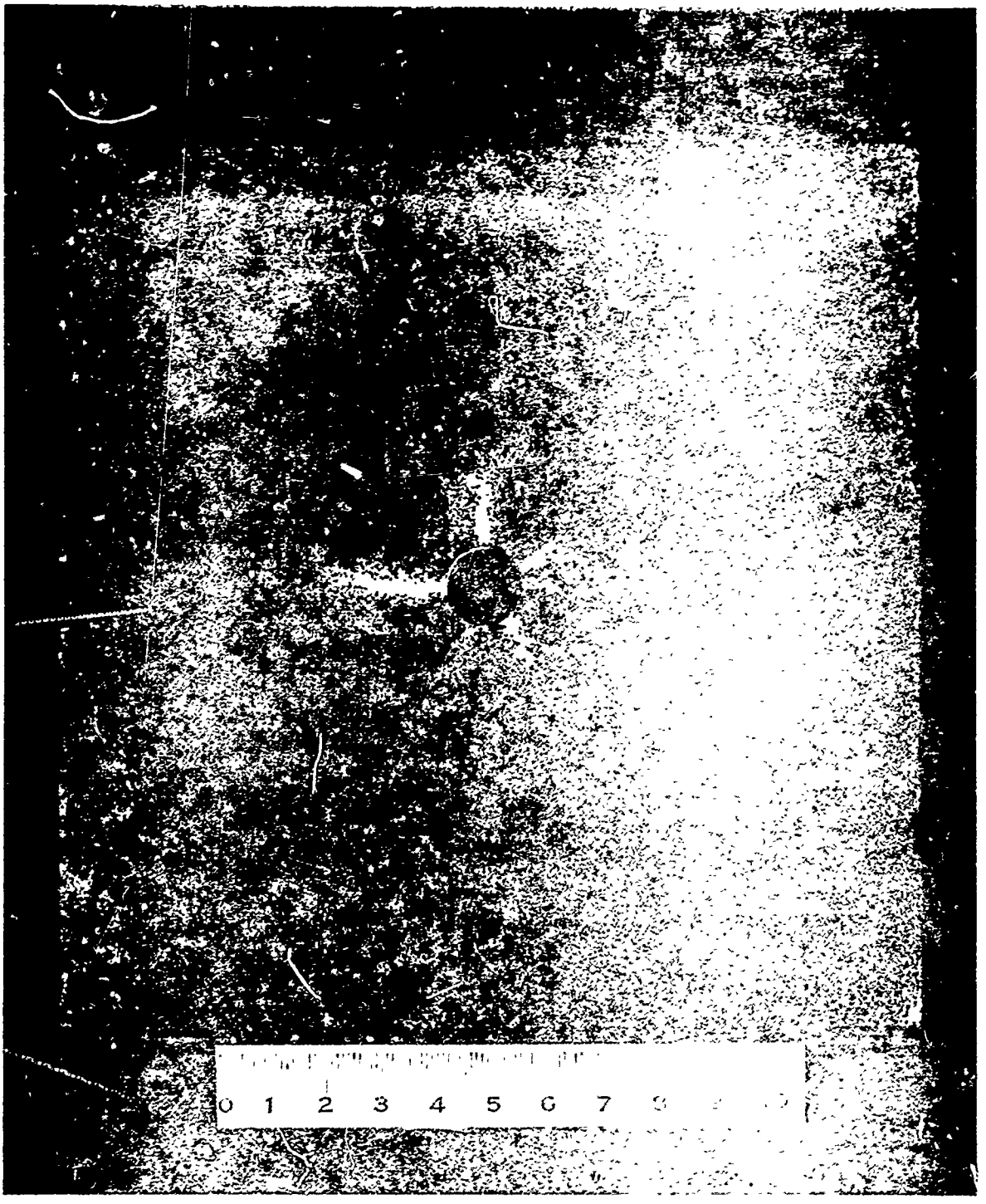

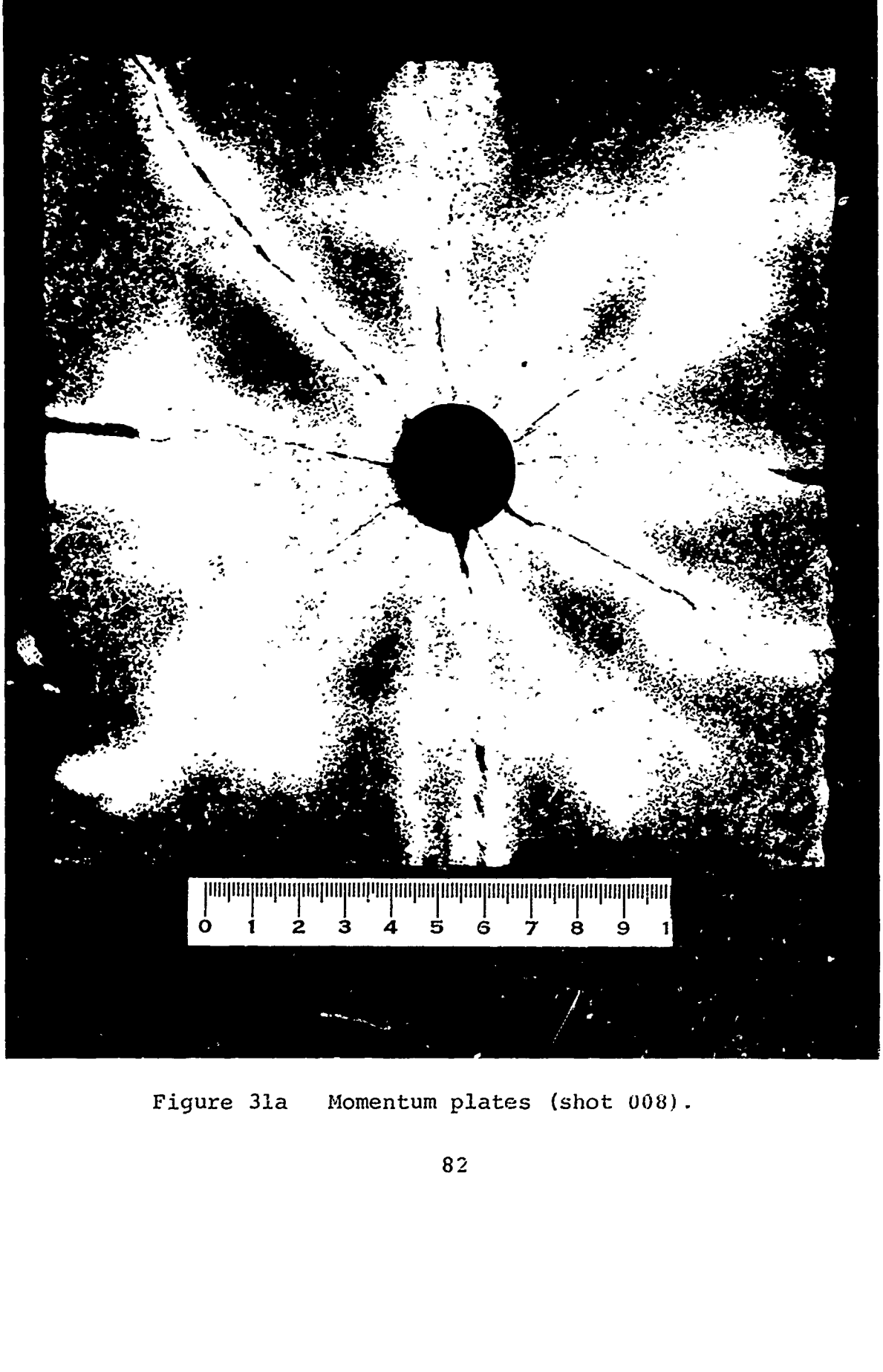

Figure 31a Momentum plates (shot 008).

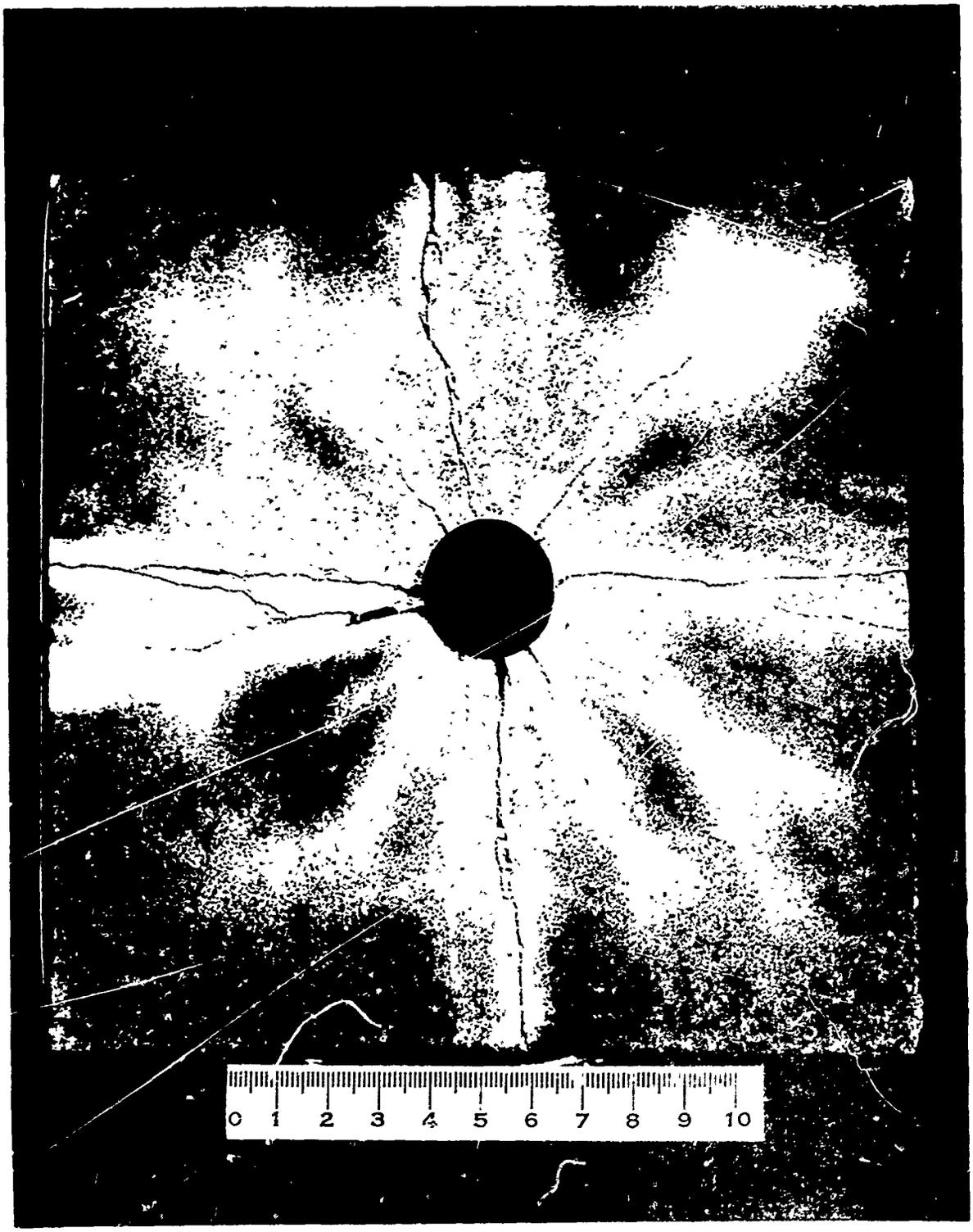

Figure 31b No momentum plates, shot 047.

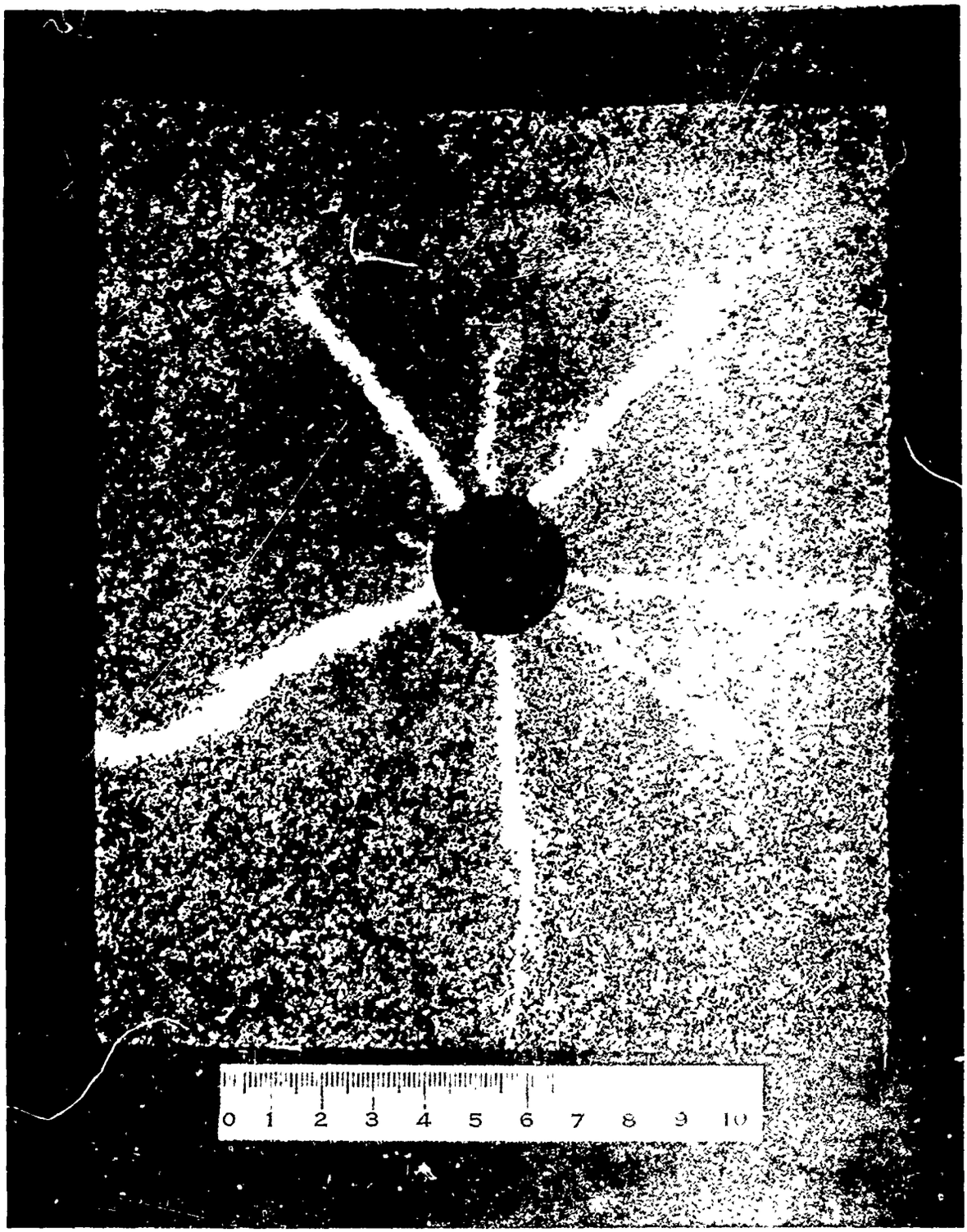

Figure 54. Short Cavity, Low Mach

In shots 009, 010, and 011, a 32-mil-diameter phosphor-bronze wire exploded at 15 kV in water was used. This provided about 56 percent of the energy of that used in the previous shots and resulted in considerably less damage imparted to the sample. The loading pulse was about 15 μsec duration with a peak of 1.36 kbar. Pictures of the fracture damage for short (2.5-inch cavity length) samples with and without momentum plates are shown in Figures 32a and b, respectively. The sample in shot 009 still experienced cracks that intersected with the outer surfaces, but it remained intact. Figure 32c shows the damage for shot 010, a sample with a 6-inch cavity length. The damage patterns in shots 009 and 011 were affected by a hairline fault running from the upper left corner of the sample down toward the cavity and from the cavity toward the bottom right side. Here again the damage is considerably less than for shot 010 in which the sample had a longer cavity length.

For the water loading tests, the influence of the free surface, even for shots with momentum plates, is quite apparent. There are four major cracks that intersect perpendicularly the samples' outer surfaces. This is most probably caused, as exhibited in shot 009 (see Figure 32a), by that portion of the reflected wave not trapped in the aluminum plates. For this case, the cracks not perpendicular to the sample boundaries extend out to radii less than the perpendicular radius to the surface. This, however, is not the case for shots 007 and 008, which indicate that cracking would have extended to the sample surfaces even if the entire pulse was trapped in the momentum plates.

The reason that the momentum plates were not sufficient to entrap the incident pulse was that the long pulse durations were

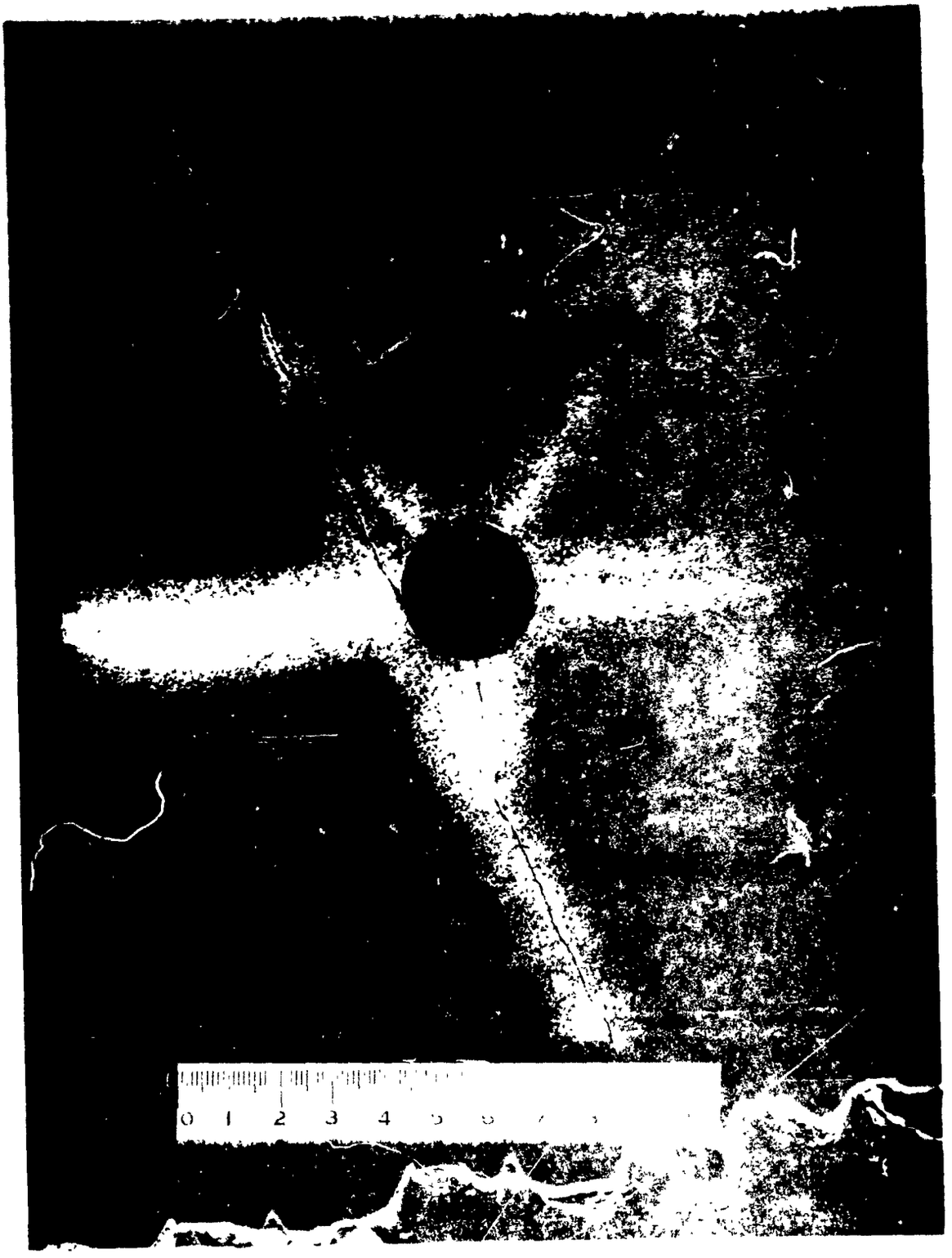

Figure 3.3 Observed [illegible]

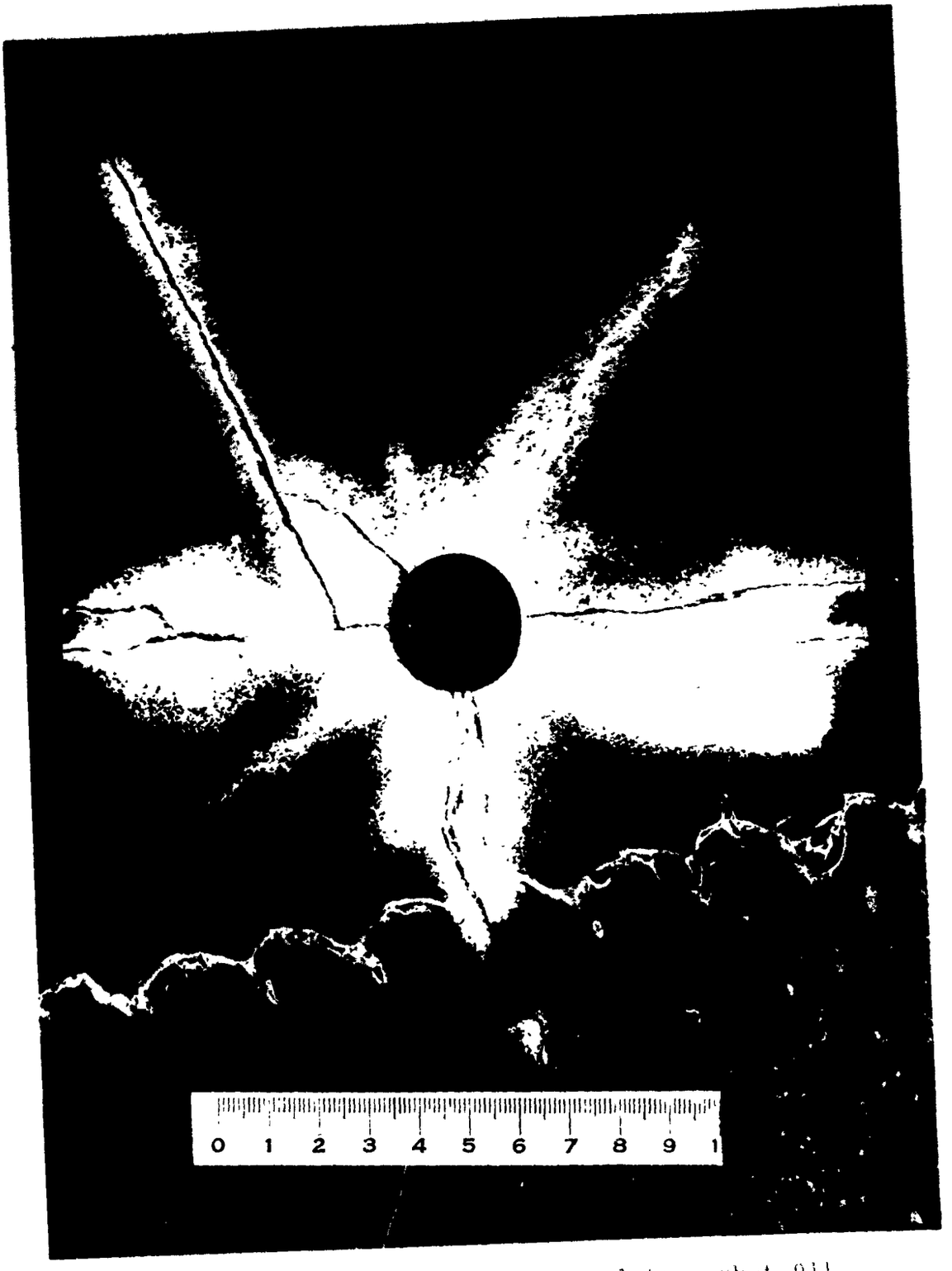

Figure 32b Short cavity, no momentum plates, shot 011.

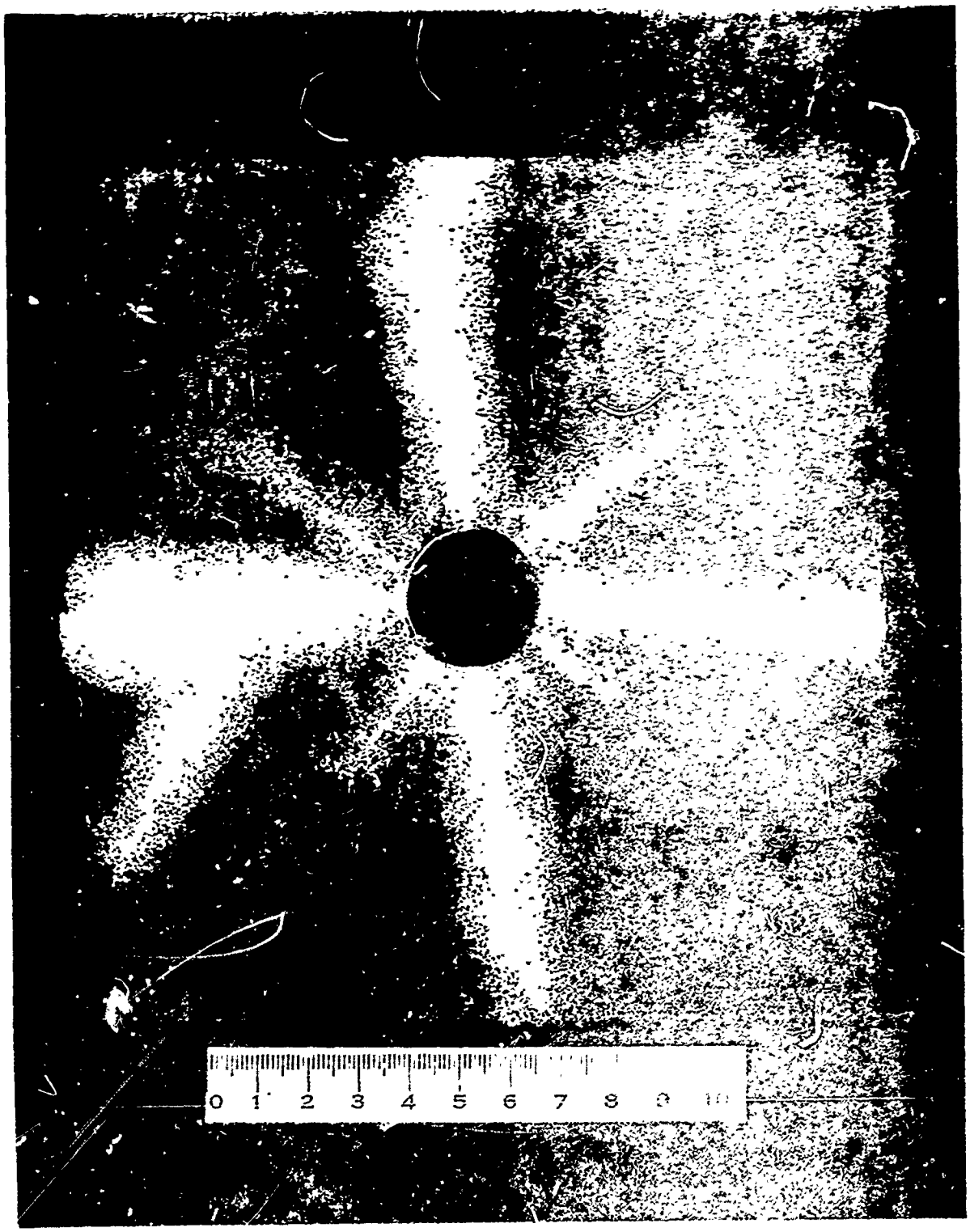

Figure 32: Momentum plates, shot

not anticipated. A successful measurement of the loading pulses was not obtained until after the fracture tests were completed. The difficulty encountered in obtaining a reliable measurement of the loading pulse is discussed below. The use of samples with larger lateral dimensions would have helped to alleviate the effects of the free surfaces, but none were available.

5.4.3 Measurements of Cavity Loading Conditions. As previously noted, the adverse environment created by the exploding wire makes the measurement of the cavity pressure-time history very difficult, especially for small cavities. A review of techniques that have yielded varying degrees of success appears in Reference 26. The methods that proved most successful were those from which the pressure-time history had to be deduced indirectly from measurements of the shock wave speed or the elastic free-surface response of a cylindrical sample. These indirect techniques are quite tedious to apply and very time-consuming. Also, they are not well suited for the problem in this work. For these reasons, a more direct method for measuring the cavity condition using piezoresistive gauges was pursued.

The use of manganin piezoresistive gauges for shock wave measurements has been extensively studied and well documented (References 27, 28, and 29). The manganin gauge exhibits a fractional change in resistance that is proportional to the normal stress component, σ, acting on its active element. This is expressed by

$$\sigma = \frac{1}{K} \frac{\Delta R}{R_g}$$

where R_g is the initial value of the resistance of the gauge and $K = 0.0027\ \Omega/\Omega/\text{kbar}$ for the gauges employed here.

A 50-ohm photo-etched manganin foil gauge* was bonded to the cavity of an aluminum block (Figure 33a). The gauge is bonded to the cavity with a thin layer of Furane Epocast 202 epoxy so that it blends in smoothly with the curvature of the cavity. The total thickness of the gauge package is 5 mils. The assembled gauge-aluminum block is shown in Figure 33b. Because of the excellent impedance match of aluminum with granite, the cavity pressure measured by the manganin gauge for both the airblast wave loading and hydraulic water loading is very close to that experienced by the granite samples.

The power supply used with the above gauge was a Piezo-resistive Gage Pulse Power Supply** which utilizes a Wheatstone bridge circuit shown in Figure 34. Briefly, the gauge forms one arm of the bridge. The bridge is initially balanced, V = 0, with the capacitor-pulse type power supply charged to a voltage, V_o. Several microseconds prior to the arrival of the stress wave at the gauge, the capacitor is discharged. When the gauge is compressed by the pressure loading, the bridge becomes unbalanced and the resultant voltage, V, across the null indicator is monitored on an oscilloscope. A circuit analysis gives the change in resistance, ΔR, of the gauge element as

$$\Delta R = \frac{\frac{V}{V_o}\left[(R + R_3)\left(\frac{R_3 + R_4}{R_3} + \frac{R_4}{R}\right) + R_1 + R_2\right]}{\frac{R_4}{R} - \frac{V}{V_o}\left[\frac{(R + R_3)(R_3 + R_4)}{R R_3} + \frac{R_1 + R_2}{R + R_3}\right]}$$

*Micro-Measurements Company, Romulus, Michigan, Manganin Gauge LM-SS-210AW-048.

**Metro Physics, Incorporated, Model 50-75C.

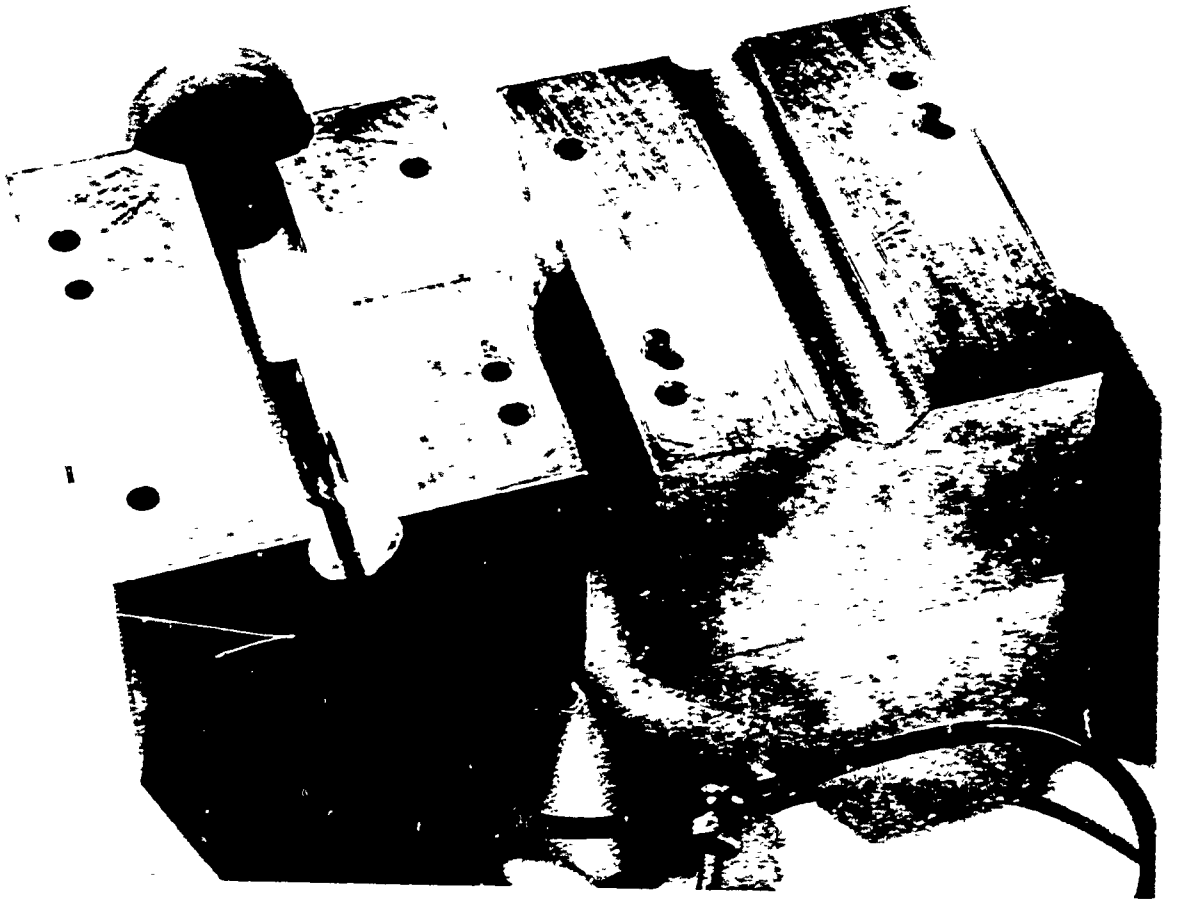

Figure 33a Gauge mount [illegible]

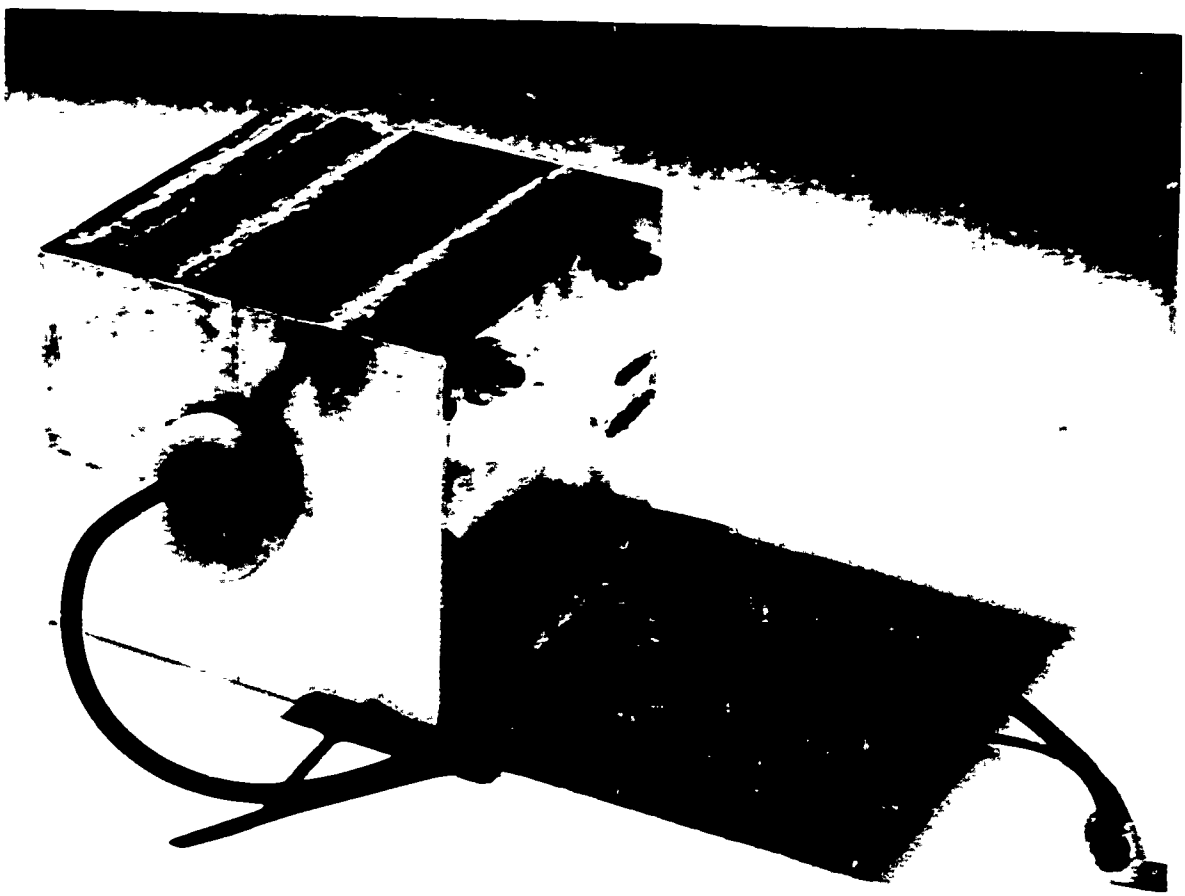

Figure 33b Assembled aluminum gauge block.

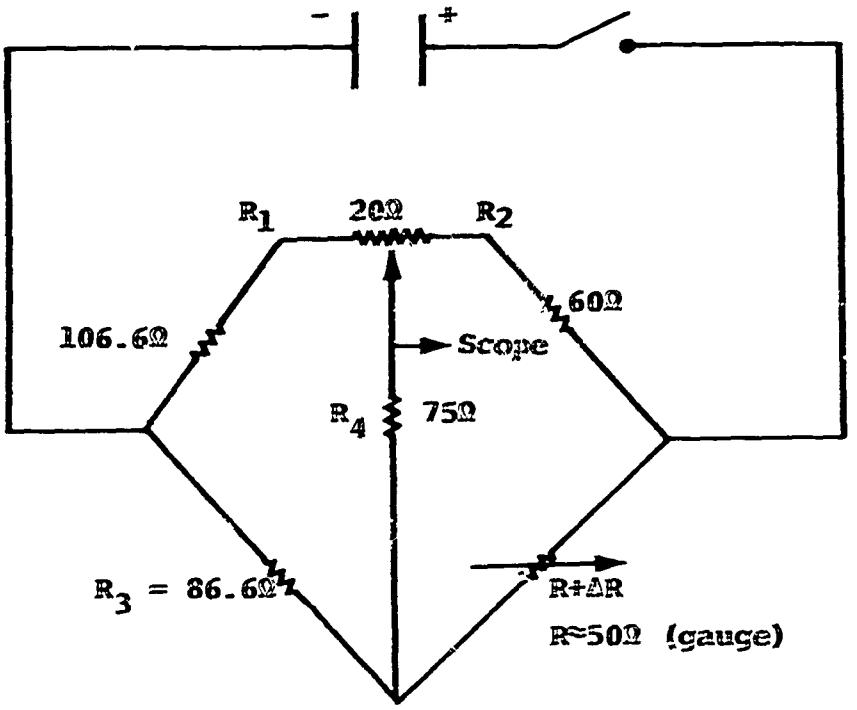

Figure 34 Bridge circuit for manganin gauge measurements.

where values of R_1, R_2, R_3, and R_4 are defined in Figure 13 and $R = R_g + R_x$ is the total resistance in the gauge arm, with R_x the cable resistance in the gauge arm. The use of this expression, together with the gauge constant K, provides $\sigma(t)$ for a known V_o and the measured V(t).

Three different pressure profiles were measured on a 1.020-inch-diameter cavity using the manganin-gauge aluminum-block configuration. A blast-type loading pulse in atmospheric air created by a 51-mil-diameter phosphor-bronze wire and exploded at a voltage of 20 dV, a hydraulic loading pulse in water created by the same wire and voltage conditions, and a hydraulic loading pulse in water created by a 32-mil diameter phosphor-bronze wire and exploded at 15 kV are all shown in Figure 35. Although the peak pressure of the blast wave pulse is higher than both the water pulses, its impulse is significantly less. Samples loaded with this pulse (e.g., fracture shot 003) showed no fracture damage.

The success of these measurements depended on the pressure-loading pulse arriving at the cavity after the onset of dwell when current had ceased to flow through the wire, (e.g., Figure 27b). The reason for this is that the manganin gauge acts as a search coil and picks up voltage, induced by the rapidly changing magnetic field, which is fed back into the bridge circuitry. The amplitude of this voltage increases the closer the gauge is to the exploding wire and exceeds the signal voltage from the gauge. Shielding the gauge from this field would be quite difficult and impractical, since it would physically interfere with the response of the gauge to the pressure pulse. However, the manganin-gauge power supply was capable of recovering from the effect of this induced signal about 2 μsec after current shutoff, and measurements of the pressure pulse could be obtained

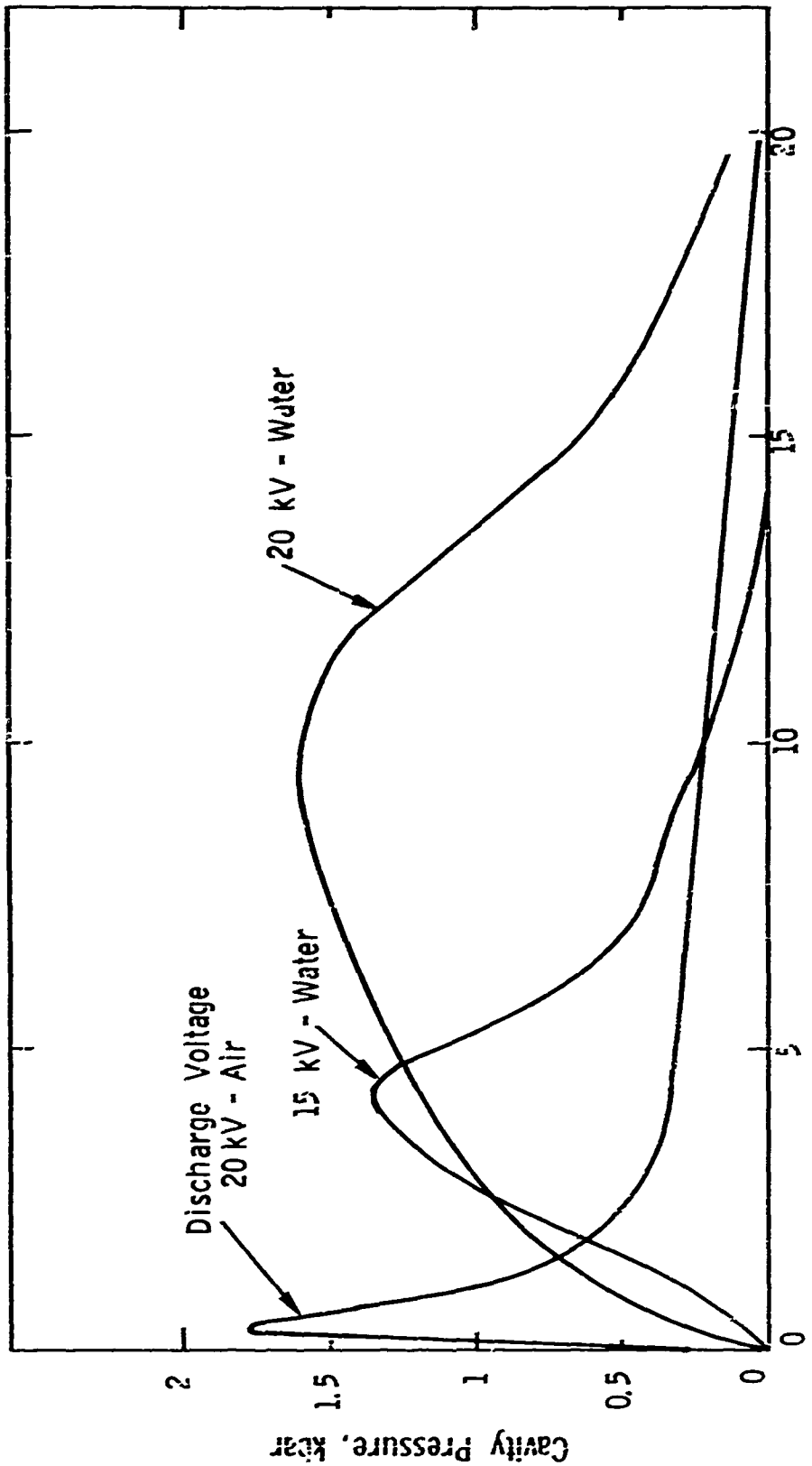

Figure 35 Cavity-pressure time history for exploding wire in air and water (cavity diameter = 1.020 inches).

after this time. The arrival of the pulse in air and water for a 1.020-inch-diameter cavity was about 3 and 4 μsec, respectively, after current shutoff. However, the arrival of the pressure pulses for the ½-inch-diameter cavity preceded the current dwell and measurements could not be obtained.

Another measurement of the pressure pulse was obtained with small (0.0937-inch diameter) barium titanite probes inserted in holes drilled in the radial direction of plexiglass samples. Although the response of these probes could not be quantitatively deduced, they did provide a qualitative measurement of the pressure pulse shapes which was similar to that obtained by the manganin gauges. This helped to substantiate the authenticity of the measurements made by the manganin gauges.

As mentioned previously, the gradual-rise, long-duration character of the pressure pulse created by the exploding wire in water (Figure 35) was not initially anticipated. However, these pulses are not so surprising when considering the analogy of a simple moving piston for the expansion process of the wire. Several different mechanisms have been proposed to explain the vaporization or expansion process of the wire (e.g., Muller, Bennet and Webb, and Chace in Reference 25). These mechanisms are quite complex and a discussion of them is beyond the scope of the present work. The following discussion is offered simply as a possible intuitive explanation for the different pressure profiles obtained.

The whole process of melting and vaporizing the wire occurs in only a few microseconds. Prior to the vaporization, the physical shape of the wire is maintained by inertia and magnetic pressure. As time proceeds, the magnetic pressure drops with the

collapse of the current and the kinetic pressure becomes dominant and expansion of the vaporized material begins. Now consider this expanding material to act as a cylindrical piston compressing the surrounding medium. For a given wire and rate of energy deposition, the environmental containment of wire strongly affects the rate of expansion. An air environment allows little restraint to the expansion of the wire in comparison with the restraint afforded by a water environment. The distance required for a shock to develop in front of a moving piston in a hydrodynamic medium is proportional to the square of the sound speed and inversely proportional to the acceleration of the piston. Therefore, since the cylindrical piston can expand more rapidly in air than in water, a shock wave will be formed in air in less distance than would be required in water. A steeper wave front in water would result sooner if the rate of energy deposition is increased. This would increase the kinetic pressure, and hence, the acceleration of the cylindrical piston. The steeper rise of the pressure pulse for the 32-mil wire at 15 kV in Figure 35 is an indication of this where the rate of energy per unit mass is about 1.9 times that for 51-mil wire at 20 kV.

5.5 INTERPRETATION OF EXPERIMENTAL RESULTS

Calculations were made of the experimental geometry and loading conditions using both the linear-elastic description of granite and the tensile fracture model described in Section 4.4. As a result of this analysis, a deeper understanding of the process of tensile fracture in this geometry can be obtained.

Experimental shots 002 and 004 were especially interesting, as they give the possibility of bracketing the tensile strength. The first calculation used a perfectly elastic model to compute

shot 002. The validity of the purely elastic assumption can be checked by noting the trajectory in $\sqrt{J_2'}$, J_1 space--Figure 36, trajectory 002--and comparing to compressional fracture data. Within the experimental scatter, the trajectory is inside the proportional limit data of Reference 15. The calculated maximum hoop tensile stress is shown in Figure 37 for shots 002 and 004.

For the rest of the discussion it is assumed that tensile failure is determined by just the peak tensile stress.*

From Figure 37, the tensile strength of granite is at least 0.6 kbar, since the 1-inch bore hole shot did not fracture. The ½-inch bore-hole shot did fracture, so that the tensile strength is no more than 1.5 kbar. When the calculation was repeated using the tensile crack model with a tensile strength of 1 kbar, the model indicated fractures out to nearly 0.8 cm radius, where the elastic calculation showed slightly more than 1 kbar peak tension. The water buffer calculation used an 0.8-kbar tensile limit, and the calculated extent of cracking was about 1.5 cm, where an elastic calculation showed about 0.8-kbar peak tension. The experiments, however, showed that those cracks which did not intersect (and so were not obviously influenced by) the free surface, extended to locations where elastic calculations show the peak tensile stress to be about 0.3 kbar for both the water buffer (Figure 38) and the ½-inch air buffer (Figure 37).

From these observations, it is concluded that it requires less tensile stress to propagate a crack than it does to initiate one. That the effect of opening a void takes some energy from the stress wave is concluded from the peak tensile stress being a few percent lower at a given range when the tensile crack model is used than an elastic calculation shows.

*It may be that this is not a sufficient criterion, but it is simple and convenient. Since the air pulses have similar tensile stress histories, the peak value or the integral of (say) stress time are equivalent criteria. Further, the cracks extend to about the same peak tensile stress value for both the water and air buffers (compare Figures 37 and 38).

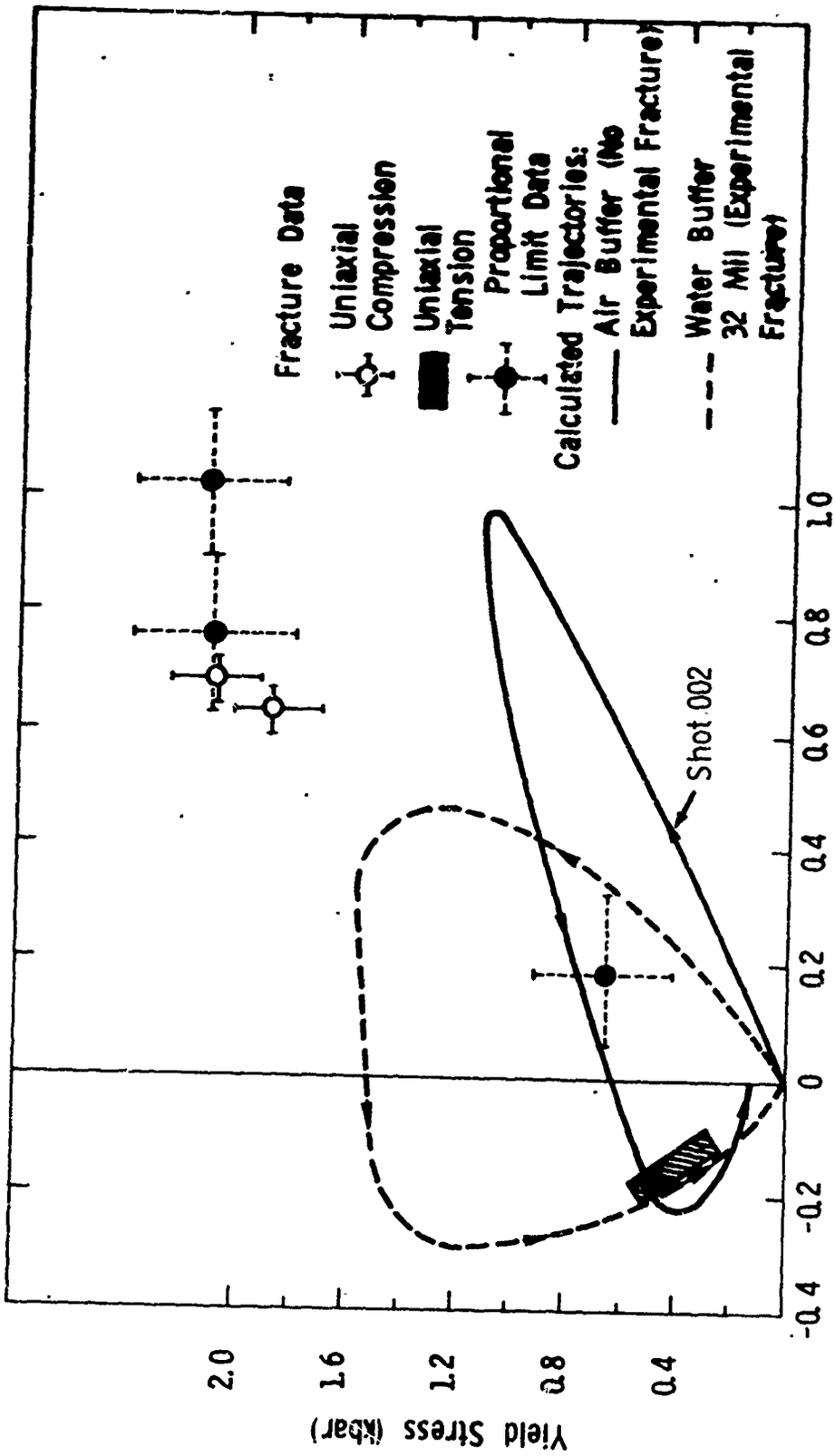

Figure 36 Calculated stress trajectories and experimental triax data.

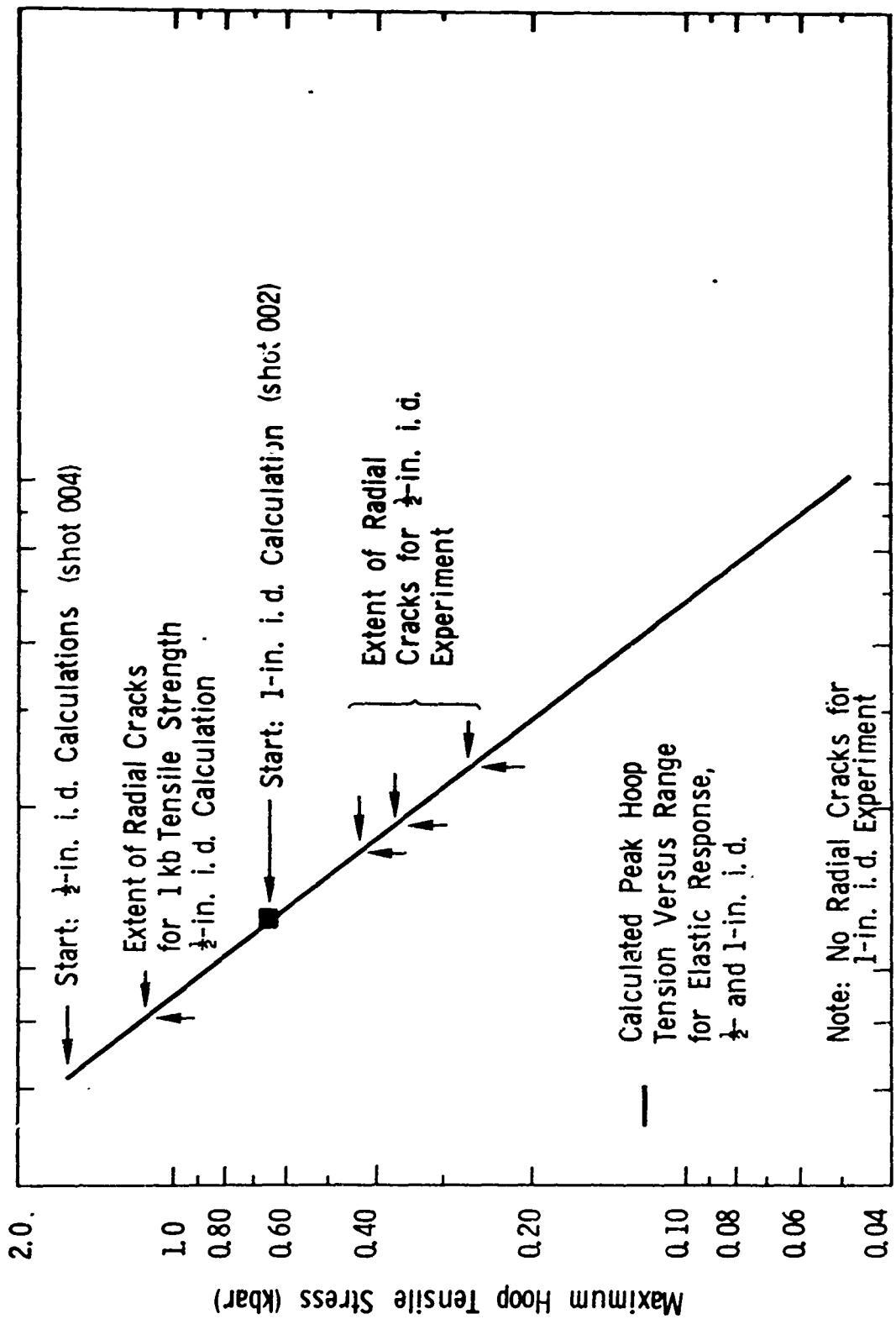

Figure 37 Air buffer, 1/2 and 1 inch inside diameter.

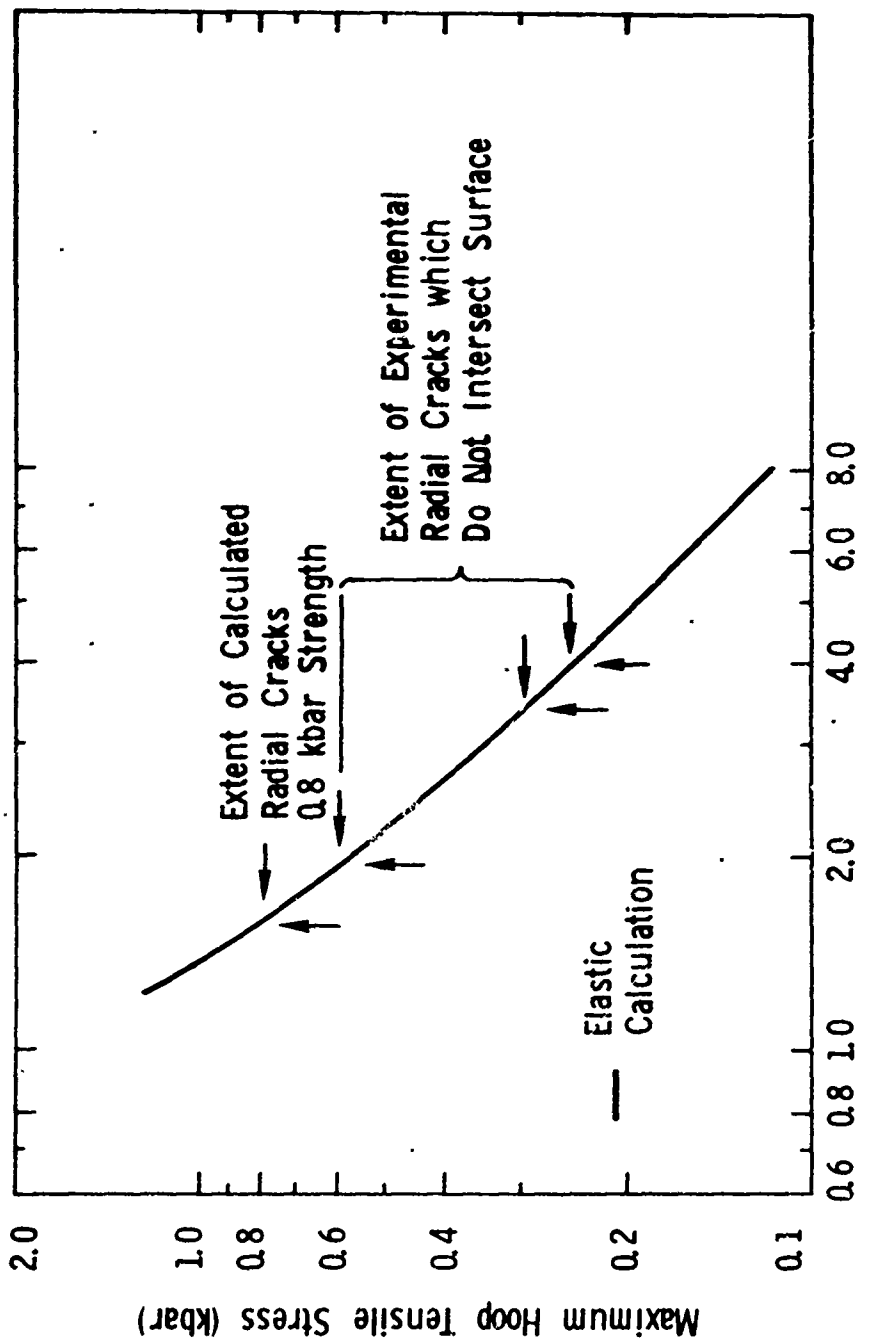

Figure 38 Water buffer, 32 mil wire.

SECTION 6
CONCLUSIONS AND RECOMMENDATIONS

Two parallel paths were followed in this investigation of fracture and comminution of rock. The first path was the study of existing analytical models of fracture and comminution and the application of these models to the dynamic stress fields appropriate for blasting. From this study a method was developed to test the theories in various idealized geometries and loading conditions. The second path was a more fundamental investigation of the process of tensile fracture in rock. Experimental data and finite-difference calculations were used to obtain the dynamic tensile strength of Westerly granite. In addition, it was discovered that cracks can propagate in a tensile stress field more easily (with less stress) than they are initiated.

Some specific recommendations can be made for extending the results presented here. The model for rock failure in hoop tension is inadequate. Provision must be made so that a crack can extend more easily than it can be started, perhaps through an ad hoc stress concentration factor. The experiments using the water buffer should be refined, and additional air buffer shots at intermediate cavity radii should be done to try to pin down the tensile strength a little more accurately. The fracture and comminution program should allow for variable material properties, and additional models should be tested.

More generally, as these future results begin to show a clearer picture of dynamic fracture, the two approaches can blend--results on dynamic fracture can be used to refine, say, the Galin spall model, and particle size distributions from the fracture and comminution program can be used in more detailed calculations of the interaction of stress waves and the effects of fractured material during blasting.

REFERENCES

1. "Rapid Excavation: Significance--Needs--Opportunities," National Academy of Sciences, Washington, D. C., 1968.

2. F. G. Robertson, "Compilation of Data on Craters Produced by Explosives," Astrogeologic Studies, Annual Progress Report, U. S. Geological Survey, NASA-CR-87057, November 1966.

3. Mark L. Wilkins, "Calculation of Elastic-Plastic Flow" in Methods in Computational Physics, Vol. 3, Academic Press, New York (1964).

4. An Introduction to the PISCES™ System of Continuum Mechanics Code, Physics International Company, October 1971.

5. Blasters' Handbook, E. I. du Pont de Nemours and Co., Wilmington, Delaware (15th ed.).

6. A. M. Gaudin, "Comminution as a Chemical Reaction," Mining Engineering, 7, 1955, pp. 561-562.

7. First Symposium on Rock Mechanics, Colorado School of Mines, July 1956.

8. L. A. Galin and G. P. Cherepanov, "Self-Sustaining Failure of a Stressed Brittle Body," Soviet Physics-Doklady, 11, September 1966.

9. E. Rabinowicz, Friction and Wear of Materials, Wiley, 1965.

10. R. T. Hukki and I. G. Reddy, "The Relation Between Energy Input and Fineness in Comminution," Second European Symposium on Size Reduction, Verlag Chemie (1967).

11. C. Orr, Particulate Technology, MacMillan and Company, New York (1966).

REFERENCES (cont.)

12. L. Knopoff and G. MacDonald, "Attenuation of Small Amplitude Stress Waves in Solids," Rev. Mod. Phys., 30, 1178-1192 (1958).

13. W. Goldsmith and C. F. Austin, "Some Dynamic Characteristics of Rocks," in Stress Waves in Anelastic Solids, ed. H. Kolsky, Springer (1964).

14. D. D. Rabb, "Particle-Size Distribution Study, Piledriver Event," in Symposium on Engineering With Nuclear Explosives, 1970, USAEC, CONF-700101, 1970.

15. S. R. Swanson, Development of Constitutive Equations for Rocks, Ph.D Thesis, University of Utah, December 1969.

16. W. S. Brown and S. R. Swanson, Constitutive Equations for Westerly Granite and Cedar City Tonalite for a Variety of Loading Conditions, DASA-2473, University of Utah, March 1970.

17. H. K. Kutter, The Interaction Between Stress Wave and Gas Pressure in the Fracture Process of an Underground Explosion in Rock, With Particular Application to Presplitting, Ph.D Thesis, University of Minnesota, June 1967.

18. H. K. Kutter and C. Fairhurst, "On the Fracture Process in Blasting," Int. J. Rock Mech. Min. Sci., 8, 181-202 (1971).

19. J. B. Walsh, "The Effect of Cracks on Poisson's Ratio," J. Geophys. Res., 70, 5249, October 15, 1965.

20. W. Herrmann, "Constitutive Equation for the Dynamic Compaction of Ductile Porous Materials," Journ. Appl. Physics, 40, 6, 2490ff, May 1969.

21. I. M. Fyfe, R. R. Ensminger, and R. Swift, The Effects of Shear on Stress Wave Propagation, AFWL TR-65-12, Air Force Weapons Laboratory, August 1965.

22. R. R. Ensminger and I. M. Fyfe, "Constitutive Model Evaluation Using Cylindrical Stress Wave Propagation," J. Mech. Phys. Solids, 14, 231-238 (1966).

REFERENCES (cont.)

23. R. P. Swift and I. M. Fyfe, "Elastic/Viscoplastic Theory Examined Using Radial Cylindrical Stress Waves," J. Appl. Mech., 37, 1134-1140, December 1970.

24. G. W. Bigg, "The Elastic and Plastic Response of a Thin Cylindrical Shell to an Internal Impulsive Load," Ph.D Thesis, University of Illinois.

25. W. G. Chase and H. K. Moore, Exploding Wires, Vols. 1, 2, 3, and 4, Plenum Press, New York (1960-1968).

26. Fracture and Comminution of Rock, PITR-310, Physics International Company, San Leandro, California, August 1971.

27. D. D. Keough, R. F. Williams, and D. Bernstein, "Piezoresistive Pressure Transducer," Proceedings ASME, December 1964.

28. D. Bernstein et al., "Research on Manganin Pressure Transducers," in Behavior of Dense Media Under Dynamic Pressure, Symposium N.D.P., Paris, 1967, pp. 461-468, Gordon & Breach, New York, 1968.

29. D. D. Keough and J. Y. Wong, "Variation of Shock Piezoresistance Coefficient of Manganin as a Function of Deformation," J. Appl. Phys., 41, 3508-3515, July 1970.

APPENDIX A

THE FRACTURE AND COMMINUTION COMPUTER PROGRAM

The fracture and comminution program consists of one main program together with function PRESS and subroutine CLASIF. PRESS calculates the pressure at each time step in each space zone. CLASIF performs the particle-sieving and size analysis described in Block D (Figure 3).

The program listing and input instructions follow. Figure 7 is a printout of typical input data to the program. All data are in centimeter-gram-microsecond units. These inputs are discussed below.

Geometry. G = 0, 1, 2 selects plane, cylindrical, or spherical geometry. RO and RMAX are inner and outer boundaries of the rock. PPRIN is a control or printing of certain optional outputs as described at lines 214 and 243 of the main program. If FREESU is non-zero, the outer boundary is assumed to be a free surface and the Galin spall model is tested.

Forcing Function. The correspondence between the variables listed in the table and those given in Block B (Section 3.3.2) is as follows:

PMAX is p_o

ALPH is $a\alpha$

BETA is $b\alpha$

XO is x_o

A is A

B is B

Not all the nine slots on each data card are now used. The remaining slots are available to read in additional data if the program is revised.

Input data format is listed in Table A1.

Program Listing. A listing of the FORTRAN program follows.

TABLE A1

FRACTURE AND COMMINUTION PROGRAM--INPUT DATA

Card Type No.	Entry No. on Card	Name in Program	Symbol in Writeup	
1	1	G	2n	Geometry factor, G=0,1,2 for plane, cylindrical, spherical
	2	RO	r_o	Inner radius, must be non-zero if G is 1 or 2
	3	RMAX	r_{max}	Outer radius
	4	NZON		Number of space (mass) zones
	5	PPRIN		Controls printout of certain quantities. See text.
	6	FREESU		If FREESU > 0., RMAX is free surface and Green spall model is computed
	7			
	8			
	9			
2	1	PMAX	p_o	Initial, maximum pressure at r_o in forcing function
	2	ALPH	$a\alpha$	Coefficient of exponent in forcing function
	3	XO	x_o	Proportional to wavelength of forcing function
	4	DTI		Time step
	5	A	A	Coefficient of exponential in forcing function
	6	B	B	Coefficient of exponential in forcing function

TABLE A1 (cont.)

Card Type No.	Entry No. on Card	Name in Program	Symbol in Writeup	
	7	BETA	b_α	Coefficient of exponential in forcing function
	8			
	9			
3	1	RHO	ρ	Density of the rock
	2	YMOD	E	Young's modulus
	3	PRAT	ν	Poisson's ratio
	4	Q	Q	Solid-friction coefficient
	5	SCOMP	S_c	Compressive strength coefficient
	6	STENS	S_t	Tensile strength coefficient
	7			
	8			
	9			
4	1	CEFR	k	Rittinger comminution efficiency
	2	SSE	T	Specific surface energy
	3	SHAPV	f_v	Volume shape factor
	4	BWI	W_i	Bond work index
	5	SHAPA	f_a	Area shape factor
	6	DIAMIN	$v_1^{1/3}$	Minimum size-class diameter
	7	SIZRAT	R	Ratio of volumes of successive size classes
	8	JMAX		Number of size classes
	9			

FORTRAN PROGRAM

```
      PROGRAM  HEUB(INPUT,OUTPUT,TAPE5=INPUT,TAPE6=OUTPUT)
C
C
      COMMON PMAX,ALPH,BETA,A,G,Q,X0,R0,DR,DT,CP,B
      COMMON IG, R, NZON, DIAMIN, SIZRAT, SHAPA, SHAPV, JMAX
      DIMENSION P(41,100),E(41,100),R(41),K(41),RMDP(41),BMDP(41),
     1          PBP(41),TBP(41),RMDM(41),BMDM(41),PBM(41),TBM(41),
     2          T(10),TITLE(10),CARD(9),WARRY(41,100),
     3          WACUMP(41,100),WACUMM(41,100),DIAM(41)
     1 ,TAR(41),GAL(41),PAR(41)
C
      INTEGER PNTR,CRDR
      DATA CRDR/5/,PNTR/6/,PPRIN/0./,ERR/0./
C
COMMENCE OPERATION
      READ(CRDR,1000) (TITLE(I),I=1,10)
      WRITE(PNTR,1002) (TITLE(I),I=1,10)
  101 READ(CRDR,1001) NTYP,(CARD(I),I=1,9)
      IF(EOF(CRDR)) 103,102
  102 GO TO (110,120,130,140),NTYP
  102 GO TO (110,120,130,140),NTYP
C
CARD TYPE 1 - GEOMETRY
  110 G = CARD(1)
      IG = IFIX(G + 1.1)
      IG = IFIX(G + 1.1)
      R0 = CARD(2)
      RMAX = CARD(3)
      NZON = CARD(4)
      PPRIN = CARD(5)
      FREESU = CARD(6)
C  ENTRY 6 ON CARD TYPE 1. POSITIVE IF RMAX IS FREE SURFACE
      IF(RMAX.LE.R0.OR.NZON.LE.0 ) GO TO 210
      IF(R0.EQ.0..AND.G.NE.0.) GO TO 210
      GO TO 101
C
CARD TYPE 2 - FORCING FUNCTION
  120 PMAX = CARD(1)
      ALPH = CARD(2)
      X0 = CARD(3)
      DTI = CARD(4)
      A = CARD(5)
```

```
      B = CARD(6)
      BETA = CARD(7)
      IF(X0.LE.0..OR.DTI.LE.0.) GO TO 220
      GO TO 101
C
CARD TYPE 3 - MATERIAL PROPERTIES
  130 RHO = CARD(1)
      YMOD = CARD(2)
      PRAT = CARD(3)
      Q = CARD(4)
      SCOMP = CARD(5)
      STENS = CARD(6)
      IF(RHO.LE.0..OR.Q.LE.0..OR.PRAT.LE.-1..OR.PRAT.GE..5)GO TO 230
      GO TO 101
C
CARD TYPE 4 - COMINUTION PARAMETERS
  140 CEFR = CARD(1)
      SSE  = CARD(2)
      SHAPV = CARD(3)
      BWI = CARD(4)
      SHAPA = CARD(5)
      DIAMIN = CARD(6)
      SIZRAT = CARD(7)
      JMAX = IFIX(CARD(8) + .1)
      IF(CEFR.LE.0..OR.SHAPV.LE.0.) GO TO 240
      GO TO 101
C
  103 WRITE(PNTR,1003) G,RMAX,R0,NZON,PPRIN,FREESU
      WRITE(PNTR,1004) PMAX,ALPH,X0,DTI,BETA,A,B
      WRITE(PNTR,1005) RHO,YMOD,PRAT,Q,SCOMP,STENS
      WRITE(PNTR,1006) SSE,CEFR,SHAPV,BWI,SHAPA,DIAMIN,SIZRAT,JMAX
      IF(ERR.NE.0.) GO TO 20
C
COMPUTE BULKMODULUS, SOUND SPEED AND PROPER TIME STEP
C
      BMOD = YMOD/(3.*(1.-2.*PRAT))
      CSQ = 3.*BMOD*(1.-PRAT)/(1.+PRAT)
      CP = SQRT(CSQ/RHO)
      NCYC = ((RMAX-R0)/CP + 3./ALPH)/DTI + 1
      DT = DTI
      IF(NCYC.LE.100) GO TO 104
      NCYC = 100
      DT = ((RMAX - R0)/CP + 3./ALPH)/NCYC
  104 WRITE(PNTR,1007) BMOD,CP,DT
      NPOST = NZON + 1
      DR =(RMAX-R0)/NZON
      G = G/2.
C
```

```
CALCULATE PRESSURE(R,T) AND ENERGY(R,T)  GRIDS
C
      DO 1 J = 1,NPOST
         DELTR = (J-1)*DR
         R(J) = R0 + DELTR
         DO 2 I = 1,NCYC
            TIME = (I-1)*DT
            P(J,I) = PRESS(DELTR,TIME)
            E(J,I) = 0.5*P(J,I)*ABS(P(J,I))/BMOD
    2   CONTINUE
    1 CONTINUE
C
COMINUTION INITIALIZATION
C
      DO 4 J = 1,NPOST
      WACUMP(J,1)=0.
      WACUMM(J,1)=0.
         RMDP(J) = 1.E+10
         RMDM(J) = RMDP(J)
         BMDP(J) = RMDP(J)
    4 BMDM(J) = RMDP(J)
C
COMINUTION CALCULATIONS
C
      DO 8 J = 2,NPOST
         PP = 0.
         PM = 0.
         TP = 0.
         TM = 0.
         DO 7 I = 1,NCYC
            TIME = (I-1)*DT - DR/CP
            RAD = (J-2)*DR
            PG = PRESS(RAD,TIME)
            EEL = 0.5*PG*ABS(PG)/BMOD
            WCOM = EEL*(1. - DR/R(J))**(2.*G) - E(J,I)
      WARRY(J,I) = WCOM
            IF(P(J,I).GT.STENS.AND.P(J,I).LE.SCOMP) GO TO 7
            IF(WCOM.EQ.0.) GO TO 7
            IF(P(J,I).LE.STENS) GO TO 6
C
C                  COMPRESSIVE COMINUTION
C
            IF(WCOM.LT.0.) GO TO 7
      IF(I.EQ.1) GO TO 51
      WACUMP(J,I) = WACUMP(J,I-1) + WCOM
   51 CONTINUE
```

```
                PP = PP + 0.5*(P(J,I-1) + P(J,I))*DT
                TP = TP + DT
                RIT = 6.*SSE/(WCOM*CEFR*SHAPV)
C CUMULATE COMMINUTION STEPS
        RIT = 1./(1./RIT + 1./RMDP(J))
                RMDP(J) =AMIN1(RIT,RMDP(J))
                BND = .01*(BWI/WCOM)**2
        DEL = 1./SQRT(BND) + 1./SQRT(BMDP(J))
        BND = 1./(DEL)**2
                BMDP(J) =AMIN1(BND,BMDP(J))
                GO TO 7
C
C                       TENSILE COMINUTION
C
     6          IF(WCOM.GT.0.) GO TO 7
        IF(I.EQ.1) GO TO 61
        WACUMM(J,I) = WACUMM(J,I-1) + WCOM
    61 CONTINUE
                PM = PM + 0.5*(P(J,I-1) + P(J,I))*DT
                TM = TM + DT
                RIT = -6.*SSE/(WCOM*CEFR*SHAPV)
C CUMULATE COMMINUTION STEPS
        RIT = 1./(1./RIT + 1./RMDM(J))
                RMDM(J) =AMIN1(RIT,RMDM(J))
                BND = .01*(BWI/WCOM)**2
        DEL = 1./SQRT(BND) + 1./SQRT(BMDM(J))
        BND = 1./(DEL)**2
                BMDM(J) =AMIN1(BND,BMDM(J))
     7      CONTINUE
             IF(TP.LE.0.) GO TO 5
             PBP(J) = PP/TP -SCOMP
             TBP(J) = TP
     5       IF(TM.LE.0.) GO TO 8
             PBM(J) = PM/TM - STENS
             TBM(J) = TM
     8 CONTINUE
C   ENTER GALIN SPALL MODEL
        IF(FREESU.LE.0.) GO TO 11
C   INITIALIZE SPALL PARTICLE SIZE
        DO 82 J=1, NPOST
     82 GAL(J)=1.E+10
        TRAT = (RMAX - R0)/CP
        DO 81 L=1,NZON
        J = NPOST + 1 - L
        RAD = R(J)
        TIME = TRAT + (RMAX - RAD)/CP
C   ARRIVAL TIME OF WAVE FROM FREE SURFACE
        RADO = RAD - R0
```

```
      PG = PRESS(RADO,TIME)
C     INCIDENT PRESSURE WHEN REFLECTED WAVE ARRIVES
      TAR(J) = TIME
      PAR(J) = PG
      IF(PG .LE.0) GO TO 81
C  IF ZONE IS IN TENSION IT CANNOT SPALL
      IF(RMDP(J) .LT. 1.E+10) GO TO 81
C  IF ZONE HAS CRUSHED IT CANNOT SPALL
      EEL = 0.5*PG*PG/BMOD
      EELM =EEL / RHO
      X  = PG/(RHO*CP)
      XX = X*X
      SURENG = EELM-0.5*(XX-2.*PG/RHO)
      GAL(J) = 6.* SSE /(RHO * SURENG)
   81 CONTINUE
   11 CONTINUE
C
C  READY TO DETERMINE SIZE DISTRIBUTION
C  OUTPUT SECTION
C
      WRITE(PNTR,1008) (TITLE(I),I=1,10)
      DO 12 J = 1,NPOST
   12 WRITE(PNTR,1009) R(J),RMDP(J),BMDP(J),RMDM(J),BMDM(J),PBP(J),
     1                 TBP(J),PBM(J),TBM(J)
C     SKIP GALIN SPALL PRINTOUT IF NO FREE SURFACE
      IF(FREESU.LE.0) GO TO 18
      WRITE(PNTR,1026) (TITLE(I),I=1,10)
      DO 48 J=1,NPOST
   48 WRITE(PNTR,1025) J,R(J),GAL(J),TAR(J),PAR(J)
   18 CONTINUE
C
C IF PPRIN  GT ZERO AND LT 3. PRINT P(R,T) GRID
      IF(PPRIN.EQ.0.) GO TO 20
      IF (PPRIN. GE. 3.) GO TO 30
      IND = NCYC/10
      DO 13 M=1,IND
         MI = 10*(M-1)
         MZ = MI + 1
         ML = 10*M
         WRITE(PNTR,1010) (TITLE(I),I=1,10)
         DO 14 N=1,10
   14    T(N) = (MI + N - 1)*DT
         WRITE(PNTR,1011) (T(N),N=1,10)
      WRITE(PNTR,1013)
         DO 15 J = 1,NPOST
   15    WRITE(PNTR,1012) R(J),(P(J,N),N=MZ,ML)
   13 CONTINUE
      IF(NCYC.LE.10*IND) GO TO 30
```

```
      WRITE(PNTR,1010) (TITLE(I),I=1,10)
      MI = 10*IND
      ML = NCYC - MI
      DO 16 N = 1,ML
   16 T(N) = (MI + N - 1)*DT
      WRITE(PNTR,1011) (T(N),N=1,ML)
      WRITE(PNTR,1013)
      MI = MI + 1
      DO 17 J=1,NPOST
   17 WRITE(PNTR,1012) R(J),(P(J,N),N=MI,NCYC)
      GO TO 30
   30 CONTINUE
C IF PPRIN LT 2. PRINT ENERGY ABSORBED IN EACH TIME STEP
      IF (PPRIN.GE.2.) GO TO 40
      IND = NCYC/10
      DO 23 M=1,IND
         MI = 10*(M-1)
         MZ = MI + 1
         ML = 10*M
         WRITE(PNTR,1018) (TITLE(I),I=1,10)
         DO 24 N=1,10
   24    T(N) = (MI + N - 1)*DT
         WRITE(PNTR,1011) (T(N),N=1,10)
      WRITE(PNTR,1013)
         DO 25 J = 1,NPOST
   25    WRITE(PNTR,1012) R(J),(WARRY(J,N),N=MZ,ML)
   23 CONTINUE
      IF(NCYC.LE.10*IND) GO TO 20
      WRITE(PNTR,1018) (TITLE(I),I=1,10)
      MI = 10*IND
      ML = NCYC - MI
      DO 26 N = 1,ML
   26 T(N) = (MI + N - 1)*DT
      WRITE(PNTR,1011) (T(N),N=1,ML)
      WRITE(PNTR,1013)
      MI = MI + 1
      DO 27 J=1,NPOST
   27 WRITE(PNTR,1012) R(J),(WARRY(J,N),N=MI,NCYC)
   40 CONTINUE
      IND = NCYC/10
      DO 33 M=1,IND
         MI = 10*(M-1)
         MZ = MI + 1
         ML = 10*M
         WRITE(PNTR,1019) (TITLE(I),I=1,10)
         DO 34 N=1,10
   34    T(N) = (MI + N - 1)*DT
         WRITE(PNTR,1011) (T(N),N=1,10)
```

```
      WRITE(PNTR,1013)
         DO 35 J = 1,NPOST
   35    WRITE(PNTR,1012) R(J),(WACUMP(J,N),N=MZ,ML)
   33 CONTINUE
      IF(NCYC.LE.10*IND) GO TO 30
      WRITE(PNTR,1019) (TITLE(I),I=1,10)
      MI = 10*IND
      ML = NCYC - MI
      DO 36 N = 1,ML
   36 T(N) = (MI + N -1)*DT
      WRITE(PNTR,1011) (T(N),N=1,ML)
      WRITE(PNTR,1013)
      MI = MI + 1
      DO 37 J=1,NPOST
   37 WRITE(PNTR,1012) R(J),(WACUMP(J,N),N=MI,NCYC)
      IND = NCYC/10
      DO 43 M=1,IND
         MI = 10*(M-1)
         MZ = MI + 1
         ML = 10*M
         WRITE(PNTR,1020) (TITLE(I),I=1,10)
         DO 44  N=1,10
   44    T(N) = (MI + N - 1)*DT
         WRITE(PNTR,1011) (T(N),N=1,10)
      WRITE(PNTR,1013)
         DO 45 J = 1,NPOST
   45    WRITE(PNTR,1012) R(J),(WACUMM(J,N),N=MZ,ML)
   43 CONTINUE
      IF(NCYC.LE.10*IND) GO TO 20
      WRITE(PNTR,1020) (TITLE(I),I=1,10)
      MI = 10*IND
      ML = NCYC - MI
      DO 46 N = 1,ML
   46 T(N) = (MI + N - 1)*DT
      WRITE(PNTR,1011) (T(N),N=1,ML)
      WRITE(PNTR,1013)
      MI = MI + 1
      DO 47 J=1,NPOST
   47 WRITE(PNTR,1012) R(J),(WACUMM(J,N),N=MI,NCYC)
      GO TO 20
C
CERROR SECTION
C
  210 WRITE(PNTR,1014)
      ERR = 1.
      GO TO 101
  220 WRITE(PNTR,1015)
      ERR = 1.
```

```
      GO TO 101
  230 WRITE(PNTR,1016)
      EPR = 0.
      GO TO 101
  240 WRITE(PNTR,1017)
      EPR = 1.
      GO TO 101
   20 CONTINUE
C  RITTINGER COMPRESSIVE MODE
      WRITE(PNTR, 1021)
      WRITE(PNTR, 1022)
      CALL CLASIF(RMDP)
C  RITTINGER TENSILE MODE
      WRITE(PNTR, 1021)
      WRITE(PNTR, 1023)
      CALL CLASIF(RMDM)
C  RITTINGER MIXED MODE
      DO 21 I=1, MPOST
   21 DIAM(I) = AMIN1 (RMDP(I),RMDM(I))
      WRITE(PNTR, 1021)
      WRITE(PNTR, 1024)
      CALL CLASIF(DIAM)
      CALL EXIT
C
C
 1000 FORMAT(10A8)
 1001 FORMAT(I8,9E8.0)
 1002 FORMAT(1H1,11H INPUT DATA,10X,10A8 //)
 1003 FORMAT(5X, 9H GEOMETRY/15X,3H G=,F3.0/12X,6H RMAX=,F5.0,3H CM/
     1       14X,4H R0=,F5.0,3H CM/20X,I3,6H ZONES/
     210X,7H PPRIN=,F5.1/10X,8H FREESU=,F5.1//)
C
 1004 FORMAT(5X,17H FORCING FUNCTION/20X,7H PMAX =,E10.3,5H MBAR/
     1       20X,7H ALPH =,E10.3,12H PER MIC.SEC/23X,4HX0 =,F5.2,3H CM/
     2       10X,18H INPUT TIME STEP =,F10.2, 7H MICSEC/20X,7H BETA =,
     3       E10.3,12H PER MIC SEC/23X,4H A = E10.3/23X,4H B = E10.3//)
C
 1005 FORMAT(5X,20H MATERIAL PROPERTIES/15X,10H DENSITY =,F6.3, 6H GM/CC
     1       /15X,17H YOUNGS MODULUS =,E10.3, 5H MBAR/16X,16HPOISSONS RA
     2TIO =,F7.3/15X,19H DAMPING CONSTANT =,F10.3/15X,20H ULTIMATE STREN
     3GTH =,E10.3, 5H MBAR/15X,19H TENSILE STRENGTH =,E10.3, 5H MPAR//)
C
 1006 FORMAT(5X,22H COMINUTION PARAMETERS/15X,26H SPECIFIC SURFACE ENERG
     1Y =,E10.3/15X,23H RITTINGER EFFICIENCY = F6.3/15X,22H VOLUME SHAPE
     2 FACTOR = F6.4/15X,18H BOND WORK INDEX = E10.3/
     315X,7H SHAPA=,F6.4,/15X,8H DIAMIN=,E10.3,/15X,8H SIZRAT=,E10.3/
     315X,6H JMAX=,I2,                                    /38H NOTES FOR THE
     2 FOLLOWING COMPUTED DATA/5X,18H R = POSITION (CM)/5X,36H RHO = RIT
```

```
     4TIN=FR MEAN DIMENSION (CM)/5X,31H BMD = BOND MEAN DIMENSION (CM)/
     55X,32H SUFFIX P IMPLIES COMPRESSION   /5X,32H SUFFIX M IMPLIES TEN
     6SION        /5X,28H PB = MEAN OVERSTRESS (MBAR)/5X,31H TB = DURATIO
     7N OF OVERSTRESSING/41H ALL VARIABLES ARE SCALAR POINT FUNCTIONS//)
C
 1007 FORMAT(15H BULK MODULUS =,E10.3, 5H MBAR/14H SOUND SPEED = F10.3,
     1       10H CM/MICSEC/21H COMPUTED TIME STEP = E10.4, 7H MICSEC)
C
 1008 FORMAT(1H1/16H COMINUTION DATA,10A8//7X,1HR,13X,4HRMOP,10X,4HBMOP,
     1        9X,5H RMOM, 9X,5H BMOM,10X,3HPBP,11X,3HTBP,11X,3HPBM,11X,
     2          3HTBM)
C
 1009 FORMAT(9F14.4)
 1010 FORMAT(1H1/33H PRESSURE(POSITION,TIME)    (MBAR),10A8//50X,14H TIME
     1 (MICSEC))
C
 1011 FORMAT(10X,10E11.3)
 1012 FORMAT(F7.3,3X,10E11.3)
 1013 FORMAT(5H     R)
 1014 FORMAT(18H ERROR IN GEOMETRY)
 1015 FORMAT(26H ERROR IN FORCING FUNCTION)
 1016 FORMAT(29H ERROR IN MATERIAL PROPERTIES)
 1017 FORMAT(31H ERROR IN COMINUTION PARAMETERS)
 1018 FORMAT(1H1/31H ABSORBED ENERGY DENSITY (MBAR),10A8//50X,16H TIME
     1 (MICSEC))
 1019 FORMAT(1H1/* CUMUL ENERGY DENS ABSORBED IN COMPRESS *,10A8
     1//50X,*TIME (MICSEC) * )
 1020 FORMAT(1H1/* CUMUL ENERGY DENS ABSORBED IN TENSION *,10A8
     1//50X,* TIME (MICSEC)*)
 1021 FORMAT(*1*)
 1022 FORMAT(* RITTINGER COMPRESSIVE MODE SIZE CLASSIFICATION*/)
 1023 FORMAT(*  RITTINGER TENSILE      MODE SIZE CLASSIFICATION */)
 1024 FORMAT(*  RITTINGER MIXED       MODE SIZE CLASSIFICATION */)
 1025 FORMAT(1H ,I2,3X,4E11.3)
 1026 FORMAT(1H1/17H GALIN SPALL DATA,10A8//2X,1HJ,7X,4HR(J),5X,6HGAL(J)
     1,5X,6HTAR(J),5X,6HPAR(J))
      END
```

```
      FUNCTION PRESS(R,T)
C
      COMMON PMAX,ALPH,BETA,A,G,Q,X0,R0,DR,DT,CP,B
C
      DELT = T - R/CP
      PRESS = 0.
      IF(DELT.LT.0.) RETURN
      TOR = 1.
      IF(G.NE.0.) TOR = (R0/(R0+R))**G
      FAC = PMAX*EXP(-R/(X0*Q))
      PRESS = FAC*TOR*(A*EXP(-ALPH*DELT) - B*EXP(-BETA*DELT))
      RETURN
      END



      SUBROUTINE CLASIF(DIAM)
      COMMON PMAX,ALPH,BETA,A,G,Q,X0,R0,DR,DT,CP,B
      COMMON IG, R, NZON, DIAMIN, SIZRAT, SHAPA, SHAPV, JMAX
      DIMENSION ZVOL(41), ZSURF(41), DIAM(1), R(41), SIZ(50),
     1FCVOL(50), FCSUR(50)
      INTEGER PNTR,CROR
      PNTR = 6
      NPOST = NZON+1
C  INITIALIZE RELATIVE FRACTURED VOLUME AND PARTICLE SURFACE AREA
      VOLF = 0.
      FSUR = 0.
      WRITE(PNTR,2003)
      DO 10 I=2, NPOST
C  CALCULATE RELATIVE VOLUME OF EACH ZONE
      ZVOLI = R(I)**IG-R(I-1)**IG
      ZVOL(I) = ZVOLI
C  HAS ZONE FRACTURED
      IF(DIAM(I) .GE. 1.E10) GO TO 10
C  IF SO ADD ITS VOLUME AND PARTICLE SURFACE TO FRACTURED TOTALS
      VOLF=VOLF+ZVOLI
      ZSURF(I)=(ZVOLI*SHAPA)/(SHAPV*DIAM(I))
      FSUR=FSUR+ZSURF(I)
       WRITE(PNTR,2001) I, R(I), ZVOL(I), VOLF, ZSURF(I), FSUR
   10 CONTINUE
```

```
C  DEFINE SIZE CLASSES
      DIARAT =(SIZRAT)**.3333
      DO 20 J=1,JMAX
   20 SIZ(J)=DIAMIN* (DIARAT)**(J-1)
C  INITIALIZE CUMULATIVE VOLUME AND SURFACE
      CVOL = 0.
      CSUR = 0.
      WRITE (PNTR,2002)
      WRITE(PNTR,2004)
      DO 40 J=1,JMAX
C  INITIALIZE VOLUME AND SURFACE IN CLASS J
      VOLJ = 0.
      SURJ = 0.
      SIZE = SIZ(J)
C  FIND ZONES THAT      PASS SIEVE J
      DO 30 I=2, NPOST
      IF (DIAM(I) .GT. SIZE) GO TO 30
C  ADD VOLUME AND SURFACE TO CLASS J
      VOLJ = VOLJ + ZVOL(I)
      SURJ = SURJ + ZSURF(I)
   30 CONTINUE
C  CUMULATE VOLUME AND SURFACE
      CVOL =        VOLJ
      CSUR =      SURJ
C     NORMALIZE CUMVOL AND SURFACE
      FCVOL(J) = CVOL/VOLF
      FCSUR(J) = CSUR/FSUR
      WRITE(PNTR, 2001)  J,SIZE,CVOL,CSUR,FCVOL(J),FCSUR(J)
   40 CONTINUE
 2001 FORMAT(3X, I2, 5(3X,1P1E10.3))
 2002 FORMAT(*1*)
 2003 FORMAT( * ZONE RADIUS   RVOLUME   CUM VO.   RSURFACE  CUMSURF*,/)
 2004 FORMAT( * CLASS SIZE    CUMRVOL   CUMRSURF  FCUMVOL   FCUMSURF*,/)
      RETURN
      END
```